Kinematic models of interseismic deformation from inversion of GPS and InSAR measurements to estimate fault parameters and coupling degree

PRESENTATA DA:
LETIZIA ANDERLINI

REFERENTE:
PROF.SSA MARIA ELINA BELARDINELLI

COORDINATORE DOTTORATO:
PROF. MICHELE DRAGONI

Acknowledgments

Contents

Introduction

Deep movements on mantle bring the Earth's crust to fracture into rigid plates bounded by fault systems, where is realized the relative motion of plates by means of earthquakes or aseismic displacements. During the interseismic phase of seismic cycle (i.e. any time period far from coseismic events and the following astenospheric relaxation periods) plate movements and their relative interactions generate on the Earth's surface a displacement velocity field that in proximity of fault systems presents variations that is influenced by fault geometry, crust rheology and intensity of plates relative motion (Bürgmann & Dresen, 2008; Thatcher, 2009). This deformation is measurable by geodetic techniques, that, thanks to recent improvements of satellite technology, provide huge amounts of measures with millimeter precision, allowing to study the interseismic deformation also at local fault scale of few kilometers.

The growing number of continuously recording GPS stations in Italy, particularly during last 5 years, gives the possibility to detect, with higher accuracies and precisions than in the past, variations of ground deformation rates across major fault structures. Moreover also the InSAR geodetic technique, after many years of imaging satellite acquisition, is beginning to provide accurate and dense datasets of deformation rates for the Italian peninsula, detecting in the best cases variations of deformation rates at shorter spatial scale than the GPS measurements can show.

In this dissertation we have considered, as kinematic interseismic modeling, Dislocation (Savage & Burford, 1973) and Block Modeling (Meade & Loveless, 2009) approaches. These two methods allow to model the interseimic velocities considering faults as rectangular surfaces embedded in an homogeneous, elastic and isotropic half-space (Okada, 1985). With the first method it is possible to reproduce interseismic displacement rates at local fault scale, estimating the best fault parameter set, such as position and dimentions, to explain the observed velocities. On the other hand the second method considers instead interseismic velocity fields at wider spatial scales, where the measured deformation rates do not concern only the deformation occurring in the fault proximity, but they also provide information about the relative motion of plates (or blocks). In this approach the fault-systems interested by the deformation rate (located at the plate boundaries) need to be defined a priori, for which, instead, are estimated the long-term fault slip-rates expected from the relative motion of blocks. This is the most important advantage of the Block Modeling (BM) approach, that, assessing the deformation rate accommodated by the considered fault systems, may infer useful information to evaluate the seismic potential of the faults. However the strong disadvantage of this method consists in the apriori

definition of fault geometries that are usually not well-known. Moreover within the BM approach it is possible to evaluate also the spatial variation along the fault planes of the kinematic coupling degree, that describes the seismic or aseismic behavior of the fault portions. In particular a low coupling degree suggests that the fault surface is realizing aseismically the relative motion of blocks, on the contrary fault portions with high coupling degree indicate fault asperities that they may accomplish the relative movement by means of seismic events. Thus the estimation of the coupling degree distribution may provide even more useful information about the seismic potential estimate of the considered fault.

In this dissertation we have applied these approaches in two principal regions characterized by different tectonic frameworks: a purely extensional zone interested by deformation rates of almost 3 mm/yr along NE-SW direction and a right-lateral E-W shear zone of 1 mm/yr of deformation rate along the N-S direction.

The first case concerns a kinematic analysis for the tectonic extension observed across the Umbria-Marche Apennines, where fault geometries are known. In particular this area is characterized by the presence of seismic activity (Amato *et al.*, 1998; Pondrelli *et al.*, 2006) related to not only the high dipping-angle normal-faults (that have generated historical and instrumental moderate earthquakes) but also to the Alto Tiberina (AT) low-angle normal fault (LANF) featured by diffuse microseismicity (**?**), that may indicate a possible aseismic behavior (Collettini, 2002; **?**). However the LANFs are considered by the "Andersonian" theory as averse to faulting, and their possible seismic activity is still a debated topic. Thus we have performed a Block Modeling analysis to evaluate which fault systems are actively accommodating the extensional. Moreover, thanks to the last 3D reconstruction of the ATF surface (Mirabella *et al.*, 2011), we have estimated aslo the interseismic coupling degree distribution, that has been validated by a resolution analysis performed by means of several checkerboard tests.

The second case of study is focused on the Gargano promontory, for which we have considered also InSAR measurements of interseismic velocities. The Gargano promontory is inserted in a complicated seismo-tectonic framework due to a shear zone generated by the relative movement of Adria and Apulia plates (Doglioni *et al.*, 1994). It belongs to a widespread deformation region that concerns mainly the central Adriatic, for which has been observed numerous active fault systems (Brankman & Aydin, 2004; Ridente & Trincardi, 2006) and a diffuse seismicity onshore and offshore the promontory (Console *et al.*, 1993; Pondrelli *et al.*, 2006; Del Gaudio *et al.*, 2007). In this case no specific study has provided evidence of a favored fault boundary between the two plates (D'Agostino *et al.*, 2008), and the only fault most morphologically evident in surface is the Mattinata fault, whose possible seismic activity is well debated. Therefore we have tried to evaluate which deformation is occurring in the Gargano promontory, modeling both GPS and InSAR interseismic velocities considering a combined approach of Dislocation and Block modeling. In this problem we have had to face several steps in order to apply jointly GPS and InSAR data within the BM approach. Firstly we have had to anchored InSAR velocities to the same terrestrial reference frame of GPS data, in order to have comparable measurements. Thanks to the quality and density of the available InSAR velocities, we have decided to

use the Dislocation Modeling (DM), in order to evaluate the best fault parameters able to reproduce the local deformation rate concerning the promontory. Then we have used the fault structure found by the DM approach as fault boundary for a BM approach, in which we have considered both GPS and InSAR velocities. For this considered fault we have finally evaluated also the interseismic coupling degree, that has been validated by means of checkerboard resolution tests.

To perform these analysis we had modified the original BM code (Meade & Loveless, 2009), in order to allow the joint inversion of GPS and InSAR data within the BM approach. Moreover we have modified the specific inversion method in cases where the interseismic coupling distribution had to be estimated, because of the original inappropriate solver method when we should estimate more parameters than the available data (i.e. under-determined problem, Menke, 1989). During each specific analysis we have thus verified the reliability of the modified inversion method, evaluating benefits and drawbacks of the two solvers.

Chapter 1

Kinematic Models to study Interseismic Deformation

1.1 Introduction

The Earth crust deformation takes place as a result of interactions between deep driving forces in the mantle and lithospheric strength. This system has led the crust to fracture into plates moving independently from each other, whose interactions generate lithospheric deformation at boundaries. The traditional view of tectonics is that the lithosphere comprises a strong brittle layer overlying a weak ductile one, which gives rise to two forms of deformation behaviors: brittle fracture, accompanied by earthquakes, in the upper layer, and aseismic ductile flow in the layer beneath (Scholz, 1998). The time passing between an earthquake and the following one can be divided into three phases: coseismic (earthquake generated on a fault), postseismic (viscous relaxation of crust after the earthquake) and interseismic (steady-state-assumed deformation loading). Faults lying in the brittle layer are loaded by a deep steady slip below a locking depth, above which they are assumed to be locked by friction until the coseismic phase occurs.

During the interseismic phase the ground surface undergoes deformation over time that is measurables by geodetic techniques (McKenzie & Jackson, 1983; Segall & Davis, 1997; Bürgmann *et al.*, 2000; Thatcher, 2009; Bürgmann & Thatcher, 2013). Modeling these measurements it is possible to understand where, how and which faults are accommodating that deformation.

In this chapter I will introduce an overview of kinematic interseismic modeling, presenting in details the approaches used in this thesis: "Block Modeling" as the principal method and "Dislocation Model" as an integrated approach for a specific and local study. The theories behind each approach, which codes have been used and the changes made in order to jointly use GPS and InSAR datasets will be exposed.

1.2 Models of the Interseismic Deformation

Many theories have been suggested to model the interseismic deformation: starting from the elastic buried dislocation (Savage & Burford, 1973), passing through the back-slip approach defined by Savage (1983) that have inspired later the kinematic block modeling (McCaffrey, 2002; Meade & Hager, 2005). Block modeling assumes the 7-parameter fault-plane representation described in Okada (1985). Similar methods have been proposed also including one or more viscoelastic layers below the shallow elastic seismogenic part (Savage & Prescott, 1978; Johnson *et al.*, 2007) and stress-driven deep-fault creep (Li & Rice, 1987; Johnson & Segall, 2004) in order to make them more similar to reality. Similar modifications entail adding more unknowns and need a numerical approximations on modeling.

Anyway complicated models may produce solutions not so different from those ones ob-
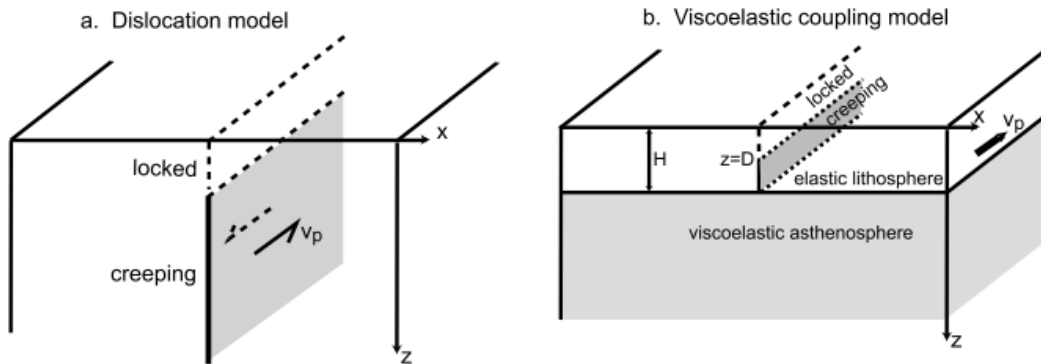
Figure 1.1: *(a) Savage & Burford (1973) model. Interseismic deformation is modeled as slip on a buried dislocation that slides at the plate rate, Vp. (b) Savage & Prescott (1978) coupling model. Cyclic motion down to depth D and steady sliding below D on a fault in an elastic layer over viscoelastic half-space. Slip rate on the fault is equal to the plate velocity, Vp. From Johnson & Segall (2004).*

tained by simpler approaches (Okada, 1985; Savage, 1990). In the case of a linear elastic layer over a viscoelastic half-space (Fig.1.1b), data related to the interseismic period are not affected by the asthenospheric relaxation (concerning the postesismic phase), and can be fit equally well by steady slip downdip of the locked zone in an equivalent homogeneous elastic half-space model (Fig.1.1a, Savage, 1995; Vergne *et al.*, 2001; Kanda & Simons, 2010). It has been shown also that the predictions of interseismic surface velocities for a two layered elastic half-space model (e.g., an elastic layer over an elastic half-space) differ by less than 5% from those for a homogeneous elastic half-space model (Savage, 1998). Therefore using more complicated models than an elastic half space may be justified only if data had very low noise-to-signal ratio and a dense spatial coverage allowing to detect the differences described above. These modelizations have been performed in very few cases (Smith & Sandwell, 2006; Johnson & Fukuda, 2010) for regions where nevertheless numerous simpler models have been already tested.

For these reasons we decide to use easier approaches, namely the Buried Dislocation (BD hereinafter) and the Block Modeling (BM hereinafter) to study the interseismic deformation. Both methods represent a fault as a rectangular plane embedded in an isotropic homogeneous elastic half-space and calculate the surface deformation as proposed in Okada (1985). For the BD modeling only the case of a strike-slip fault will be considered, since it is the case that has concerned a part of this dissertation. On the contrary the BM approach will be explained on detail because it is the principal technique used in this thesis to study the interseismic deformation.

1.3   Dislocation model for strike-slip faults

To model the horizontal deformation across a strike-slip fault, we consider a deep dislocation going to infinity, which is locked from the surface to a depth $\mathbf{z}$, and slips with uniform amount below that depth it. This approach was used for the first time by Savage & Burford (1970) for the San Andreas fault and then was widely used to model the deformation observed on strike-slip faults (e.g. Bürgmann *et al.*, 2000; Rolandone *et al.*, 2008). A schematic representation of a firts kind of dislocation model is shown on Fig.1.1a, where the plate velocity V_p between the two regions is accommodated on the buried part of the fault surface extending below the seismogenic locked part. This model produces on surface a displacement rate pattern that is displayed on Fig.1.2a, where it is worth to note that the unit on y-axis is normalized with respect to the velocity V_p and the x-axis indicates the distance from the fault trace normalized with respect to the locking depth $\mathbf{z}$.

The limit of this approach is that the deformation is caused by a dislocation line (parallel to horizontal) and not by a dislocation surface (Segall, 2010, chap. 2). The implication is that the horizontal deformation on free surface is independent of the dip of fault, if the slip on the fault is spatially uniform and extends to infinite depth. In particular, using a singular screw dislocation, the deformation at free surface is the same whether the fault plane is vertical or horizontal. Thus we are no able to distinguish among these models for infinitely long strike-slip faults on the basis of surface deformation (Fig.1.2b).

Anyway this kind of approach of studying strike-slip faults has been widely used because it can provides important informations about the fault position, locking depth of seismogenic layer and the occurring V_p below it.

1.3.1   Dislocation model code

We determine the fault geometry that best describes the observed surface deformation by mean a single rectangular dislocation in a uniform elastic half-space (Okada, 1985). The relation between data and fault parameters is simply expressed by:

$$\mathbf{d} = \mathbf{G}(\mathbf{m}) \qquad (1.1)$$

where $\mathbf{d}$ indicates data and $\mathbf{G}$ represents Green's functions non-linearly depending on $\mathbf{m}$, that is the fault parameters vector. To reproduce as better as possible the observed
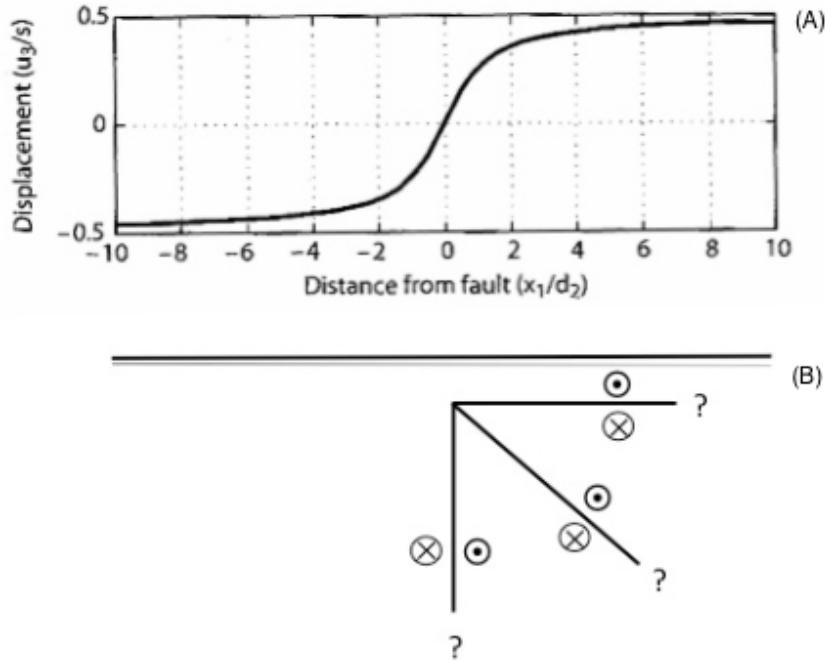
Figure 1.2: *a) Horizontal interseismic displacement; b) the deformation shown on a) is independent of the dip of the dislocation surface for a single screw dislocation. From Segall (2010, chap. 2)*

deformation we attempt to minimize the cost function WRSS (Weighted Residuals Sum of Squares):

$$WRSS = (\mathbf{d}_{obs} - \mathbf{d}_{mod})^T \times \mathbf{C}^{-1} \times (\mathbf{d}_{obs} - \mathbf{d}_{mod}) \qquad (1.2)$$

where $\mathbf{d}_{obs}$ and $\mathbf{d}_{mod}$ are the observed and modeled displacement components, respectively, and $\mathbf{C}$ is the data covariance matrix. The problem is non-linear, as the predicted surface displacements are non-linear functions of the fault geometry (Eq. 1.1). We use a constrained, non-linear optimization algorithm (Celis *et al.*, 1985; Árnadóttir & Segall, 1994; Bürgmann *et al.*, 1997) to solve for nine parameters describing the rectangular dislocation and slip-rate vector (i.e. length, width, dip, top-depth, latitude, longitude, dip-slip and strike-slip). The constrained inversion allows us to bound the solution starting from some apriori information given by structural geology and seismicity. In particular for interseismic studies it's common practice to fix length and width to high values to reproduce a wide deep buried dislocation and possibly to use tight bounds on location if the study is focused on a particular fault structure. In this way there are effectively less fault parameters to estimate and the research can be focused on the most important ones, such as locking-depth and position.

This inversion method may count for many different datasets that should be modeled jointly by the same estimated parameters. To this aim diuring the inversion different types of data are weighted each one by a factor varing from 0 to 1, avoiding that any

dataset may influence the solution more than the others. In the case of the present dissertation we have used only two type of data: InSAR and GPS velocities. The numerical superiority of InSAR dara with respect to GPS ones was confined by using this factor, that rescales the covariance matrix. In fact expanding the eq. 1.2 for the two datasets, we have:

$$
\begin{aligned}
WRSS_{TOT} &= (WRSS_{GPS} + WRSS_{InSAR}) \\
&= \|\mathbf{W}_g\mathbf{d}_g - \mathbf{W}_g\mathbf{G}_g(\mathbf{m})\|^2 + \|\mathbf{W}_s\mathbf{d}_s - \mathbf{W}_s\mathbf{G}_s(\mathbf{m})\|^2 \quad (1.3)
\end{aligned}
$$

where subscripts g and s are referred respectively to GPS and InSAR data and the weghting matrix $\mathbf{W}_{g,s}$ is a diagonal matrix in which the diagonal elements are equal to $1/\sigma_{g,s} \times w_{g,s}$, with σ is the error associated to each data and w is the *weighting factor* (varying from 0 to 1). In this approach we keep fixed $w_g = 1$ since GPS data are very accurate and they must weight as much as possible during the inversion. The value of w_s will be chosen instead evaluating how much the two datasets are well fitted jointly so that it should be assessed case by case. The particular method used in this thesis will be explained in detail on Chap. 4.

Anyway this approach has some limitations for the interseismic deformation study, since first of all it is not possible to invert for several fault structures simultaneously, because the non-linear optimization argorithm we use is not so strong to invert for many indipendent parameters. The only ways to overcome this issue are: change the optimization algorithm with a global one or perform many studies each one focused on a local area, but this is not a subject of interest for this dissertation. The other limitation is that all the observed velocity gradients are assumed to be only an elastic effect of the fault systems considered during the inversion, neglecting any contribution from the regional kinematics that concerns the independent movements of plates. This contribution could be detectable not so far from the fault trace. Looking at Fig. 1.2a it can be easily seen that the elastic signal stops to vary tens of kilometers away from the fault trace, but at the same distance the plate rotation could produce an horizontal gradient that may affect the observed data (McCaffrey, 2002). The block modeling approach described in the sections allows to avoid this problem.

1.4   Block Modeling Approach

The Block Modeling theory (McCaffrey, 2002; Meade & Hager, 2005) is a kinematic approach for which the velocity field observed by geodetic measurements is modeled considering the crust subdivided into plates, assumed as elastic rigid *blocks*, which rotate independentely with respect to a reference one. Block boundaries are represented by rectangular fault planes embedded in an elastic, homogeneus and isotropic halfspace (Okada, 1985) and their interactions caused by plate movements are associated to the observed velocity gradients. This simplified representation follows the *back-slip* concept explained by Savage (1983), which is based on the assumption that the sum of interseismic and coseismic deformation gives back the long-term motion of blocks. So rearranging the terms,

we can model the interseismic deformation as the sum of the long-term block motion and a shallow long-term slip-rate acting on opposite direction of coseismic slip sense (i.e. back-slip, see Fig. 1.3).

Thus in the BM approach the long-term block velocity is indicated by the rotational
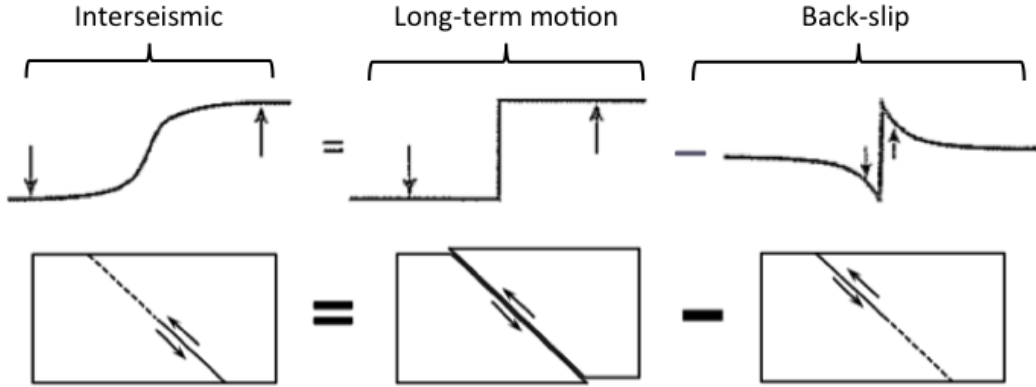
Figure 1.3: *Back-slip*

plate motion, $\mathbf{V_R}$, represented by an angular velocity vector (see eq. 1.6). Then on the shallow locked part of the crust, the elastic contribution ($\mathbf{V_E}$) within the velocity field is provided by an elastic dislocation with a slip rate equal (but with opposite sign, i.e. back-slip) to the relative movement of blocks projected on fault plane. Thus the elastic back-slip contribution is strictly depending on the rotational rates that represent the crust large-scale movements. For this reason the long-term slip rate obtained for the fault boundaries are considered "self-consistent" within the whole kinematic framework. Moreover on BM is possible to take into account also for an internal strain of blocks as an additional deformation source, $\mathbf{V_S}$, since effects of minor faults are not included in the block geometry (McCaffrey, 2005). The interseismic velocity field $\mathbf{V_I}$ is therefore modeled by the sum these three components:

$$\mathbf{V_I} = \mathbf{V_R} + \mathbf{V_E} + \mathbf{V_S}. \tag{1.4}$$

where the unknown parameters consist only in the angular velocity vectors and, if estimated, in the horizontal strain rate tensor, since $\mathbf{V_E}$ is generated by the long-term slip rate depending on the differential rotation of blocks (see eq. 1.9, Fig. 1.4a).

The wide kinematic representation of the BM is the strength of the approach, since the observed velocity field provides a kinematic framework in which the model parameters should fulfill at the same time all the velocity contributions considered. Nevertheless the limitation of this technique consists on defining apriori the block geometry and fault parameters and this leads to do strong assumptions for regions where active faults are not well identified.

However this method has been widely used to study the interseismic deformation in different tectonic frameworks, as strike-slip faults (D'Alessio *et al.*, 2005; McCaffrey, 2005;

Meade & Hager, 2005), subduction zones (Wallace *et al.*, 2004; Manaker *et al.*, 2008; Serpelloni *et al.*, 2010; Loveless & Meade, 2011; Franco *et al.*, 2012) and extended plate boundaries (Reilinger *et al.*, 2006; Socquet *et al.*, 2006; Meade, 2007b) providing long-term fault slip-rates useful to assess implications for seismic potential of each region.

1.4.1 Interseismic Coupling
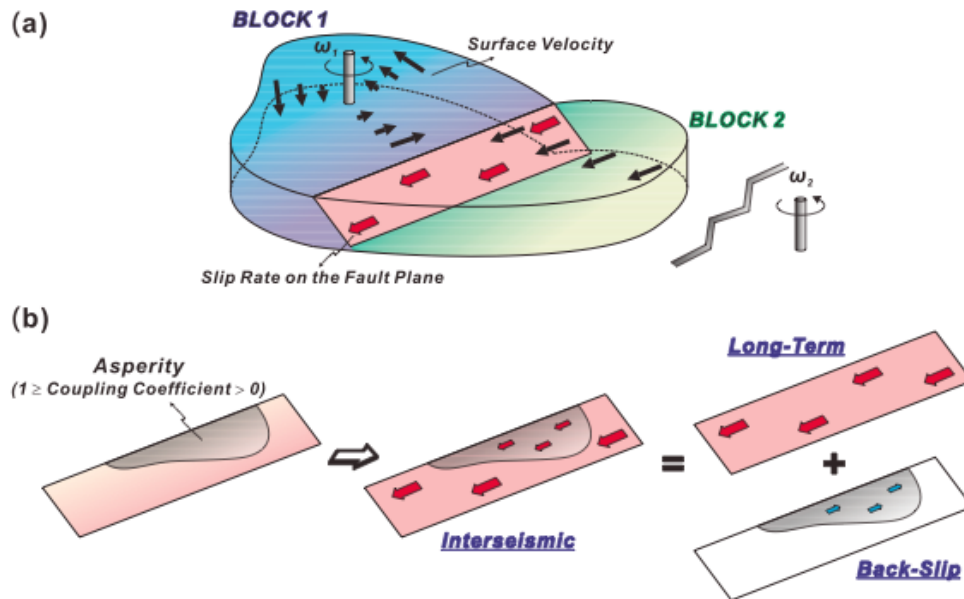
Figure 1.4: *Concept of the 3D block modeling. (a) Relationship of the Euler pole location and block motion. The black thick arrows indicate the directions and magnitudes of the surface velocities in tectonic blocks. The pink plane (fault plane) is the interface between two blocks; ω means rotation rate. Red arrows denote the slip rates along the fault plane and the slip rates are derived from the velocity difference between two blocks. (b) Relationship between the longterm slip rate, backslip rate (slip rate deficit) and interseismic slip rate. Red arrows denote the slip rates along the fault plane, and the blue arrows are the back slip rates on the asperity. From Ching* et al. *(2011)*

A further tool useful to better evaluate the fault seismic potential consists on considering a spatial distribution of back-slip on the fault plane, that allows us to identify in which part of the surface the elastic contibution should occur, i.e. to distiguish between the locked seismic "asperities" from the aseismic portions where interseismic "creep" occur. Fault creep may occur gradually over a long period of time (months to years), or it may occur as episodes of displacement, called *creep events* which last from a few hours to days and include from a millimeter or less to a few tens of millimeters of displacement (Wesson, 1988). The pattern of locked asperities and creeping portions depends on spatial variations of fault friction (Kaneko *et al.*, 2010).

In the BM representation fault creep is the aseismic behavoir with which faults accommodate the relative motion of blocks, and it does not provide any elastic contribution to the surface velocity field. For this reason the variation of back-slip is assumed to be less than or equal to the long-term slip rate and it may be considered as the actual slip occurring on fault plane during the interseismic phase (see Fig. 1.4b).

A simplified approach to evaluate the slip occurring on a fault plane consists in defining the *interseismic coupling* degree ϕ, as the ratio of the slip deficit v_i (i.e. back-slip) during the interseismic period divided by the long-term slip derived from the relative motion of blocks V_p:

$$\phi = \frac{v_i}{V_p} \tag{1.5}$$

In eq. 1.5, ϕ varies between 0 (there is no slip deficit), where the fault surface is said uncoupled and 1, corresponding to a fully coupled fault patch that identifies an asperity (see Fig. 1.4b). Intermediate values for the coupling coefficient indicate complex zones that accommodate the relative motion by both seismic rupture and creep, or spatial heterogeneity of locked patches and creeping patches at a smaller scale.

To model the coupling distribution, the fault plane is subdivided into patches each of which may have independent back-slip components. Considering this further complexity the number of unknown parameters significantly increases with respect to a classical BM approach, giving rise to some issues to deal with, like evaluating if the inversion method is consistent with an under- or over-determined problem (Menke, 1989) and the use of a regularization constraint for the coupling solution to avoid a scattered, unrealistic slip distribution. These topics will be discussed in more detail in the next paragraph that describes the BM code used in this thesis and the changes applied to solve for these problems.

1.4.2   Parametric Representation

In this thesis we have used the BM code of Meade & Loveless (2009), where they present the analytical approach to model GPS velocity data. I will report some important mathematical passages to demonstrate pro and cons aspects of their approach and the necessity to apport some changes to it.

Their approach uses spherical coordinates to describe the block rotation by means of a Cartesian rotation vector $\mathbf{\Omega}$ passing through the center of the Earth, as $\mathbf{V_B} = \mathbf{\Omega} \times \mathbf{x}$, where $\mathbf{x}$ represents the Cartesian station coordinates. This relation can be written in terms of a linear operator:

$$\mathbf{V_B} = \mathbf{P_V} \mathbf{G_B} \mathbf{\Omega} \tag{1.6}$$

where $\mathbf{P_V}$ is the Cartesian to East-North-Up (ENU hereinafter) conversion tensor and $\mathbf{G_B}$ is the cross product tensor. Since the rotational velocities are tangent of the Earth's surface, there's no vertical component in the velocity field reducing the problem to an horizontal plane deformation case. Thus in this BM configuration, the vertical component of each velocity contribution is not taken into account, modeling only horizontal velocity data.

To describe the elastic contribution due to the locking of faults during the interseismic phase, they use a slip-rate deficit occurring on faults (see Par. 1.4, Fig. 1.3) and depending on the differential velocity predicted by the relative rotation of bounding blocks, given by:

$$\mathbf{V_E} = \mathbf{G_0 s} \tag{1.7}$$

where $\mathbf{G_0}$ gives the partial derivatives of the elastic Green's functions (Okada, 1985) and $\mathbf{s}$ is the vector of slip components, that is expressed in terms of relative rotation of bounding blocks (a and b in this case):

$$
\begin{aligned}
\mathbf{s} &= \mathbf{P_F P_V}[\mathbf{G_B \Omega^{\{a\}}} - \mathbf{G_B \Omega^{\{b\}}}] \\
&= \mathbf{P_F P_V G_{B\Delta V}} \left[\begin{array}{c} \mathbf{\Omega^{\{a\}}} \\ \mathbf{\Omega^{\{b\}}} \end{array} \right]
\end{aligned} \tag{1.8}
$$

where the matrix $\mathbf{P_F}$ projects the differential east and north block motion velocity into fault-slip components. It is worth to note that for any given fault segment the approach allows only two slip components, strike slip and either dip or tensile slip for dipping or vertical faults, respectively. This choice is based on the fact that tensile-slip dislocation sources may serve as approximations to dipping reverse and normal faulting structures (Souter, 1998) and this property may be useful in the definition of block bounds in those cases where the fault geometry is undefined. Substituing eq. 1.8 in eq 1.7, we obtain the elastic deformation depending on rotational parameters:

$$\mathbf{V_E} = \mathbf{G_0 P_F P_V G_{B\Delta V} \Omega} \tag{1.9}$$

To allow for a spatially variable elastic coupling, the approach replaces fault planes with the parametrization of surfaces by mean Triangular Dislocation Elements, TDEs (Comninou & Dundurs, 1975; Jeyakumaran *et al.*, 1992; Meade, 2007a). For a fault segment with a TDE mesh, in place of $\mathbf{V_E}$, the contribution to the elastic deformation field is obtained summing the contribution produced from each singular TDE:

$$\mathbf{V_T} = \mathbf{G_T t} \tag{1.10}$$

where $\mathbf{G_T}$ is a matrix of partial derivatives of Green's functions describing displacements due to unit slip on a TDE (Comninou & Dundurs, 1975; Jeyakumaran *et al.*, 1992; Meade, 2007a) and $\mathbf{t}$ is the vector of TDE slip components.

Finally the approach, as already mentioned, allows to estimate an intrablock deformation that may represent faulting behavior at a scale smaller than that represented in a particular model and possibly additional deformation processes not taken into account. The intrablock strain for each block is given by:

$$\mathbf{V_{\dot{\epsilon}}} = \mathbf{G_{\dot{\epsilon}} \dot{\epsilon}} \tag{1.11}$$

where $\dot{\epsilon}$ is the horizontal strain rate tensor, referred to the reference coordinates (where the magnitudes of the velocities due to strain are zero) by mean the tensor $\mathbf{G_{\dot{\epsilon}}}$.

Summing all the contributions listed up to here, the interseismic velocity $\mathbf{V_I}$ (eq. 1.4) can be rewritten for this approach as this complete statement:

$$
\begin{aligned}
\mathbf{V_I} &= \mathbf{V_B} - (\mathbf{V_E} + \mathbf{V_T}) + \mathbf{V_{\dot\epsilon}} \\
&= [(\mathbf{P_V G_B} - \mathbf{G_0 P_F P_V G_{B\Delta V}}) \quad -\mathbf{G_T} \quad \mathbf{G_{\dot\epsilon}}]
\begin{bmatrix} \mathbf{\Omega} \\ \mathbf{t} \\ \dot\epsilon \end{bmatrix}
\end{aligned}
\qquad (1.12)
$$

This forward expression explicits the linear relationship between observed interseismic velocity and the unknown model parameters, i.e. $\mathbf{\Omega}$, $\mathbf{t}$ and $\dot\epsilon$. If all of those contributions are considered within a BM inversion, the chanche to fall in an under-determined problem is quite elevated and in order to solve for a unique solution a regularization of the problem has to be applied (Menke, 1989) imposing some constraints to the unknowns. These bounds can consist of:

- apriori information on long-term fault slip rates, that may be provided by geological estimation;

- application of a smoothing operator to TDE slip vectors to take-down the roughness of the coupling distribution (Harris & Segall, 1987), to this aim the estimate of the second spatial derivative (discrete Laplacian) of the slip distribution is required;

- up- and/or down-dip zero slip constraints for TDEs, since low coupling degree is expected along shallower and deeper portions of the plate boundary because of high pore pressure due to the existence of water and low viscosity due to high temperature, respectively (Ito *et al.*, 1999). For the latter reason in a BM inversion forcing the coupling solution to taper to zero at the bottom depth, as effect of the lithospheric brittle-ductile transition, may be acceptable.

All of these further constraints are considered within the general definition of the BM representation, for which more specific details are reported in Appendix A. Each of these constraints provide a contribution for the estimation of the final solution by means of a specific weighting factor, that controls the influence of the constraint in the final solution. The factor more used during the analysis reported in this thesis is that one correlated to the smoothing operator, that we call *smoothing factor*, β. This factor has been evaluated in each case of study of this dissertation, in order to obtain a regularized coupling distribution that at the same time provides a good fit of the observed velocities. The method used for this purpose will be defined case by case.

1.4.3 Inversion Techniques

The authors of the original BM code we use, Meade & Loveless (2009), have choosen to use the Linear Least-Squares (LLS, see Appendix A) problem solver because it allows for an analytic solution given a fault-network configuration, and the calculation of the model sensitivities and formally propagated uncertainties is straightforward (Meade & Loveless,

2009). However this approach is not really correct, since the linear least-squares solver is strictly referred only to real over-determined problems (Menke, 1989), in which the data-to-unknown ratio must be at least greater than one. This condition may be verified mainly when any contribution from TDE-slip distribution is not considered. For this reason the LLS method is a reliable solver mainly for BM inversions estimating long-term slip rates for rectangular fault without any TDEs. However the LLS method has been already used for interseismic coupling estimation by Loveless & Meade (2010), where they obtain a well regularized coupling solution by mean a suitable choice of the smoothing factor β value for which the slip magnitude of TDEs are physically meaningful with respect to the long-term plate motion as estimated using the block modeling approach.

Unfortunately, this approach to estimate the coupling distribution has been proven to be inappropriate for the specific studies reported in this thesis. In fact in the attempt to vary β values in order to obtain a slip distribution with a magnitude comparable to the long-term slip rates, the final solution of coupling presents always an over-smoothed pattern, loosing the ability to identify any clear definition of locked asperities. The reasons for this unexpected problem originate from the assumption itself of using the LLS method for a regularized problem. In fact the LLS solver is the most reliable one only if the problem is overdetermined, that is, if we have more data than the unknown parameters. On the other hand regularized problems are not actually over-determined, neither under-determined (Menke, 1989), because after regularization we have same data and unknowns as before the regularization, the difference is that, as an artifact, we apply some constraints to the final solution. If we have a good data distribution (i.e. they reveal a clear tectonic pattern), a model geometry reasonably simple (i.e. few blocks) and an elevated signal-to-noise ratio (i.e. interseismic velocities of several cm/yr), then the regularization is just an help for the LLS method to converge to a solution already constrained by data themselves (e.g. Loveless & Meade, 2010). But those conditions are not satisfied in the complicated tectonic framework of the Italian peninsula, where many blocks are needed to take-into account for several active fault-systems, that is also characterized by a low signal-to-noise ratio (velocities of few mm/yr). In this context rotational parameters are still well constrained by the data (covering adequately all blocks), but it is not so for the coupling distribution, for which there isn't any kind of kinematic constraint and where the slip magnitude basically depends on the few stations just over the TDE mesh. The only constraint that may act on the slip-deficit distribution is the laplacian operator, but high values of β are needed in order to have slip on TDEs comparable with long-term slip-rates, and then the coupling distribution turns out to be too smoothed.

To avoid this annoying problem I have modified the code in order to minimize the cost function WRSS (eq. 1.2) for the generalized problem that considers also the regularization (i.e. solving for a constrained, linear least squares problem) using an algorithm based on the preconditioned conjugate gradient methods (Coleman & Verma, 2001). In this manner it is possible to force the solution to have values within prescibed boundaries, and using the long-term slip rates obtained from the relative rotation of blocks, it is possible to define a slip range in which TDE slip-deficit may vary. Moreover the smoothing parameter recovers its principal aim that consists in controlling the relative importance of minimizing

the cost function versus minimizing the roughness of the slip (Harris & Segall, 1987; Du *et al.*, 1992). The strength of this approach will be demonstrated during each application comparing results obtained from LLS solver and from the Linear Constrained Algorithm (LCA hereinafter).

1.5   Integration of modeling techniques

We have integrated BD and BM approaches in order to study the interseismic deformation measured across the Mattinata Fault on the Gargano Promontory. The presence on that area of a fairly good numbers of GPS stations and a dense dataset of InSAR velocities (see Chap. 2) brings us to take advantage of all available tools to evaluate fault parameters and interseismic coupling occurring for that particular fault system. For this reason we have used the dislocation model approach to realize a constrained inversion in order to estimate the fault plane parameters and then we have used that geometry within a block model to evaluate the interseismic coupling distribution for the studied fault (see Chap 4).

The positive aspects of this two-step procedure consist in taking advantages of both BD and BM methods, i.e.:

- BD: no regional kinematic constraint and modeling of data with one or very few faults;

- BM: blocks boundaries fixed with *a-priori* fault parameters.

For a specific fault the kinematic constraint provided by the BM approach allows us to detect the spatial variation of coupling consistent with the assumed kinematics of the region. Moreover the constrained inversion gives reliability to the estimated fault parameters for the following step of coupling degree estimation, that may be affected by the fault geometry provided. Anyway this particular approach can be used also having only GPS data, but it requires a good spatial coverage detecting details of the horizontal velocity gradient across the active fault under investigation. On Chapter 4 I will describe more in detail the steps and results obtained from the integration of the two tecniques.

Chapter 2

Geodetic Measurements of Interseismic Deformation

2.1 Introduction

The ground deformation during the interseismic phase of seismic cycle is measurable by *geodetic techniques*, that take into account accurate measurements of position in any point on Earth's surface. Thanks to lately improvements of the space geodesy, these techniques provide huge amounts of measures with a millimeter precision, allowing to study interseismic deformation also at local fault scales.

These techniques produce their measures by means of artificial satellites, that send continually electromagnetic signals toward the Earth. They may be classified by the instrument platform which distinguishes the measuring method:

1. *Earth-to-space-methods*: satellites are observed with ground-based instruments (receivers);

2. *Space-to-Earth-methods*: satellites carry an instrument or sensor as a part of their payload to observe the Earth.

GPS measurements fall on the first group, since receivers located on ground stations record the position in time, whereas InSAR measures belong to the second group, since they arise from the overlap of images of the land surface acquired by the satellites themselves. These two techniques are basically complementary and one of the aims of this work is to use both jointly to get as more information as possible about the characteristics and behavior of faults during interseismic phase. In the following paragraphs, I will explain more in details how these techniques work and what kind of data have been available for these studies.

2.2   GPS data

The Global Positioning System (GPS) is a fleet of 31 satellites that are orbiting our planet approximately 11000 miles above Earths surface. It was created and developed by the U.S. Department of Defense, with originally only 24 satellites, that became fully operational in 1995.

This system provide location and time information in all weather conditions, anywhere on Earth where GPS receiver can see four or more GPS satellites. Unfortunately there are many factors that could affect the position measurements made by GPS receivers, like:

- *Atmospheric delay*: the ionosphere (the atmospheric layer 30-50 km above Earths surface) contains particles with electrical charges, which change the speed of radio signals; water vapor in the troposphere (the atmospheric layer in which weather occurs) may decrease the speed of radio signals, producing a "delay".

- *Clock errors*: GPS satellites are equipped with very accurate atomic clocks, but they are not perfect and slight inaccuracies can lead to errors.

- *Ephemeris errors*: satellites are launched into a precise orbit well above the Earth's atmosphere. The Department of Defense constantly monitors the exact altitude, speed and position of each satellite. Small changes are caused by gravitational pulls from the moon and sun and by the pressure of solar radiation on the satellites. Slight ephemeris errors over such large distances can make a difference.

- *Multipath*: when the signal arrives at the surface of the Earth, it can reflect off obstructions such as buildings and trees and therefore it takes longer to reach the receiver than it should.

- *Receiver noise*: receivers can introduce errors of their own, usually from internal noise.

Anyway the influence of these errors on measurements accuracy depends on the ability of GPS receiver to reduce it and for this purpose GPS units are divided in two main classes:

- *Handheld* GPS receivers: they are the most widespread among people, who use it for navigation, recreation, mapmaking and land planning; they calculate positions as autonomous solutions using only satellites and not allowing any correction for many error sources, therefore the accuracy of solutions is of the order of one meter.

- *Differential* GPS receivers: the position is calculated by means of at least two GPS receivers, the roving one, that continuously calculates its position from the satellites and the stationary one that compares the calculated position by satellites with its known fixed location, estimating a difference useful to correct the GPS roving measurements.

Figure 2.1: *Survey-mode GPS reciever installed during the OMBRA project to monitor the Montello area (Eastern Alps)*

The second one provides more accurate measurements than the first one and it is mostly used for geophysics, geodetic and topographic purposes. In particular to improve the measurement accuracy of the roving receiver, its phase records are proceseed and analysed in a second moment using a network of fixed ground-based reference stations to estimate the position time series and the error contributions on signal (see paragraph 2.2.1).

GPS measurements can be made mainly by means of two strategies: survey-mode (EGPS) and continuous (CGPS) sites. In the first case there's a network of geodetic landmarks fixed to the ground, on which measurement campaigns with annual or semi-annual time intervals are executed, with the benefit of having a wide number of sites with few receivers at a quite low cost (see an example on Fig. 2.1). Whereas in the second case the GPS receiver is located on a fixed geodetic monument, recording continuously signals at a rate of 30s, but this strategy is quite expensive and it needs continuous power supply. However CGPS receivers allows to record short-time deformation signals (coseismic and postseismic deformations), which it is very unlikely that EGPS ones can detect. Moreover the accuracy of measuremets of CGPS sites is much better than the one from survey-mode sites.

During the processing phase and the time series analysis, the kind of data acquisition method is obviously taken into account to obtain the best measures as possible.

2.2.1   GPS data analysis

GPS velocities have been obtained from raw data recorded by several operating networks in the Euro-Mediterranean and African regions. These data have been analyzed by adopting a three-step approach, as described on Serpelloni *et al.* (2013), which includes: (1) raw phase data reduction, (2) combination of loosely constrained solutions and reference frame definition, and (3) time series analysis.

In the first step, the GAMIT (V10.4) software (Herring *et al.*, 2010) is used on daily GPS phase observations to estimate site position, adjustments to satellite orbital parameters and time-variable piecewise linear zenith and horizontal gradient tropospheric delay parameters, applying loose constraints. During this analysis the ocean-loading and pole-tide correction model FES2004 (Lyard *et al.*, 2006) is applied and the Global Mapping Function (GMF) (Boehm *et al.*, 2006) for both hydrostatic and nonhydrostatic components of the tropospheric delay model. The IGS (International GNSS Service) absolute antenna phase center model is used for both satellite and ground-based antennas. Continuous GPS data are divided into several subnets and processed independently; each subnet share a set of high quality IGS stations, which are subsequently used as tie-stations in step 2. Survey-mode GPS networks are processed separately, adding a larger number of high quality CGPS stations, in order to reduce the average baseline lengths.

In the second step the ST_FILTER program of the QOCA software (Dong *et al.*, 2002) is used to combine all the daily loosely constrained solutions, for both CGPS and EGPS subnets, with the global and regional solutions made available by SOPAC (http://sopac.ucsd.edu), and simultaneously realize a global reference frame by applying generalized constraints (Dong *et al.*, 1998). Specifically, the reference frame is defined by minimizing the horizontal velocities of the IGS core stations (http://igscb.jpl.nasa.gov), while estimating a seven-parameter transformation with respect to the IGS08 realization of the ITRF2008 frame (Altamimi *et al.*, 2011).

The third step consists in the analysis of the position time series for the CGPS and EGPS stations, in order to estimate a constant linear velocity term together with annual and semi-annual seasonal components and, if present, offsets at specific epochs, adopting a white + flicker noise model, following Williams *et al.* (2004). In addition the Common Mode Error (CME) estimation is performed by applying the PCA method of Dong *et al.* (2006). In this way the position time series are filtered, reducing the daily scatter and allowing for more accurate determinations of time series.

In the last step data from CGPS and EGPS stations with an observation period longer than 2.5 years have been analyzed, as shorter intervals may result in biased estimates of linear velocities (Blewitt & Lavallée, 2002).

2.2.2 GPS velocity field

All data used in this work have been analyzed at Istituto Nazionale di Geofisica e Vulcanologia (INGV) of Bologna, following the process described above.

Velocities and uncertainties of CGPS stations located on tectonically stable domains of
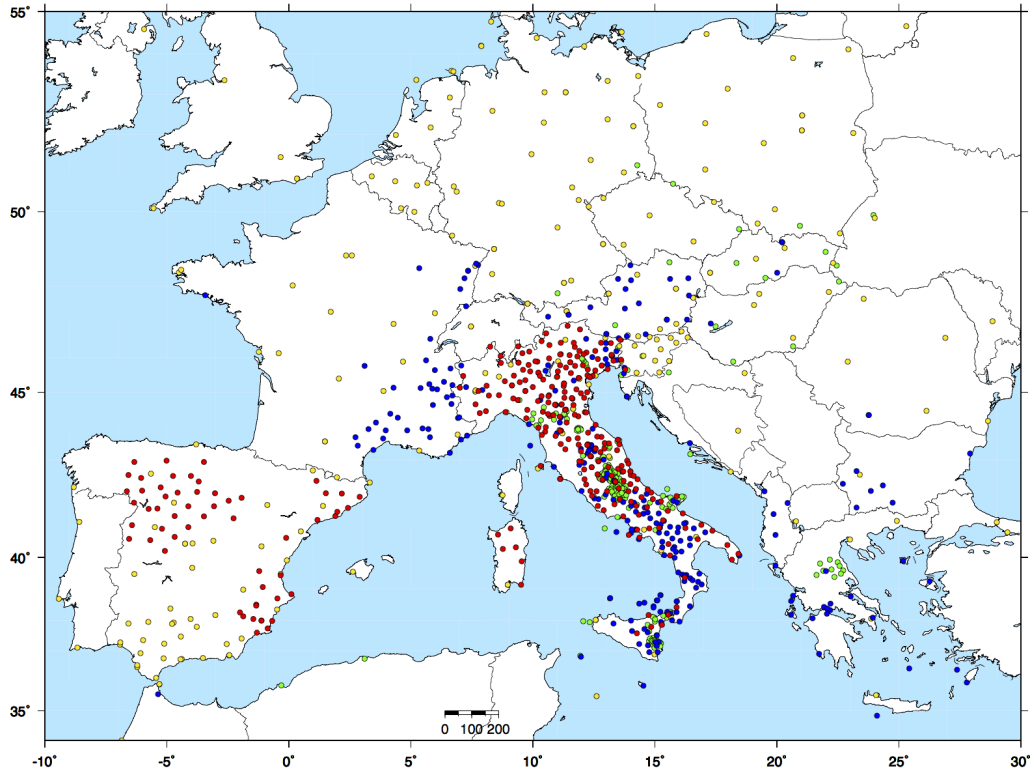

Figure 2.2: *GPS stations in the Euro-Mediterranean region clustered by type. Blue: geophysical stations, red: topographic stations, yellow: geodetic stations and green: survey-mode stations.*

the Eurasian and Nubian plates have been used to estimate their Euler rotation poles with respect to the IGS08 frame. They are totally almost 1700 sites of which more than 1400 continuous and 250 survey-mode. Fig.2.2 shows the GPS sites used: they belong to different types of networks for the Euro-Mediterranean region. It is worth to note how it is important for the Italian peninsula to integrate different networks to have a quite good coverage of the territory by GPS sites. It should be preferred to consider only geophyisics and geodetic networks for the accuracy and reliability of their data, since their purpose is exactly to measure the position with high precision and continuity through time. On the other hand we use also topographic networks, created to provide data for navigation or cadastral purposes, whose data quality could be worse. Anyway, after the processing phase, the quality of each data is represented by the error associated to it.

The final GPS velocity field is calculated with respect to Eurasia fixed frame (as shown

on Fig.2.3) indicating for the Italian peninsula a widespread deformation of the order of few millimeters per year. This huge quantity of data has been selected accurately for each study presented in this thesis, in order to make the most the available data.
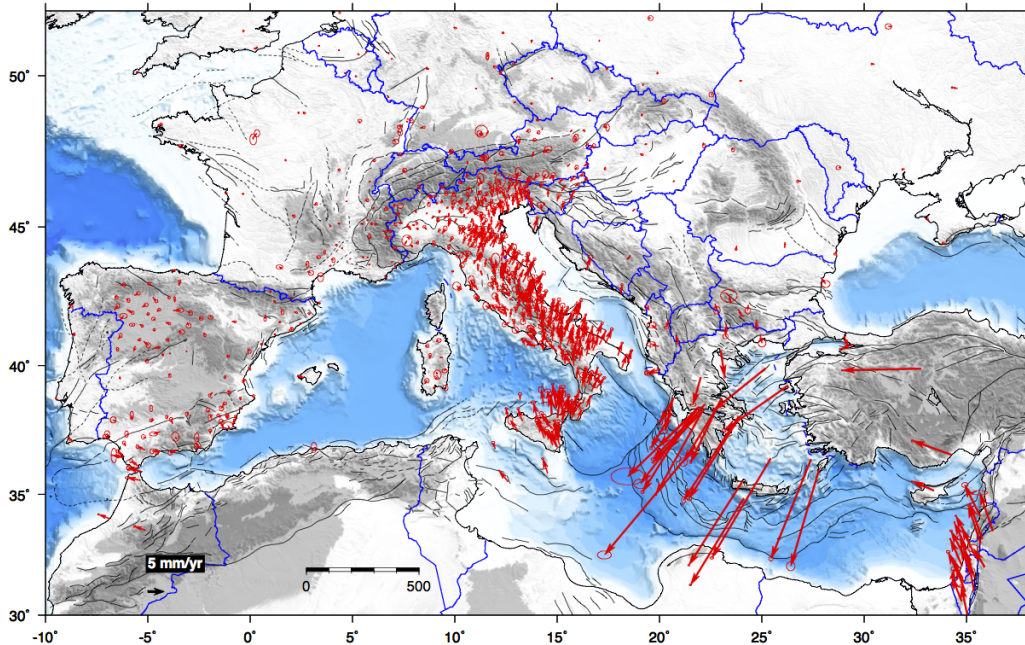

Figure 2.3: *GPS velocity field in the Euro-Mediterranean region with respect to Eurasia fixed frame.*

2.3   InSAR data

2.3.1   SAR images

Synthetic Aperture Radar (SAR) is a technique that allows to acquire images of the Earth's surface from a satellite. It uses the Radar (Radio Detection and ranging) imaging remote sensing technique that can provide 2-dimensional (along-track and across-track dimension) images of the earth by transmitting microwaves to the ground and receiving the back-scattered signal. Such a real-aperture radar in space would have a spatial resolution of about 5-10 km, limited by the power and size of the footprint of the radar beam (Bürgmann *et al.*, 2000). Fig. 2.4 shows a simplified acquisition geometry of a side-looking real-aperture radar: the beam footprint is generated by the signal arriving at a fixed incidence angle, which corresponds the slant range direction (shortest distance from the radar antenna to the centre of the ground footprint). This direction is known also as Line of Sight (LOS) of satellite and usually InSAR data of displacement, at the end of processing, are provided along it.
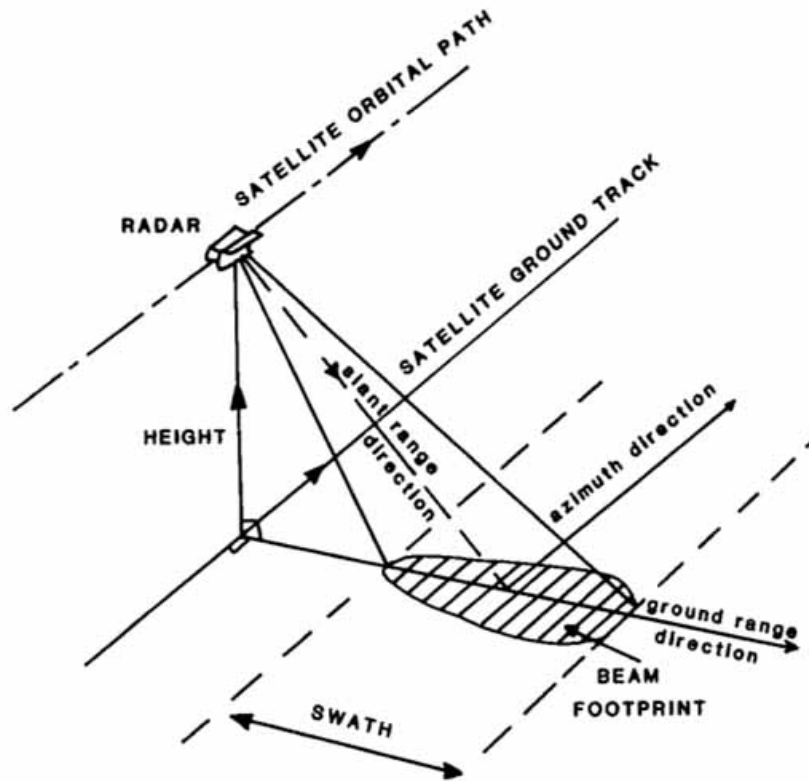
Figure 2.4: *Schematic representation of real-aperture radar acquisition.*

Nevertheless SAR method can image the surface with a pixel resolution of 10-20 meters, getting information of both the amplitude and phase from each image pixel. This increased resolution is achieved combining complex processing techniques with satellite orbit information. Fine resolution in the cross-track direction is obtained by using a radar signal of high bandwidth, which improves the differentiation of radar echoes from closely spaced targets in the range direction. In the along-track direction the resolution increased receiving back-scattered signals from a particular point target on the ground, illuminated by overlapping footprints of successive pulses and the Doppler effect of the radar signal is used to differentiate the targets. This technique allows to simulate a very big receiving antenna, known as the sinthetic aperture.

The geometry acquisition of SAR satellites consists in following sun-synchronous orbits inclined of few degrees ($\sim 10^o$) with respect to the Earth's axis, wherein each successive orbital pass occurs at the same local time of day. This particular combination of terrestrial rotation and satellite motion is able to cover each area of the planet by means of two distinct acquisition geometries (see Fig. 2.5): ascending orbit-track (moving northward) and descending orbit-track (moving southward). The positive aspect is that using these two distinct acquisitions it is possible to estimate the horizontal ambiguity on ground

deformation, since their line-of-sight on East-West direction is opposite.

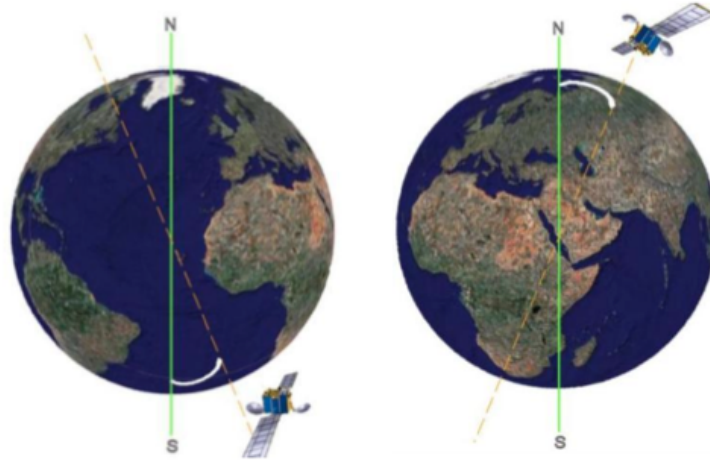After an appropriate processing, the SAR image consists on a two-dimensional record of

Figure 2.5: *Picture of ascending and descending orbital motions with respect to the Earth's axis.*

both the amplitudes and the phases of the returns from targets within the imaging area. The amplitude contains information about the target reflectivity, whereas the phase encodes changes at the surface as well as a term proportional to the range to the target. This second content is pretty much random, since the phase signal is subject to delays caused by the atmosphere, and shifts due to the interaction with elementary targets contained into a pixel. Useful information can be extracted only differencing the phase of the same pixel between two different SAR images: this is the principle of radar interferometry.

2.3.2   InSAR technique

Interferometry of SAR (InSAR) images uses the phase information in two SAR images to determine the phase difference between each pair of corresponding image points, thus producing an interferogram. If the phase difference is calculated at the same time but with a slightly different look angles (the perpendicular distance of orbit trajectories is called "baseline"), it provides information about changes in range to targets on the ground, and thus the surface topography at the resolution of the SAR image can be recovered with knowledge of the imaging geometry (Rosen *et al.*, 2000). Otherwise if the phase difference of two images are taken from the same viewpoint, but at different times, it can precisely measure any shifts of the returned phase, which correspond to displacements of the ground in the direction of the range vector (Goldstein & Zebker, 1987). Anyway, because current satellites repeat their orbits only within several hundred meters, radar interferograms commonly contain both topographic information as well as surface motions. Using a digital elevation model (DEM) it's possible to remove the topographic

phase contribution from the final interferogram to measure the ground deformation.
The resultant interferogram contains the following effects that limit the accuracy: 1) inaccurate orbit information; 2) imprecise DEM; 3) atmospheric and ionospheric delay. The first two error contributions could be easly reduced during the phase processing using the latest updated DEMs and accurate orbital parameters of satellites. On the other hand the atmosferic artifacts are not temporally stable nor homogeneous, and the variable path delay can limit the InSAR accuracy for deformation measurements (Goldstein, 1995; Massonnet & Feigl, 1995). Anyway the deformation signal is slowly variable with time, and it is possible to isolate the deformation pattern with respect to the atmospheric one.

Similar to GPS, the detailed analysis on the InSAR phase data is focused on resolving the temporal behavior of the surface deformation. For the steady-state interseismic deformation, a solution is to average multiple independent interferograms over long time periods, a method named *stacking* (Sandwell & Price, 1998) and generating for each image pixel a time series of phase. Time series analysis allows for the mitigation of atmospheric artifacts, taking advantage of the temporally uncorrelated nature of atmospheric delay patterns. With a big amount of interferograms, Differential InSAR (DInSAR) measurements of deformation are relative: only the deformation gradient is observable and not the absolute value of deformation. Anyway the accuracy and the dense coverage over the earth's surface of DInSAR data are adequate to make it a fundamental geodetic tool to monitoring the ground deformation.

2.3.3 DInSAR processing

The multitemporal DInSAR technique is an approach that was developed with the aim of monitoring deformation phenomena characterized by continuous deformation in time and small deformation rates, like interseismic and postseismic deformation, landslides, subsidence or volcanic uplift. For this purpose numerous techniques of InSAR time-series analysis have been developed, with the aim to obtain during the interferograms staking a good phase coherence for each pixel with high interferometric correlation.

The correlation is a quantity varing from 0 to 1 and it represents how a pixel can reflect an electromagnetic wave, evaluating the coherence of the back-scattered phase in time. It is influenced by many factors that can be lumped together on two groups: factors from measuring tecniques and from ground variation. In the first group we can consider the time interval of SAR images acquisition (as larger the interval is, as more chances are that the scattering properties of pixels could change) and the geometric decorrelation due to baselines among satellites positions during SAR acquisition, recording information also about topography (see paragraph 2.3.2). In the second group there are factors that mainly concern with the nature of the pixel itself. The pixel reflectivity from natural terrain is generally considered as the coherent sum of returns from many individual scatterers within any given resolution cell. Factors varying in time could increase the decorrelation (Zebker & Villasenor, 1992), as: vegetation, erosion, steep slope of topography and building construction. The decorrelation is a big problem in DInSAR measurements processing because pixels with low correlation are rejected.

Currently there are generally two types of InSAR time-series methods: the Permanent Scatterer (PS) method and the Small-Baseline Subset (SBAS) method.

The PS method (Ferretti *et al.*, 2001) identifies point scatterers that are coherent over time regardless of the baseline limitation which produces for these scatterers small phase variations. The subsequent procedure is aimed to maximize the correlation by jointly estimating the phase signal from the deformation, the error in digital elevation model and the atmospheric delay. PS are typically buildings, metallic structures or outcrops of rock without vegetation and if they are well distributed across an image, this method allows for deformation studies even in quite vegetated areas. However this technique is strictly dependent on the presence of stable scatterers, that are not uniformly distributed on the Earth's surface.

The SBAS method (Berardino *et al.*, 2002) uses the interferograms with small perpendicular baselines to minimize the noise due to spatial decorrelation and topography. The interferograms are combined on a minimum-norm criterion of the deformation velocity, applying the singular value decomposition (SVD) method. The approach solves also for an estimate of the topographic error and the filtering of the atmospheric phase artifacts on the computed spacetime deformation measurements, following the solution developed for the PS technique (Ferretti *et al.*, 2001).

During each InSAR time-series processing methods, there's an important step in which phase measures (ranging from $-\pi$ to π) needs to be converted to represent continuous topography or surface deformation. This procedure is called phase *unwrapping* and it should be executed carefully to solve the phase ambigiuty during conversion. An error during this step means adding a value of 2π to the phase and it corresponds to a significant error for the final displacement estimation. The only way to reduce the probability to run into a phase unwrapping error is to choose interferometry pairs with small baselines and short time intervals providing images with as high coherence as possible.

Because of the errors in the DEM, of incomplete orbital signal removal, or residual atmospheric signal, it is possible that, at the end of the time-series processing, some artifacts are still present. Moreover the plasma in the ionosphere can alter the refractive index and cause a frequency-dependent phase shift on microwave signals. In most cases, these residual signals produce a pattern like planar or quadratic ramps mainly in the range direction. Their order of magnitude is often comparable to the expected tectonic signal, so that a residual ramp removal is necessary to improve the accuracy of the ground deformation measurements.

The final product achieved by DInSAR time-series processing is a 2-dimensional map of displacement rates along the look direction and it is not possible to determine the full three-dimensional velocity vectors. Thus, given typical signal incidence angles of $15^o - 45^o$ from vertical, InSAR has good sensitivity to vertical displacements but is less sensitive to horizontal motions perpendicular to, and cannot resolve motions parallel to, the approximately north-south-directed satellite track. To measure an additional component of the displacement vector, we need to combine information from interferograms from both ascending and descending (see paragraph 2.3.1) orbit tracks or consider data from multiple satellites having similar look-angle.

2.3.4 DInSAR-SBAS data for the Gargano Promontory

The DInSAR data available for the analysis that will be presented in this thesis have been processed at Istituto Nazionale di Geofisica e Vulcanologia (INGV), section of Roma1, using a variant of the multitemporal SBAS InSAR technique described by Lopez-Quiroz *et al.* (2009) and they will refer to Pezzo *et al.* (2014) (under revision).

They have used images from ERS and ENVISAT-ASAR satellites since their range directions are pretty comparable. They have processsed for the ascending orbits 46 images and for the descending ones 88 images, which have a time interval respectively of 13 years (from 1995 to 2008) and 18 years (from 1992 to 2010). They have generated more than 100 interferograms for both kinds of tracks with a maximum temporal baseline of 1200 days and a maximum spatial baseline of 200 m. They have removed the topography contribution using the 3 arc-second SRTM digital elevation model (Farr *et al.*, 2007). The inversion method used for the unwrapped phases solves for a system of linear equations in a least-squares sense, using a linear phase model to connect independent groups of images (Lopez-Quiroz *et al.*, 2009). At the same time they have estimated the residual topographic errors. The atmospheric propagation contribution was reduced by high-pass filtering in time and low-pass filtering space.

For the most coherent pixels (correlation greater than 0.7) they have recovered displacement time-series in the radar LOS direction (from ground to satellite) for ascending and descending orbits, estimating for each one the mean ground velocities with an accuracy of $1 \text{ mm} \times \text{yr}^{-1}$, in agreement with Casu *et al.* (2006) (see Fig. 2.6).

Combining ascending and descending velocity maps is possible to solve for the ambiguity
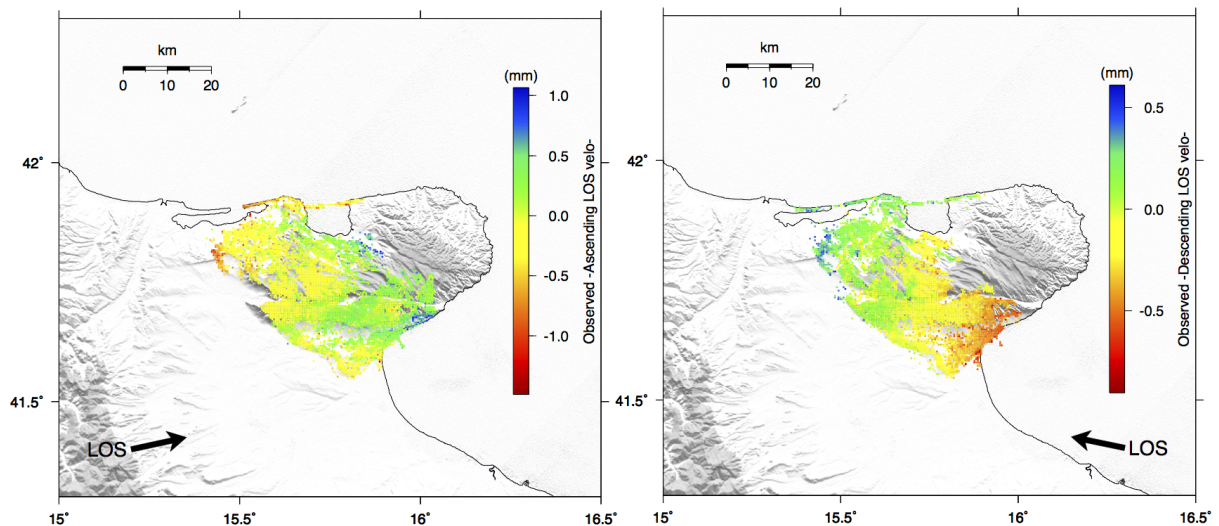

Figure 2.6: *Ascending (left panel) and descending (right panel) velocity maps on Line-of-Sight direction, indicated by the LOS vector; positive values indicate pixels approaching to satellite then negative ones correspond to moving away sites. The unit of measure of the velocities is mm/yr, and not mm as wrongly reported in map.*

between horizontal and vertical components of LOS velocities, but it is not possible to re-cover all the 3D components since there are only two measurements for each site. Because satellite orbits are inclined with respect to Earth's axis (as described on paragraph 2.3.1), the system is almost blind on North direction and contributions on that direction may be considered negligible in the LOS displacements. The combination is achieved solving for a linear system of two equations with three unknowns (Hunstad *et al.*, 2009), one of which is assumed zero. Fig. 2.7 shows the final DInSAR velocity field for the East-West
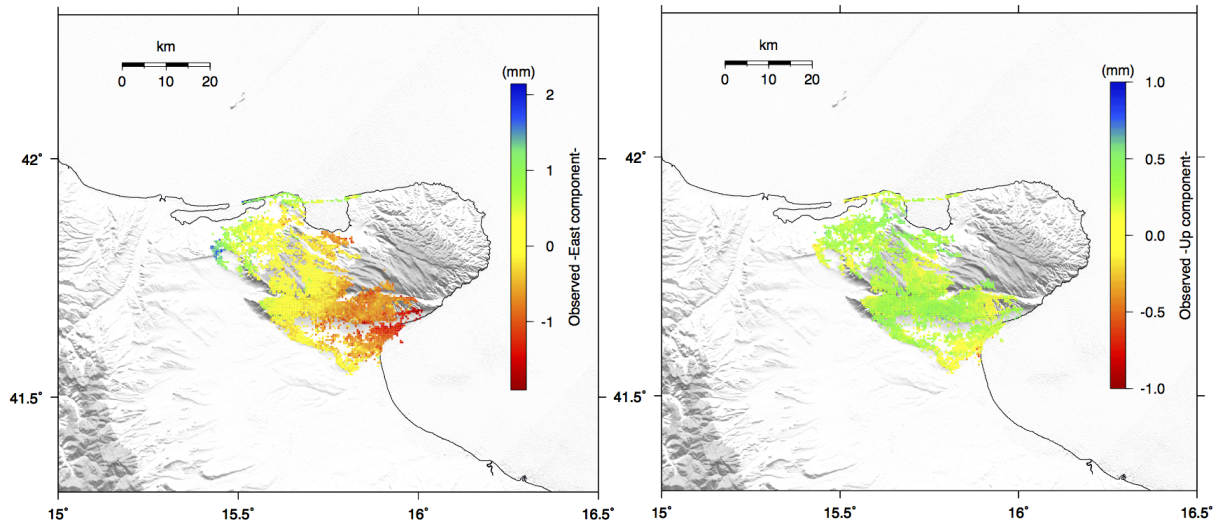

Figure 2.7: *Velocity map on East-West direction on the left (eastward is positive) and vertical long-term component (upward is positive) on the right. The unit of measure of the velocities is mm/yr, and not mm as wrongly reported in map.*

direction (left panel) and the estimated contribution in vertical direction (right panel). The first one presents a NW-SE gradient of few millimeters, while the second one doesn't show any particular pattern except for a signal almost flat demonstrating that no vertical effect (i.e. local subsidence) may have affected the horizontal signal.

2.4 GPS and InSAR data: complementary feautures and open issues

The positive aspects of GPS measurements consist in providing data for specific known points and anchored to a well-defined terrestrial reference frame. Otherwise the negative ones are related to the impossibility to have so many GPS instruments to obtain an ade-quately dense coverage of the ground and the corresponding high costs of the equipments. On the other hand, the InSAR techniques can provide spatially dense data for many worldwide areas at a relatively low costs that concern mainly the necessity of computing resources. Nevertheless during InSAR processing there are numerous factors (i.e. atmo-

phere, baseline, unwrapping step, etc...), that may affect the final solution, introducing errors difficult to be removed, and often the only way is using an indipendent estimation of an additional ramp (see paragraph 2.3.3). Moreover InSAR data indicate velocities relative to a local pixel of the frame, choosen as a starting point during the unwrapping step and they need to be compared with GPS measures to be referred to some global reference frame.

The complementariety of these two techniques has led immediately to seek a method to make them comparable, i.e. solving for non-corrected errors and anchoring them to the same reference frame. This can be achieved estimating a linear ramp signal to be removed from the InSAR data, in order to attach them to the GPS velocities that are referred to a well-defined terrestrial reference frame. The linear relation between GPS and InSAR velocities is given by:

$$V_{GPS}^i = V_{SAR}^i + [1 \quad lon_{SAR}^i \quad lat_{SAR}^i] \begin{bmatrix} a_1 \\ a_2 \\ a_3 \end{bmatrix} \tag{2.1}$$

in correspondence of a pixel very close to a GPS station, and a_1, a_2, a_3 are the linear parameters, where a_2, a_3 represent the inclination of the planar signal that recovers orbital and atmospheric non-corrected errors for InSAR data and a_1 is the offset between InSAR and GPS measurements due to the different reference frames. To estimate these three parameters we need to have at least three GPS stations placed within the InSAR frame to avoid an under-determined situation. In the event that GPS stations are more than three, we suppose that it should be more accurate to consider all of them during parameter estimation rather than choosing only three of them and loosing information. For this reason we decide to use (for the case that will be descibed in Chap. Gargano) a linear least-squares solver, and evaluating the misfit between the two datasets we have considered for each GPS station the mean velocity of the falling pixels within a variable distance radius from the station. This method has been defined in order to avoid to include outliers pixels on ramp estimation and the intersting results obtained with this approach will be presented in Chap. 4.

Chapter 3

Interseismic coupling for the Alto Tiberina Fault from GPS velocities

3.1 Introduction

The Umbria-Marche Apennines are characterized mainly by SW-NE oriented extensional deformation, as documented by geodetic (D'Agostino *et al.*, 2009), geologic (Tondi, 2000; Boncio & Lavecchia, 2000b) and seismological (Pondrelli *et al.*, 2006) data. Most of major historical and instrumental earthquakes occurred mainly on the western side of chain, bounded by west-dipping buried high-angle normal faults (Boncio & Lavecchia, 2000a; DISS, 2010; Rovida *et al.*, 2011). Moreover recent studies about the northernmost part of Umbria-Marche region show seismic and tectonic activity (Chiaraluce *et al.*, 2007; Hreinsdóttir & Bennett, 2010; Mirabella *et al.*, 2011) in correspondence of the Alto Tiberina (AT) low-angle normal fault (LANF), which is widely documented by geological data (Brozzetti, 1995; Boncio & Lavecchia, 2000b; Collettini *et al.*, 2000) and deep seismic reflection profiles (CROP03 Barchi *et al.*, 1998; Pauselli *et al.*, 2006). The supposed detachment of AT fault is an interesting case in which crustal extension could be driven by a LANF, considered by "Andersonian" theory as averse to faulting. Nevertheless which of the known fault systems play a major role in accommodating the extension, and which are the modes (seismic VS aseismic deformation) this extension is taken up, is still a debated topic.

In this context GPS measurements may provide important information on the occurring active extension indicated by velocity gradients. During last years in Umbria-Marche Apennines close to Gubbio fault (GuF) a dense network of continuous GPS stations (section 2.2.2), belonging to the RING-INGV network, has been installed, improving significantly the spatial resolution of the detectable geodetic deformations. Using the kinematic block modeling approach (section 1.4) we evaluate which particular fault systems may justify the observed velocity field in this sector of the Apennines, and in particular we would demonstrate the active kinematic role of the Alto Tiberina fault (ATF) within this context.

This analysis has been developed considering for the ATF surface the possibility to es-

timate the distribution of interseismic coupling (IC) degree (section 1.4.1) within the auto-consistent kinematic BM approach. This estimation will be performed with both inversion techniques implemented in the BM approach (section 1.4.3) to verify limits and improvements obtaind with the modified BM method. At the end, the data resolution ability of the final coupling degree distribution has been evaluated by means of several checkerboard test.

3.2   Seismo-tectonic framework

The northern Apennines are characterized by a NE-verging thrustfold belt that has arisen as a consequence of the collision between the European continental margin and the Adriatic lithosphere (Alvarez, 1972; Reutter *et al.*, 1980). From the Oligocene to the present-day, the area has experienced two phases of eastward migrating deformation: an early compression with eastward directed thrusting and a later phase of extension (e.g., Elter *et al.*, 1975; Pauselli *et al.*, 2006) that now involves the Central Appennines. In the western part of the Umbria-Marche Apennines, the Alto Tiberina (AT) low-angle (dip $< 30^o$) normal fault (LANF) (Barchi *et al.*, 1998; Boncio & Lavecchia, 2000b; Collettini, 2002), and the associated high-angle antithetic structures (Boncio *et al.*, 2004, and references therein) accommodate the extensional deformation within the brittle upper crust (Figure 3.1). The active extension occurring in the ATF is proved by several geological and geomorphological evidences (Cattuto *et al.*, 1995; Delle Donne *et al.*, 2007; Brozzetti *et al.*, 2009). The dimensions and position of ATF are also well constrianed by the interpretation of numerous seismic reflection data (CROP03, Barchi *et al.*, 1998; Pauselli *et al.*, 2006; Pialli *et al.*, 1998), and it extends over a length of $\sim$70 km with an average inclination of 20° towards NE. Recently Mirabella *et al.* (2011) have achieved a complete 3D reconstruction of the ATF up to 12 km of depth (Figure 3.1) considering all the subsurface data avaliable (seismic profiles and boreholes).

The seismic activity of the region is characterized by a dual behavior. In fact most of the numerous historical (Rovida *et al.*, 2011) and instrumental moderate ($5 \leq M_w \leq 6$) earthquakes (Amato *et al.*, 1998) occurred in the area are related to the SW dipping high-angle normal faults (Figure 3.1). Whereas microseismic surveys conducted in 1987 (Deschamps *et al.*, 1989) and 2000-2001 (Piccinini *et al.*, 2003) showed abundant microseismicity ($M_l < 3$), distributed along the ATF geometry (Collettini, 2002; Chiaraluce *et al.*, 2007) and within the overlying medium. This seismicity distribution cut-off by the ATF surface implies that the Umbra-Marche Appennines seismic events are primarily controlled by a structural feature (i.e. ATF fault detachment, Lavecchia *et al.*, 2002).

The active extension occurring along LANFs has been widely documented in different regions (Rigo *et al.*, 1996; Sorel, 2000; Morley, 1999; Jolivet *et al.*, 1998), but it is still a controversial topic. In fact on the basis of the Anderson-Byerlee frictional fault mechanics (e.g. Sibson, 1985), normal-slip nucleation should be prevented for LANFs, that are misoriented with respect to the regional stress field. However to explain the LANF seismic activity, some hypothesis have been proposed (Collettini, 2002, and ref-
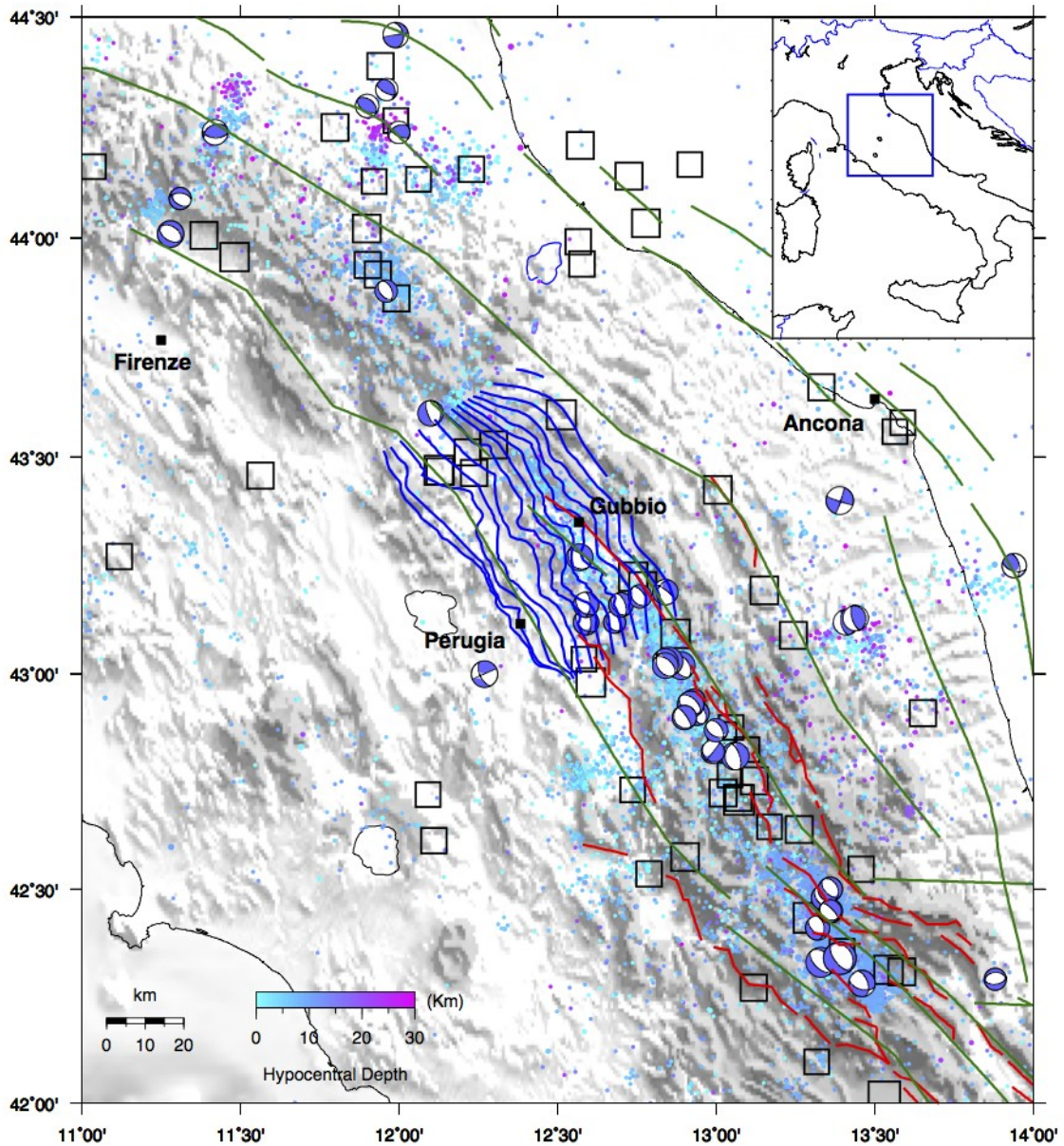
Figure 3.1: *Seismo-tectonic setting for the Umbria-Marche Apennines. Red and dark green lines indicate fault catalogs of Lavecchia* et al. *(2002) and DISS (2010), respectively, whereas the blu ones are the depth contours drawn every kilometer for the ATF proposed by Mirabella* et al. *(2011). Colored dots represent the instrumental seismicity with $M_w \geq 3$ up to 30 km of depth recorded during last 30 years and black squares show the macroseismic positions of historical events with $M_l \geq 5.5$ (Rovida* et al., *2011).*

erence therein), and the most likely one is considering the presence of pressurized fluid producing a fault frictional weakening. In fact several authors suggest that deep fluids

play a key role in triggering earthquakes (Chiodini *et al.*, 2004; Antonioli *et al.*, 2005) and control the spatio-temporal evolution of seismicity (Miller *et al.*, 2004; Antonioli *et al.*, 2005). Moreover for the ATF the presence of fluid overpressures has been documented from boreholes observations and it is generated by degassing of CO_2 saturated fluid, due to a deeply constant mantle flux (Collettini, 2002). The fluid triggering however may generate only short-time frictional instabilities, giving just a local stress variation enough for the nucleation of microseismicity (Chiaraluce *et al.*, 2007).

Nevertheless the occurring extension on ATF has been estimated to be of the order of 1 mm/yr (Collettini, 2002) and the observed microseismicity is not enough to achieve this slip rate (Chiaraluce *et al.*, 2007). In fact Rubin *et al.* (1999) documented that faults which creep largely aseismically, simultaneously produce abundant microearthquakes, and the total slip represented by the earthquakes amounts to only a small fraction of the long term observed slip rate. Thus the ATF surface is supposed to be interested by aseismic creeping portions that may explain the long-term extensional rate and our analysis have been performed also to evaluate this possibility.

3.3   GPS data and Block Modeling setting

The tectonic deformation occurring across the Umbria-Marche Apennines have been also observed by GPS measurements (Hunstad *et al.*, 2003; Serpelloni *et al.*, 2005; D'Agostino *et al.*, 2009; Hreinsdóttir & Bennett, 2010; Bennett *et al.*, 2012) providing an extensional rate for the whole region of the order of 2-3 mm/yr in NE-SW direction. This estimate is rather higher than the geologic slip-rate associated to the ATF (Collettini, 2002) and it may suggest that this extensional deformation might be accommodated by more than one fault-system. The high-angle SW-dipping normal fault-system likely play an important role within this context, in which they are the principal sources of the moderate seismic events occurred in this region.

The kinematic approaches, described in Chapter 1, could give in this context interesting indications about which particular fault system may better reproduce the geodetic deformation rate, and thus accommodate the extension. In particular the Block Modeling (BM, section 1.4) allows to reproduce a GPS velocity field within an auto-consistent kinematic frame, by means of which we may evaluate the amount of deformation should be accommodated by each fault-system . Thus we have defined a block geometry consisting on 16 blocks related to Alps, Dinarides and Central Apennines, in order to consider a self-consistent kinematic scenario of the northern Apennines and Adriatic region. We have set the block-boundary positions and associated fault parameters (dip angle and locking depth, LD, i.e. seismogenic thickness of fault) using geological (DISS, 2010; Lavecchia *et al.*, 2002) information, taking into account also the available instrumental seismic catalogs (e.g. Pondrelli *et al.*, 2006).

From the complete GPS velocity field presented in section 2.2.2, we have selected almost 600 velocities (from continuous and survey-mode stations), located in the European region and the northern part of the Italian peninsula. Figure 3.2 shows the used block-
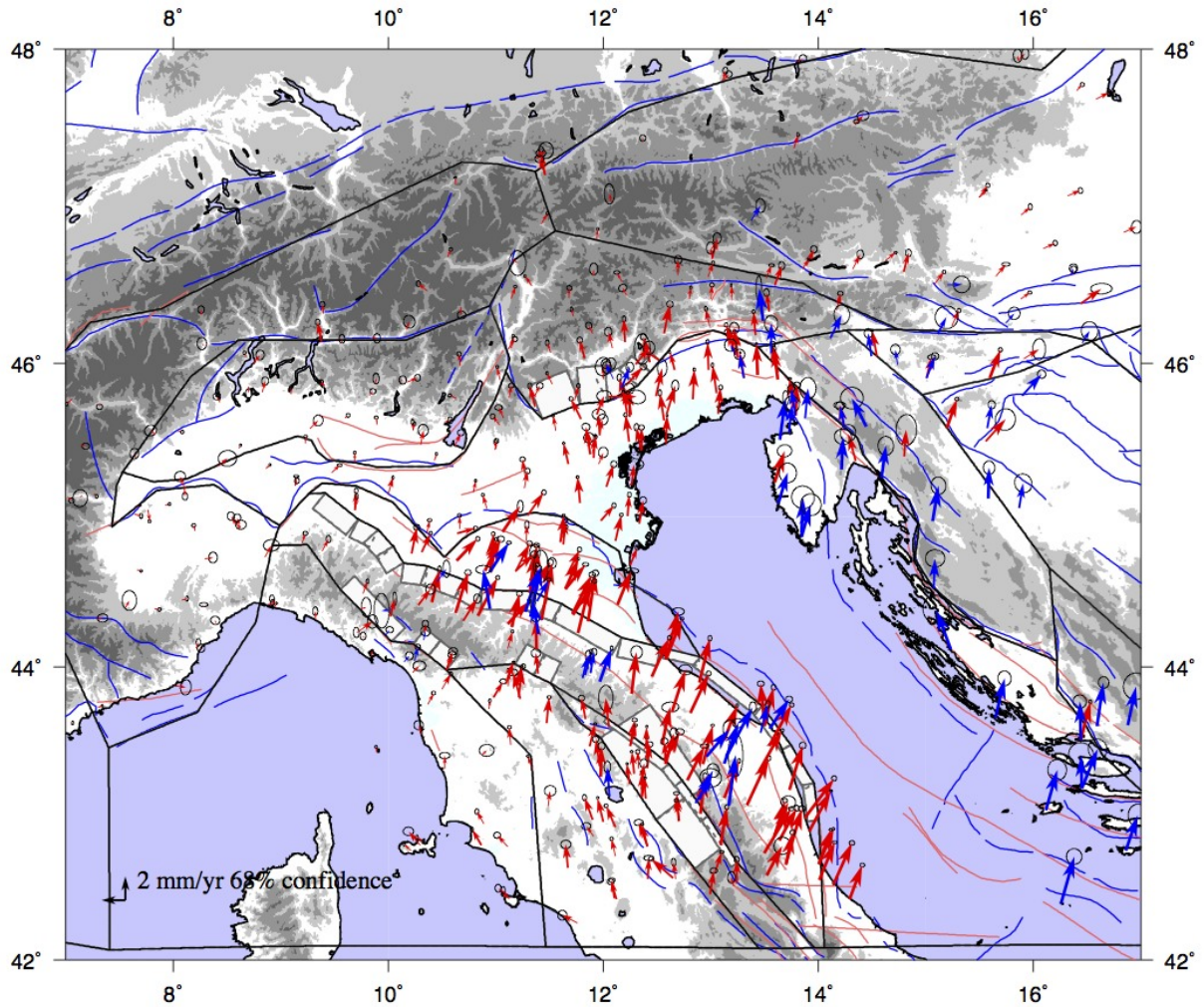
Figure 3.2: *Block geometry defined by black lines and white rectangles are the surface projection of dipping faults at boundaries. Red and blu arrows indicate the observed velocity field wrt Eurasia fixed frame from continuous and survey-mode sites, respectively.*

model geometry with dipping fault boundaries where provided for, and the selected GPS velocity field, observing as expected a NE-SW extensional rate of 2-3 mm/yr across the Umbria-Marche Apennines.

We have performed a kinematic analysis focused on active extension across the Umbria-Marche Apennines, considering the east-dipping LANFs and the high-angle west-dipping normal faults. In particular for the LANFs we define the ATF segment as a ∼70 km long, 15° east-dipping fault, with a locking depth of 12 km, as shown by relocated microseismicity of Chiaraluce *et al.* (2007) and the isobaths obtained by Mirabella *et al.* (2011), and the adjacent southern segment with a dip of 20° and LD = 10 km. Moreover we have defined most of the antithetic high-angle normal faults using the seismogenic boxes presented by Lavecchia *et al.* (2002), and in particular for the Gubbio fault (GuF) we

have considered a west-dipping plane of 40° with 6 km of locking depth, as a mean of the values proposed in the literature (Lavecchia *et al.*, 2002; Collettini *et al.*, 2003).

Thus using the block-geometry and the GPS velocity field just presented, we have tested firstly different BM scenarios to verify which of the fault boundaries proposed should actively accommodate the tectonic extensional rate measured by geodetic data. In particular we have considered three different cases, assuming as a fault boundary between the eastern and the western sides of the Apenninic chian (see Figure 3.3):

M1: just the east-dipping LANFs, i.e. the Alto Tiberina fault,

M2: just the antithetic west-dipping high-angle normal faults,

M3: both fault systems, i.e. M1+M2.

We have computed after each inversion the reduced chi squared of data and we have used the Fisher test (Stein & Gordon, 1984) to evaluate the acceptance between n and n+1 plate models, i.e. to asses if more complex models are justified by the data. Moreover for each solution we have estimated the long-term slip rates associated to the considered fault systems.

Table 3.1 reports the results of our tests evaluating the reduced chi squared χ_r^2 for the whole dataset (tot) and for a selected set of stations (sel) located close to the northern sector of Umbria-Marche Apennines, together with the corresponding slip-rates obtained in each inversion. As we can see there, the reduced chi-squared values are lower assuming the third geometry, for which also the F-test is positive. The corresponding fault slip-rates obtained from each inversion are representative of the attempt of inversions to reproduce the horizontal tectonic extension. In fact in the first two solutions we have obtained

Geometry/ Literature	Chi2rid (tot)	Chi2rid (sel)	ATF S.R. (mm/yr)	GuF S.R. (mm/yr)	Hor. S.R. (mm/yr)
M1	9.49	8.46	$2.4^{\pm0.1}$	-	$2.3^{\pm0.1}$
M2	9.51	7.89	-	$2.8^{\pm0.1}$	$2.1^{\pm0.1}$
M3	9.36	7.29	$1.5^{\pm0.1}$	$1.3^{\pm0.1}$	$2.4^{\pm0.1}$
Collettini (2002)	-	-	1.0	-	-
Collettini *et al.* (2003)	-	-	-	1.65 - 1.9	-
Mirabella *et al.* (2011)	-	-	-	-	3.0

Table 3.1: *Reduced chi-squared values computed for the whole GPS dataset (tot) and for a selected set of stations (sel) located close to the northern sector of Umbria-Marche Apennines, for each inversion, performed with different setting geometries M1, M2 and M3 (see text); the forth and fifth columns report inferred down-dip fault slip-rates from elastic block modeling and values proposed in literature, whereas in the last one is computed the corresponding horizontal slip-rate on extensional direction for BM solutions and the total horizontal extension-rate across the chain estimated by Mirabella* et al. *(2011)*
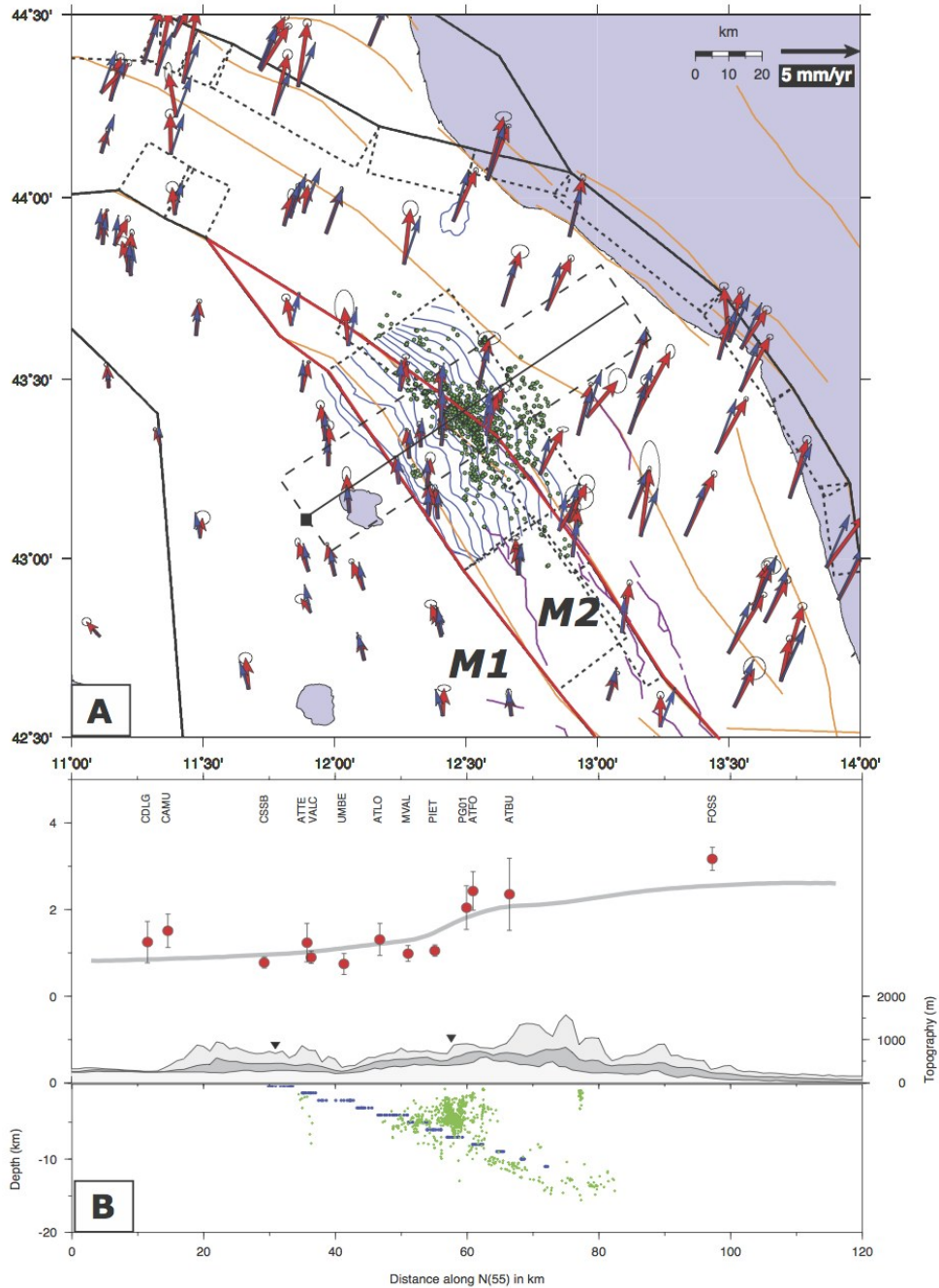
.

Figure 3.3: *Panel A: Sketch of different block-geometries used (M1, M2, M1+M2) to model the extensional rate; red arrows indicate the observed velocity field and the blu ones are the modeled velocities obtained with the M3 configuaration; green dots are the relocated microseismicity of Chiaraluce et al. (2007). Panel B: Parallel velocity components along the line profile indicated in Panel A of the observed velocity field (red dots with 1σ error bars) and the modeled one (gray line) due to the M3 configuration; black triangles indicate the surface fault trace position of ATF (left one) and GuF (right one); below are reported the minimum, mean and maximum values of the elevation topography, the microseismicity and the ATF depth points contours falling within the box profile.*

elevated fault slip-rates, which are higher than those proposed on literature (Collettini, 2002; Collettini *et al.*, 2003), except just for the one found by Hreinsdóttir & Bennett (2010), which, using GPS data too, is in agreement with the slip-rate of our first model. Using instead both fault systems as plate boundary within the Umbria-Marche Apennines we obtain lower down-dip slip-rates more in agreement with geological information (see Table 3.1), giving a total horizontal extension comparable with geodetic signal and slightly lower than the geologic estimation provided by Mirabella *et al.* (2011).

Thus our block-modeling analysis suggests that on the northern sector of the Umbria-Marche Apennines both the Alto Tiberina LANF and the antithetic, west-dipping, high-angle normal fault are likely accommodating the tectonic extension measured by GPS stations. Nevertheless looking the velocity cross section proposed in Figure 3.3B, we can observe two principal misfits.

The first one is the under-estimation of the GPS site (FOSS) that may be representative of some tectonic contribution not considered in our model. In particular we have performed a more complicated inversion solving for also the internal strain rate tensor (section 1.4, Eq.1.4-1.11) for blocks containing at least 30 GPS sites, to evaluate if this misfit may be explained by this further contribution. Unfortunately this test has provided just a slightly lower misfit for the whole GPS dataset, but any particular improvement for the GPS site at issue. Thus the misfit found for FOSS may be considered an elastic deformation signal not taken into account in our block-model setting and that needs a further specific study beyond the aim of this dissertation.

Instead the second misfit is observed for a group of GPS sites, located between the two fault systems, showing a systematic "flattening" of the parallel velocity component to the line profile that is not well reproduced by our block modeling. These velocities have been estimated from high-quality GPS sites (geophysical purpose, section 2.2.2), giving high reliability of thier recorded signal. In light of this, we have decided to estimate a distributed slip-deficit on the ATF, in order to evaluate which information GPS velocities may provide about the ATF coupling degree.

3.4   Interseismic coupling for the ATF surface

The approach used so far considers faults as uniform-slip rectangular planes, and to evaluate a non-uniform slip-deficit they should be subdivided in smaller elastic elements. In our case we have cosidered Triangular Dislocation Elements (TDEs), required by the code we use (section 1.4.2), which solve simultaneously for the rotational poles and the interseismic coupling distribution ϕ (section 1.4.1).

Initially we have considered a rectangular plane as representative of ATF with the same fault parameters used in the previous analysis (but LD = 13 km) and we have subdivided it with TDEs of ∼3km of size, using the free program DistMesh (Persson & Strang, 2004). During this analysis we have used both inversion techniques (section 1.4.3) for the coupling distribution estimate implemented in the BM code (Meade & Loveless, 2009), demonstrating the need of an alternative method to a Linear Least Square (LLS)
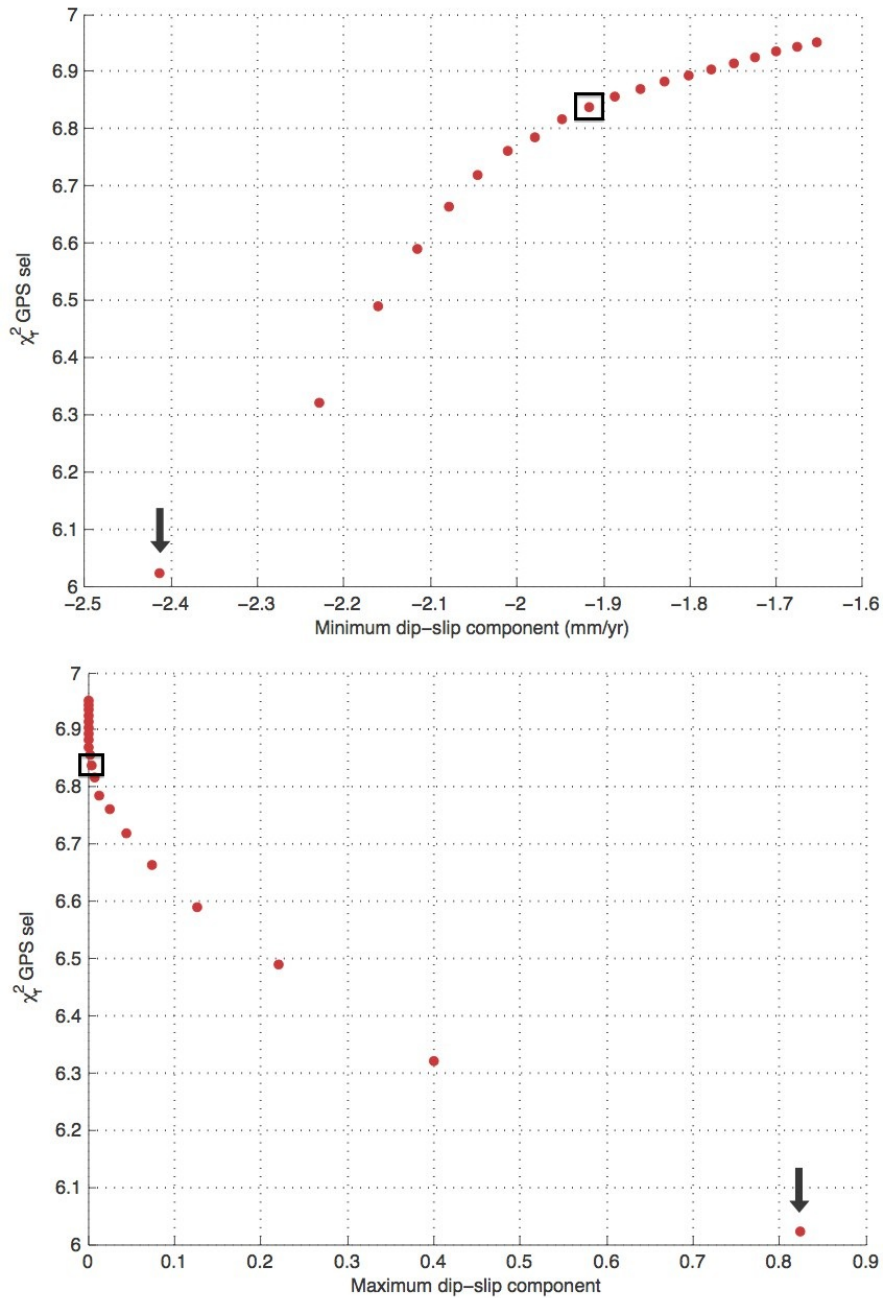
Figure 3.4: *Trade-off plots between maximum (below) and minimum (above) values of dip-slip component of back-slip distribution and the corresponding GPS residuals (χ^2_r) for a selected set of stations (sel) from BM inversions with the LLS solver for the interseismic coupling estimate as β changes among [50-1000] km^{-2} by step of 50; black arrows indicate the solution corresponding to the initial value $\beta = 50km^{-2}$ and black squares the optimal value chosen at $\beta = 500km^{-2}$.*

solver for a regularized problem. In fact in the original approach with a LLS technique to determine a slip-deficit distribution, the smoothing factor β (section 1.4.2, Eq. A.3) should not only regularize the roughness of slip distribution, but also modulate the magnitude of back-slip to be consistent with the kinematics of the considered region (Loveless & Meade, 2010). Whereas the alternative approach that we propose consists on a Linear Constrained Algorithm (LCA, Coleman & Verma, 2001) with which we can provide a-priori back-slip magnitude constraints, giving back to β its principal role of the weighting factor between minimizing the velocity misfit versus minimizing the roughness of the slip distribution (section 1.4.2, e.g. Harris & Segall, 1987). Moreover we have applied in all cases a further constraint to the slip-deficit distribution, forcing it to taper to zero at the bottom edge, at a depth of $\sim$13 km, roughly corresponding to the brittle-ductile transition expected for the region (Boncio *et al.*, 2004).

Then, after proving the advantages provided by the LCA method for the interseismic coupling estimate within the BM approach, we have considered the ATF as a 3D surface reproduced using the depth contours presented by Mirabella *et al.* (2011), in order to evaluate if an irregular fault surface may affect the final coupling distribution. This last configuration have provided interesting results, for which we have performed a last analysis of resolution test to assess the reliability of the available data to recover the coupling distribution found for the ATF surface.
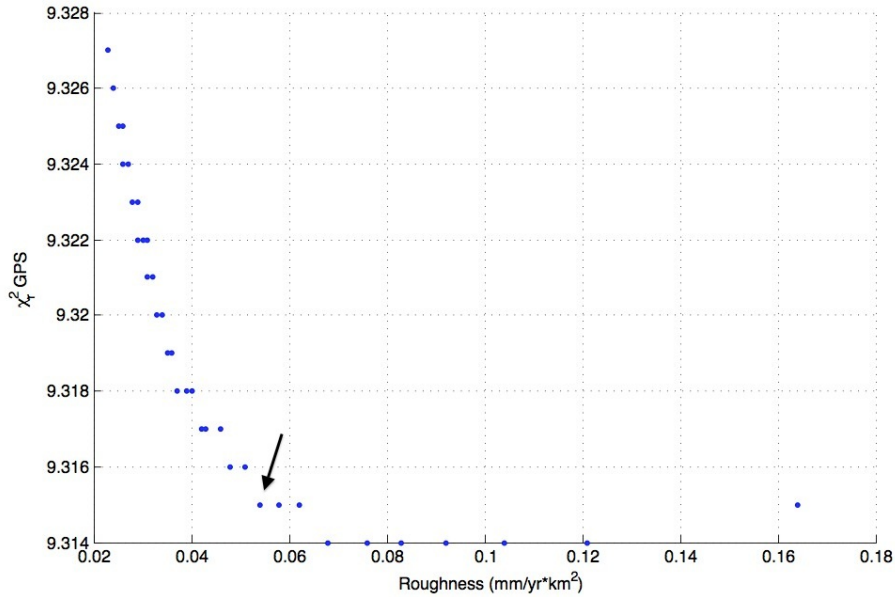

Figure 3.5: *Trade-off curve between GPS $\chi_r^2(tot)$ and the roughness of back-slip distribution obtained with the LCA inversion method, considering β changing from $0.05 km^{-2}$ (first point to the right) to $2 km^{-2}$ with step of $0.05 km^{-2}$; black arrow indicates the optimal solution corresponding to $\beta = 0.5 km^{-2}$.*

3.4.1   LLS vs LCA: comparison between coupling distributions

We have considered firstly the LLS "standard" inversion method for which, to choose the most suitable smoothing factor value for the coupling distribution, we have evaluated the minimum and maximum values of dip-slip components of the back-slip distribution as β changes. We consider the most appropriate smoothing factor that one for which the trend of maximum and minimum dip-slip components became stable close to long-term slip-rate value (Loveless & Meade, 2010).

 In this particular case we have considered β changing from 50 km^{-2} to 1000 km^{-2} with step of 50 km^{-2} and Figure 3.4 shows the minimum and maximum values of dip-slip component of back-slip distribution for each step. In this figure the black arrows indicate the solution obtained with the initial value $\beta = 50km^{-2}$ and then the other solutions are the following one by ones step by step. Thus we have chosen $\beta = 500km^{-2}$ for which the dip-slip components of back-slip solution have values among [-1.9,0] mm/yr, quite in agreement with the expected kinematics for the ATF. The corresponding coupling distribution is shown in Figure 3.6A with the observed and modeled velocities, and Figure 3.7A shows in detail the fit of parallel velocity components along the swath profile indicated in Figure 3.6, providing a $\chi_r^2(tot) = 9.43$ and $\chi_r^2(sel) = 6.84$.

Instead, using the LCA method inversion within the BM approach, we have constrained the slip-rate of each fault patch to be equal or greater (up to zero) than the long-term slip-rate estimated from the uniform-slip block model (i.e. -1.5 mm/yr, as reported in Table 3.1). Moreover we have defined the most appropriate smoothing factor β considering a typical trade-off curve between the residuals for GPS data ($\chi_r^2(tot)$) and the roughness of back-slip distribution (e.g. Harris & Segall, 1987; Árnadóttir & Segall, 1994). Thus from this trade-off curve, shown in Figure 3.5 we have chosen the optimal solution for $\beta = 0.5km^{-2}$, for which the smoothing action represented by the roughness quantity has regularized enough the coupling distribution with no expenses for GPS residuals. The corresponding coupling distribution is shown in Figure 3.6B with the observed and modeled velocities, and Figure 3.7B shows in detail the fit of parallel velocity components along the swath profile indicated in Figure 3.6, providing a $\chi_r^2(tot) = 9.315$ and $\chi_r^2(sel) = 5.24$.

Comparing the coupling distributions obtained with the two methods (Figure 3.6) we can see that with the LLS solver we obtain a solution much more smoothed with respect to the second one, where we may distinguish two principal asperities, just below the area characterized by a more dense GPS network. The common feature of two solutions is the shallow part of coupling distribution, having locked patches in the NW sector and partially/free coupling in the SE part of the surface. However the first method (LLS) has provided higher GPS residuals than those from the LCA solver solution and looking at velocity profiles shown in Figure 3.7, the second method allows us to obtain a solution able to reproduce better the "flattening" of the observed signal between the two fault systems.

Thus the change performed for the BM code about the inversion method has led a great improvement to obtain a more datailed coupling solution, also reproducing better the observed velocities. Therefore, we have continued our analysis using the second method for
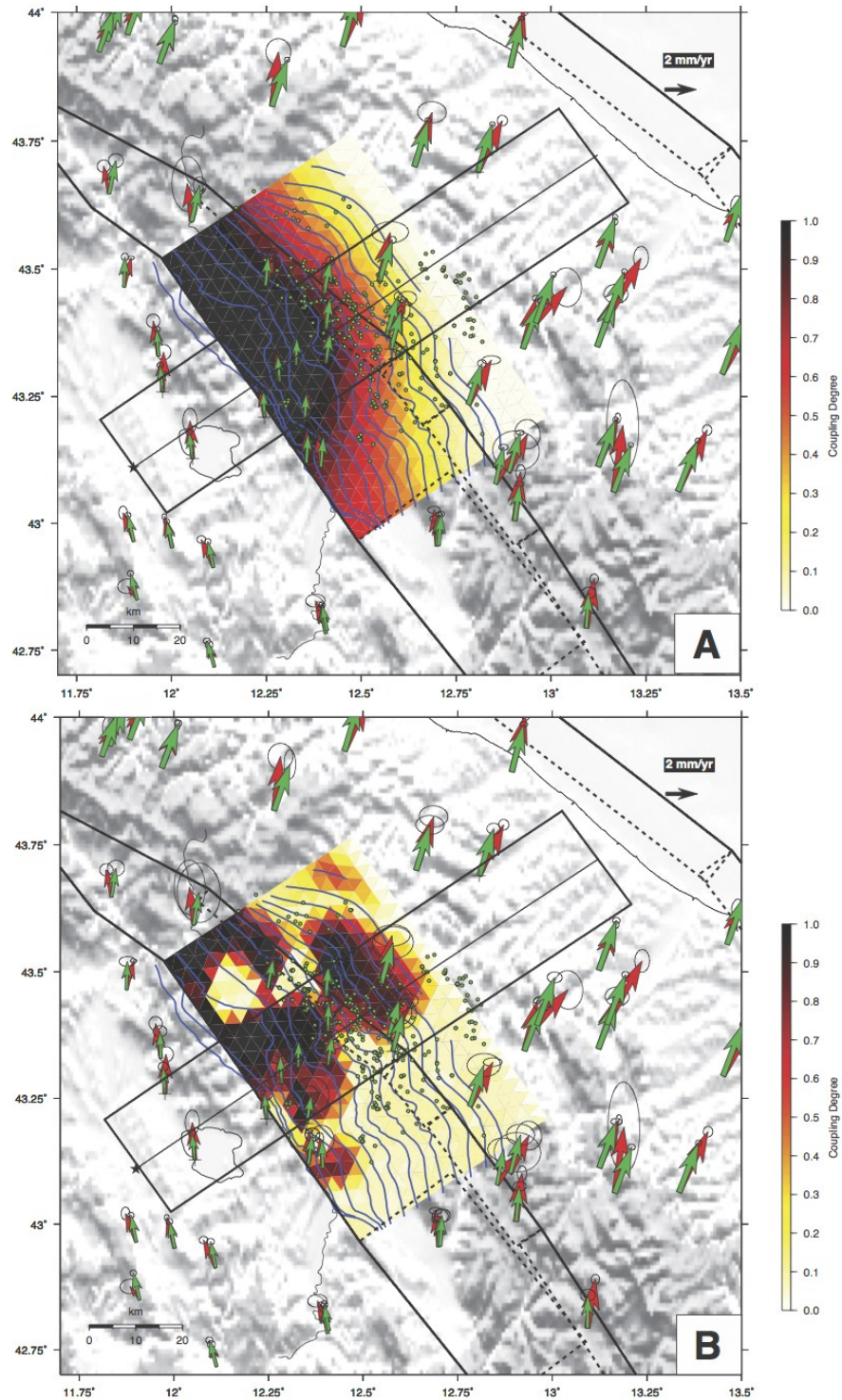
Figure 3.6: *Coupling distribution solutions obtained with the LLS (panel A) and LCA (panel B) inversion methods, where dark patches ($\phi = 1$) indicate full coupling and light ones ($\phi = 0$) corresponds to uncoupled portions; red and green arrows indicate observed and modeled horizontal velocities, respectively, and green dots show the microseismicity relocated by Chiaraluce et al. (2007) selected at 1.5 km of distance from the ATF surface (see Figure 3.7).*
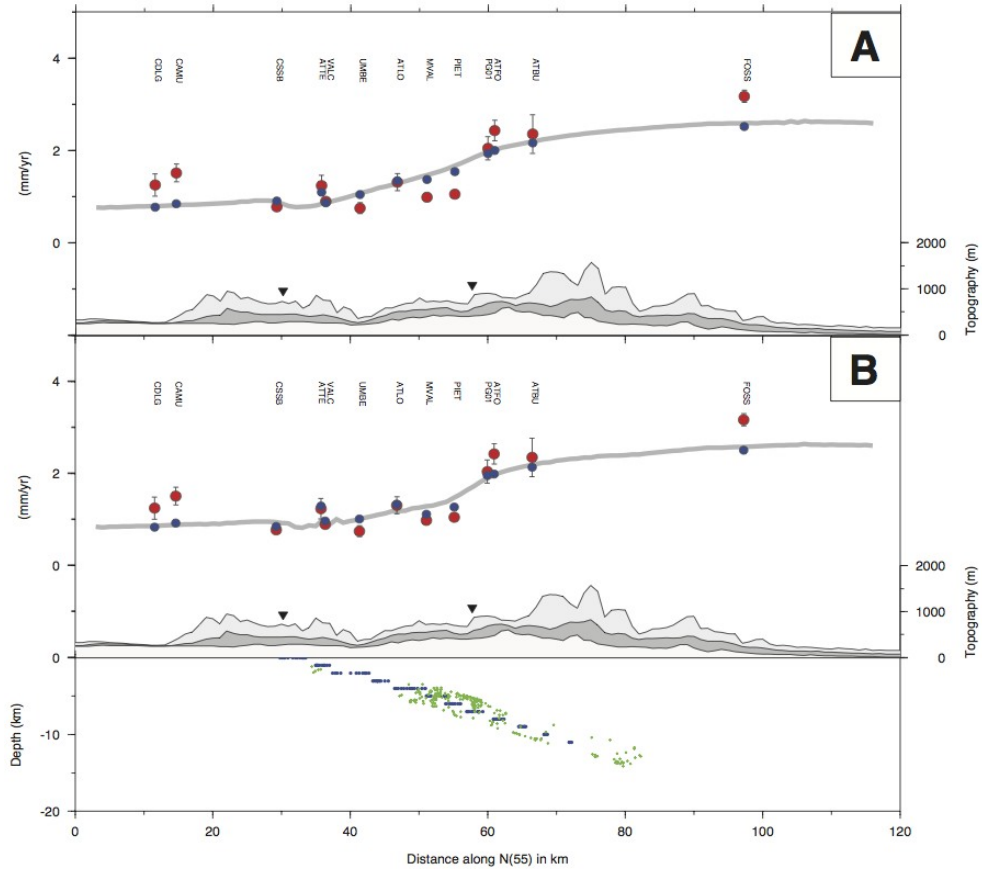
Figure 3.7: *Parallel velocity components along the line profile indicated in Figure 3.6 for observed (red dots) and modeled (blu dots) velocities obtained with the LLS (panel A) and LCA (panel B) inversion methods, and the gray lines are the mean values of the parallel components of estimated velocities for a point grid falling within the box profile indicated in Figure 3.6; below the profiles are reported the same characteristics shown in Figure 3.3, except for the microseimicity that have been selected at 1.5 km of distance from the ATF surface.*

which finally we have established its reliablity by means of several chekerboard resolution tests.

3.4.2   2D vs 3D ATF mesh surface

To explore further this topic, it may be interesting to consider the geometric irregularities highlighted by the ATF isobath map elaborated by Mirabella *et al.* (2011), shown by blu lines drawn every kilometer of depth in Figures 3.1, 3.3, 3.6, characterized by longitudinal bends and irregularities along-strike and along-dip. Using these depth contour lines we have generated a curved surface, meshed with triangular patches, using the GMSH software (Geuzaine & Remacle, 2009). A skecth of the meshed surface is shown in Figure
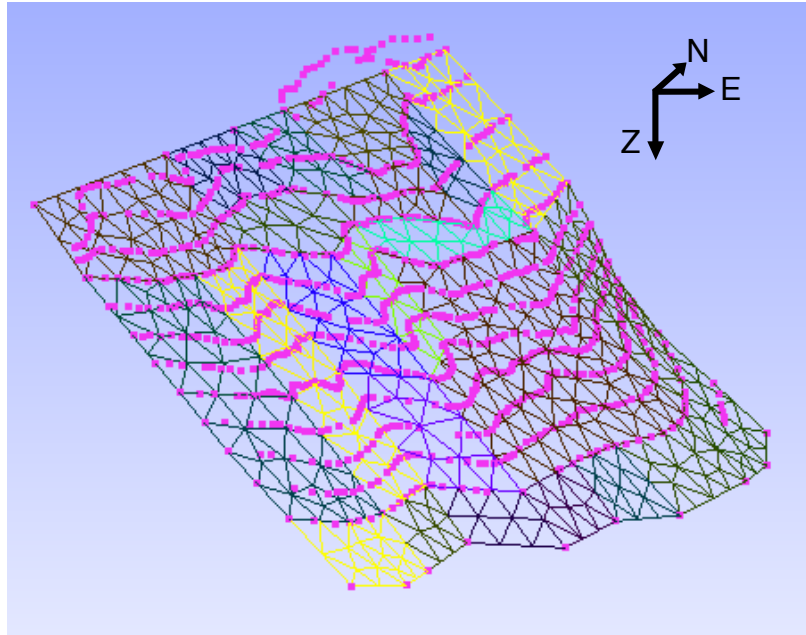
Figure 3.8: *Sketch of the 3D mesh surface for the ATF, considering the depth contours for each kilometer (pink dots) from the surface to 12 km, provided by Mirabella et al. (2011).*

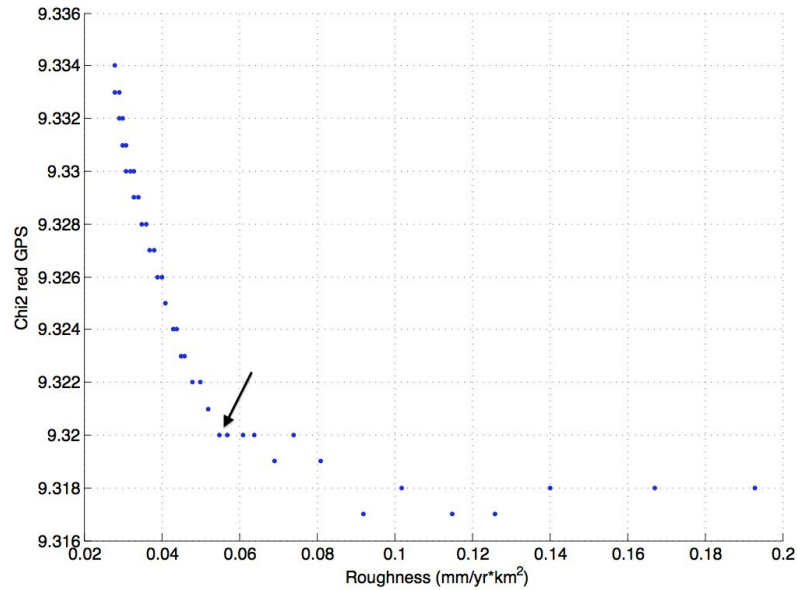**Figure 3.9:** *Trade-off curve between GPS $\chi^2_r(tot)$ and the roughness of back-slip distribution for the 3D ATF surface, obtained with the LCA inversion method, considering β changing from $0.05km^{-2}$ (first point from the right) to $2km^{-2}$ with step of $0.05km^{-2}$; black arrow indicates the optimal solution corresponding to $\beta = 0.7km^{-2}$.*
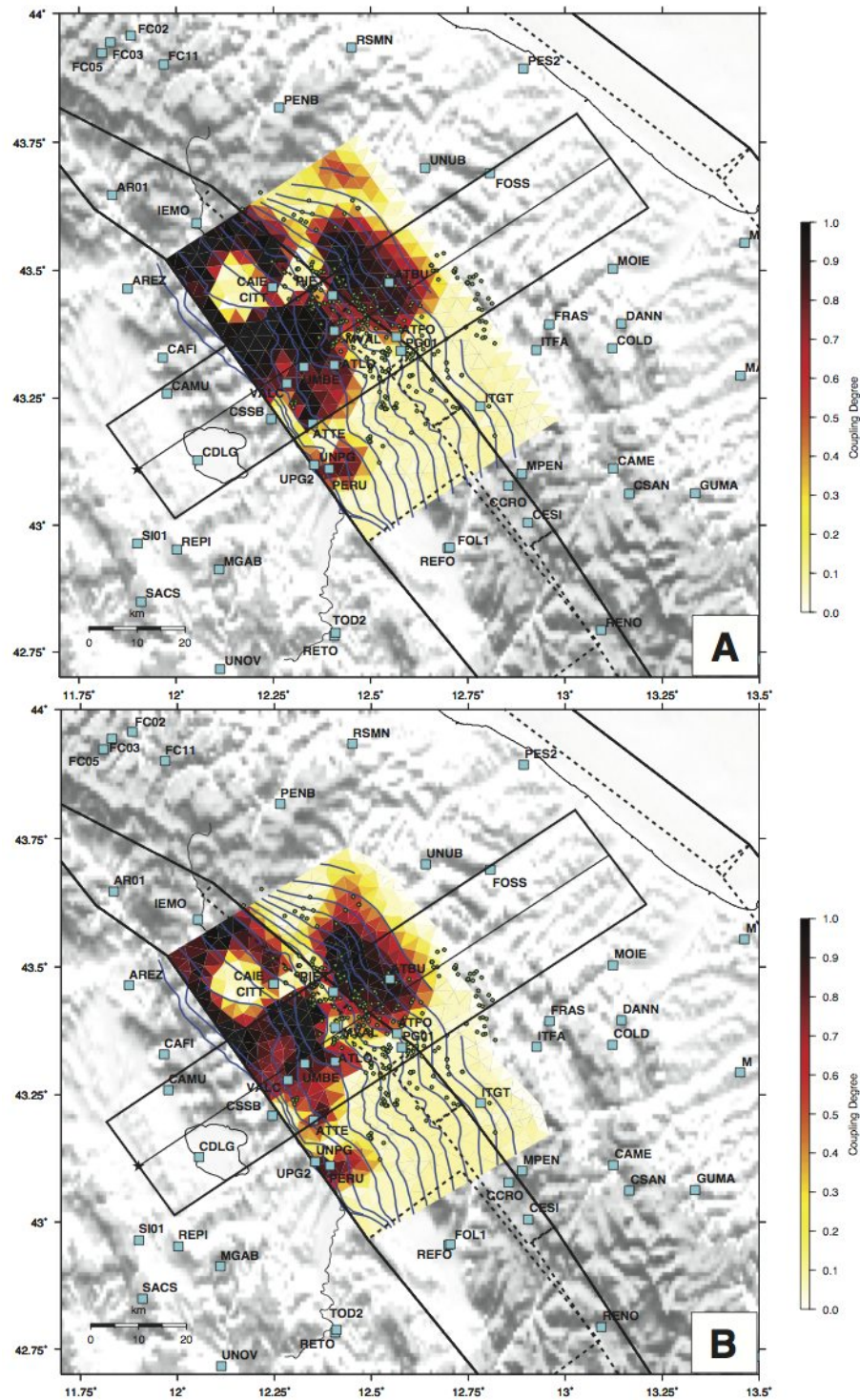
Figure 3.10: *Coupling distribution solutions obtained for a 2D plane geometry (panel A, same as Figure 3.6) and a 3D irregular one (panel B) for the ATF surface; light blu squares indicate GPS sites, each with its own ID; other features are the same as in Figure 3.6.*
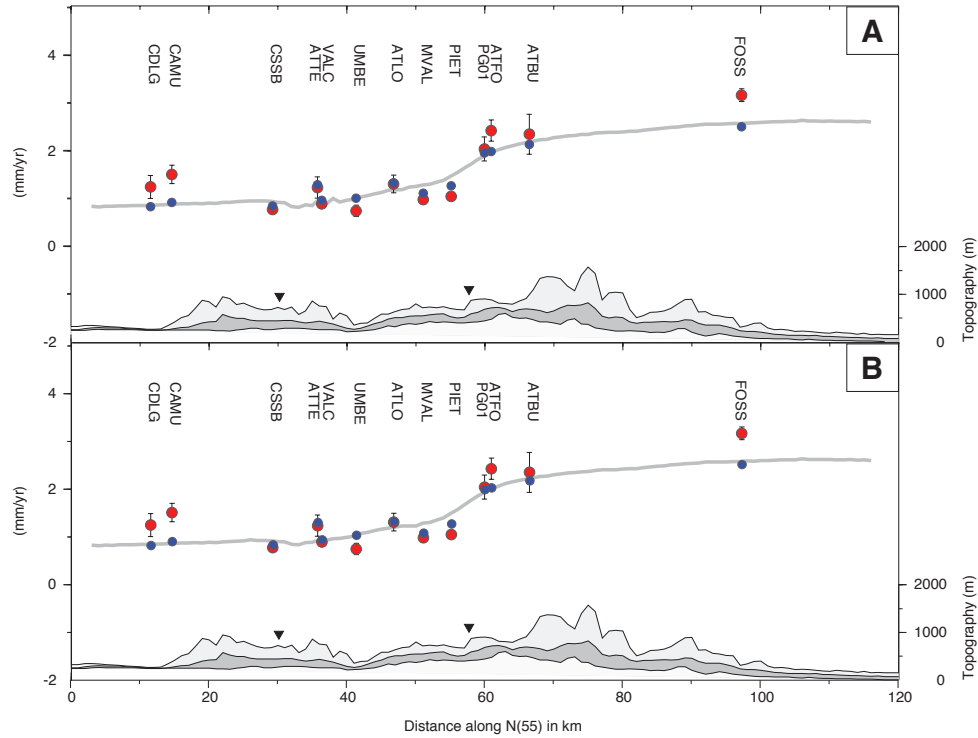
Figure 3.11: *Parallel velocity components along the line profile indicated in Figure 3.10 for observed (red dots) and modeled (blu dots) velocities obtained considering a 2D plane geometry (panel A) and 3D curved one (panel B) for the ATF surface during the BM inversion with the LCA method; other features represent the same characteristics indicated in Figure 3.7.*

3.8, for which we have approximated just the fault trace as linear segment and we have extended the surface up to 13 km of depth following the isobaths inclination point by point.

Then we have considered this 3D curved irregular surface to estimate the interseismic coupling distribution using the LCA method for the BM approach. As we have already performed for the rectangular surface, we have constrained the patch slip-rates between the same boundaries, and we have estimated the optimal smoothing factor evaluating also for this case a trade-off curve between the GPS residuals and the coupling distribution roughness (Figure 3.9). Thus, as for the rectangular meshed surface, we have chosen as optimal solution that one corresponding to $\beta = 0.7 km^{-2}$, beyond which the regularization action is overweighted at the expense of GPS residuals. The corresponding coupling distribution is shown in Figure 3.10B, where we have reproposed in the Panel A the coupling distribution for the rectangular plane surface to have a direct comparison between the two solutions. The coupling pattern are similar, except for the patches between the two major asperities, that in the 3D surface solution have become mainly uncoupled. This result is particularly interesting because the patches at issue are well correlated to the relocated microseismicity (Chiaraluce *et al.*, 2007) selected at just 1.5 km of distance from

the ATF surface, and their position corresponds exactly to the bottom edge of Gubbio fault. In spite of these few differences between the coupling distributions, the GPS residuals obtained with the 3D surface ($\chi_r^2(tot) = 9.32$ and $\chi_r^2(sel) = 5.26$) are basically the same as found for the 2D meshed plane, as also shown in the velocity profiles displayed in Figure 3.11. Thus we can explain this result suggesting that the coupling estimate can slightly change whether different surface geometries are used. On the other hand, the 3D surface coupling solution does not get worse GPS residuals, and furthermore it should be a more realistic representation than a plane for a well defined LANF as the ATF. Thus we consider the coupling solution for the irregular curved surface as the best estimate of the interseismic coupling degree for the ATF, considering data and the modeling approaches used so far.

3.4.3   Model resolution

We perform several resolution tests, adopting a checkerboard approach, in order to evaluate the reliability of our IC distribution and the ability of the available GPS network to recover the spatial asperity distribution. We have performed this kind of test with 12 different checkerboard coupling patterns, and we have created synthetic GPS velocity fields. Thus we have executed for each synthetic dataset systematic inversions considering different β values, in order to estimate the optimal recovered coupling pattern. The particular method defined for the choice of each specific solution has been explained in the Appendix B, which reports each original and recovered coupling pattern. This analysis has been performed in order to evaluate the reliability of the used LCA inversion method and the resolution ability of available GPS data to recover coupling patterns. Moreover, within a regularized problem the smoothing factor β plays an important role during the data inversion, allowing to detect the asperity distribution thanks to the regularization action, that may help to better model the observed velocities. Thus the β value depends strictly on the specific coupling pattern to estimate and it cannot be the same for all cases where the asperities have different positions and dimensions. This is due mainly by the basic under-determination of our problem, that can be solved only by an appropriate regularization controlled by β. For these reasons we have considered different β values during each checkerboard tests. The final resolution result has been interpreted as representative of the ability of GPS stations to resolve asperity patterns within a regularization approach that provides a support to the data for the coupling detection.

For twelve performed tests, we have chosen for each case the best coupling solution and we have defined for each one which TDEs are recovered or not (see Appendix B for details). Then we have computed for each TDE the percentage of recovery (i.e. resolution degree) in the total of all considered cases, and because of the low quantity of evaluated cases (that are not statistically significant), we consider the most reliable areas those ones characterized by at least 60-70% of resolution.

Figure 3.12 shows the final resolution degree obtained by this analysis and also the coupling contour lines for the principal asperities. Observing these two features we can consider resolved just the southern portion of the shallowest asperity, and comparing the

resolution distribution with the GPS station positions, it's evident a considerable correlation among resolved areas and GPS sites. Moreover the resolution degree associated to the patches located between the two main asperities is quite good, inferring that the corresponding uncoupled portion should be well resolved by our data.
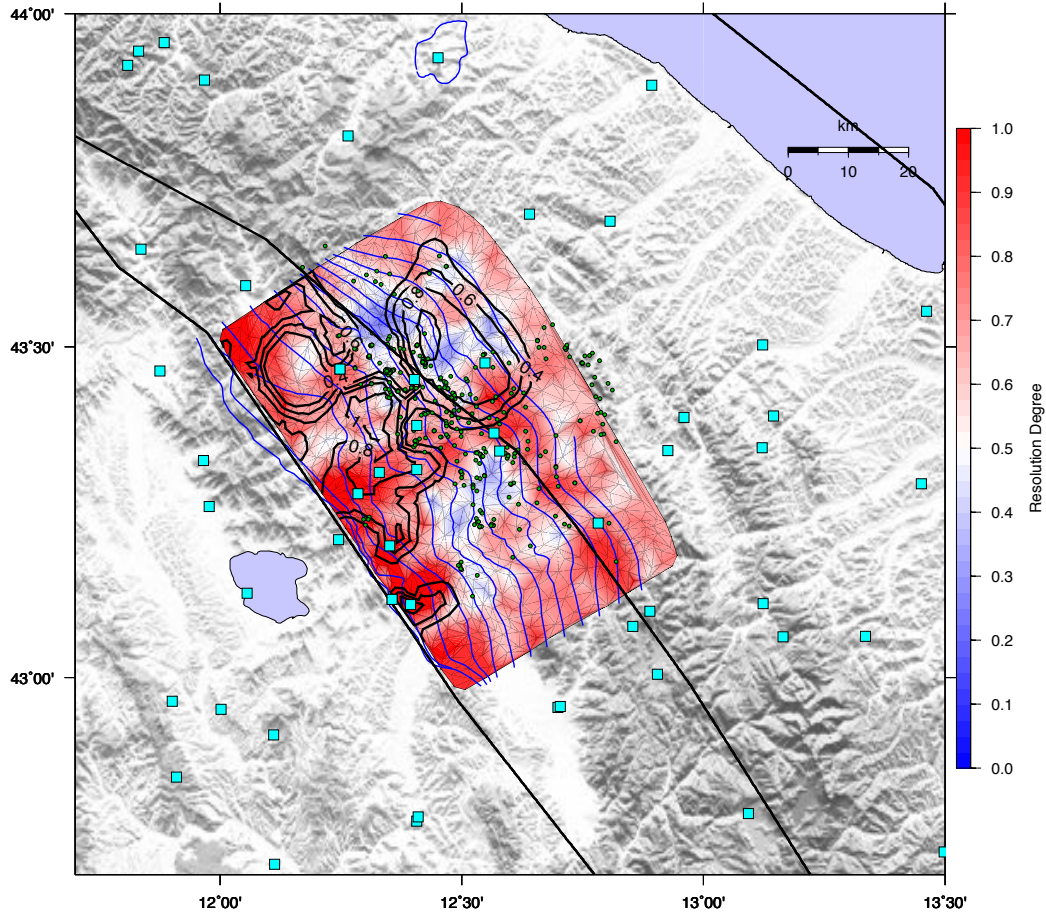

Figure 3.12: *Final resolution degree of coupling distribution interpolated among the TDE with the coupling contour lines starting from 0.4 to 1 with steps of 0.2; light blu squares indicate GPS station positions. Considering resolved areas those ones with percentage resolution greater than 0.7, we can observe a good correlation among GPS sites and more resolved patches.*

3.5   Discussions

Using a self-consistent kinematic block modeling we have studied the northern sector of the Umbria-Marche Apennines, where several GPS stations show SW-NE oriented extensional deformation. We have tested different block model geometries to reproduce the geodetic extensional rate, in order to understand which fault system is accommodating

the tectonic extension. We found that the GPS velocity field is better reproduced by a block model geometry considering both the Alto Tiberina LANF and the antithetic high-angle Gubbio normal fault (GuF) as active fault systems within this apenninic extensional sector. Moreover this configuration provides also long-term slip rates for the ATF and the GuF kinematically in agreement with the geological ones (Collettini, 2002; Collettini *et al.*, 2003). However we do not exclude the possibility that further active fault systems may contribute to the whole extensional deformation. In fact we have obtained a slight under-estimation for some GPS sites (in particular FOSS) in the eastern sector of the chain, and in addition the horizontal extensional rate expected from the long-term slip-rates obtained for the ATF and GuF in this configuration (see Table 3.1) is lower than the whole active extension estimated by Mirabella *et al.* (2011).

From our block-model geometry we obtain also systematic residuals for a group of GPS sites located between the two fault systems, and we have inferred that this misfit may be due to a variable interseismic coupling degree distribution on the ATF surface. Thus, approximating the ATF surface as a rectangular fault plane subdivided in TDEs, we have inverted GPS data solving for the back-slip distribution, using two different inversion methods. If the original BM code applies an inversion method (LLS), we have also used an alternative solver (LCA) which allows to constrain the magnitude of the back-slip distribution, providing an a-priori defined interval within which the slip may vary. From the coupling results and residuals obtained from each different method, we observe that the second one is more powerful than the original solver, providing lower residuals and more defined coupling distributions. This positive result has allowed us to use the LCA method in the subsequent coupling analysis.

Parameterizing instead the ATF as a more realistic, curved surface and performing the BM inversion of GPS data using the LCA method, we do not observe any particular improvement for the GPS residuals. However, a 3D surface should be a more realistic representation for a well defined LANF as the ATF, and since GPS residuals are comparable, we have considered the coupling distribution of the more complicated geometry as the final optimal solution obtained for the ATF by means of a BM approach. The final coupling distribution is characterized by two principal asperities located in the north-western part of the surface, one shallow between 2-4km of depth and the other one deeper from 7-10km of depth, whereas the other surface portions are interested by creeping behavior. Testing this final coupling distribution by means of several checkerboard tests, we demonstrate that the most reliable coupling portions are those located just below GPS sites. For what concerns the coupled areas we have resolved the south-eastern part of the bigger shallowest asperity and a shallow smaller one in the south. In fact they are located just below the GPS sites VALC, UMBE, ATLO and ATTE, for the bigger asperity, and UNPG and PERU for the smaller one (Figure (3.10). Estimating approximately the seismic potential of these two resolved asperities, we obtain a moment magnitude Mw greater than 6.5 and 6 for the big and the small ones respectively. However in this area no strong historical earthquakes have been recorded since 461 bc (Boschi *et al.*, 1999).

Moreover also some creeping areas are resolved as well by the presence of close GPS site,

also for the uncoupled patches between the two main asperities. These patches in the planar surface coupling solution were not intersted by creep, whereas considering for them a more realistic geometry, they became uncoupled do not providing any changes in the GPS residuals. This means that the available data do not justify an elastic contribution generated by the more dipping geometry of those patches, and this is possibly influenced by two GPS stations located exactly above the patches at issue (MVAL and PIET, Figure 3.10). Because also the good resolution degree obtained for those patches, we can assess that their low coupling degree may be a real occurring feature for that ATF surface portion.

Furthermore our final coupling distribution is quite in agreement (except for the unresolved deep asperity) with the result presented by Hreinsdóttir & Bennett (2010), proposing a shallow locking depth for the ATF and aseismic creep below. In addition it is worth to note an interesting correlation between the relocated microseismicity of Chiaraluce *et al.* (2007) selected within ±1.5 km of distance from the ATF surface and the creeping portions of the fault surface, in particular for the uncoupled patches found at 4-6 km of depth. This interesting characteristics may provide more reliability to our coupling solution, since microseismicity is attributed usually to aseismic creeping behavior (Rubin *et al.*, 1999; Vergne *et al.*, 2001). Many works have already suggested an aseismic detachment of the ATF (Collettini, 2002; Lavecchia *et al.*, 2002; Chiaraluce *et al.*, 2007; Hreinsdóttir & Bennett, 2010), and this hypothesis is also assessed by the presence of high fluid overpressures (Collettini, 2002), that may trigger the nucleation of microseismicity (Chiodini *et al.*, 2004; Antonioli *et al.*, 2005). This fault behavior associated to LANFs has been observed by Collettini & Holdsworth (2004) from surface geology data of the Zuccale LANF, no more active fault exhumed to the west of ATF, indicating the aseismic creeping as principal fault mechanism, interspersed with small seismic rupture events caused by short-lived cyclic build-ups in fluid overpressure. Thus also our result of coupling distribution has provided a further contribution to assess the creeping behavior in depth of the ATF. However the correlation found has been verified with seismic events recorded during 8 months of surveying (Piccinini *et al.*, 2003) and it might be of interest to evaluate this correlation with future available data.

Chapter 4

Estimation of fault boudaries and interseismic coupling from joint inversion of GPS and InSAR data on Gargano area

4.1 Introduction

The deformation of the Gargano promontory is traditionally interpreted as due to a shear zone that has had origin with the different subduction and retreating rates the whole Adratic slab beneath the Apennines fold-and-thrust belt underwent, due to differences in thickness of the Adraitic plate (Doglioni *et al.*, 1994; Billi *et al.*, 2007; Ridente *et al.*, 2008; Spalluto & Pieri, 2008). This tectonic activity has produced in the Gargano area many fault systems (Brankman & Aydin, 2004) among which the most morphologically evident is the Mattinata fault. Currently it is not yet clear which fault systems are still active to accommodate the relative motion between the southern and northern parts of Adria plate, that is recently observed by GPS measurements (D'Agostino *et al.*, 2008; Devoti *et al.*, 2008). In fact this area was struck by several strong historical earthquakes(CPTI, Rovida *et al.*, 2011) and it is interested by a diffuse instrumental seismicity (Milano *et al.*, 2005; Del Gaudio *et al.*, 2007) that does not provide however any information about some specific fault-system.

In this particular contest we have figured out that a kinematic modeling might provide some further constraints on how this relative motion may be accommodated. Indeed thanks to the availability of a dense dataset of InSAR velocities (see section 2.3.4) concerning exactly the promontory, besides the GPS observations, it may be possible to detect some particular crustal deformation that can provide information on where and how it occurs. The integration of two different datasets needs, before any modeling approach, velocities to be referred to the same reference frame. For this reason we have estimated a planar signal (ramp) for the InSAR data that allows not only to have InSAR measurements comparable with GPS observations but also to correct InSAR data for some errors

not evaluated during InSAR processing (see section 2.4).

We have used jointly GPS and InSAR data (Chap. 2) in the kinematic models described in Chap. 1 following the integration of approaches as described on section 1.5. In particular we have used the Burial Dislocation method (section 1.3) to evaluate position and locking depth of a fault system accommodating the geodetic gradient. Then we have considered these informations in a Block Modeling approach (section 1.4) to estimate the interseismic coupling distribution for the identified fault structure within a self-consistent kinematically contest. This estimation will be performed with both inversion techniques implemented in the BM approach (section 1.4.3) in order to verify limits and improvements obtain with the modified BM method. At the end, we have evaluated the data ability to resolve the final coupling distribution by means of several checkerboard test.

4.2 Seismo-tectonic contest

The Gargano Promontory is located along the eastern coast of southern Italy, extending eastward into the Adriatic Sea away from the otherwise northwest-trending Italian coastline. The Gargano is a structural block within the Adriatic platform, a tectonostratigraphic domain of carbonate layers that forms the foreland and footwall units of the E-verging Apennines and the W-verging Dinarides fold-and-thrust belts (Salvini *et al.*, 1999). The Adriatic foreland runs to the NE of the Apennines from the Po Plain to Apulia and corresponds mainly to the Adriatic Sea. However the definition of its southern margin is still a debated question. The earlier works that used GPS measurements to determine the rotational kinematics of the Italian peninsula (Ward, 1994; Calais *et al.*, 2002; Battaglia *et al.*, 2004; Serpelloni *et al.*, 2005) have assessed that the Adriatic plate should move independently with respect to the Nubia plate and it could comprise also the Apulian platform. Nevertheless some of those works have proposed also a separation between the northern and the southern Adriatic region along a tectonic structure also known as the Gargano-Dubrovnik line (Oldow *et al.*, 2002) on the basis of the distributed seismicity which characterizes the central Adriatic (Console *et al.*, 1993; Favali *et al.*, 1993), but the distribution of the stations of the time wasn't able to show any significant relative motion. Then the more recent work of D'Agostino *et al.* (2008) has shown that a more updated GPS velocity filed is compatible with two distinct microplates in the Adriatic region, showing an active deformation occurring in the central Adriatic, which includes the Gargano promontory. A specific fault boundary between the two microplates has not defined yet, for which instead has been supposed a widespread deformation diffused over at least 200 km in the north direction and not concentrated on a single tectonic element, such as the proposed Gargano-Dubrovnik line (D'Agostino *et al.*, 2008). However the Gargano is interested by this diffuse deformation and considering the lackness of any geodetic measurements offshore, we have tried to evaluate the occurring deformation there.

This area is characterized by several geological and geophysical features distinguishing it from the rest of the Apulian foreland: the high relief with a maximum altitude of 1000
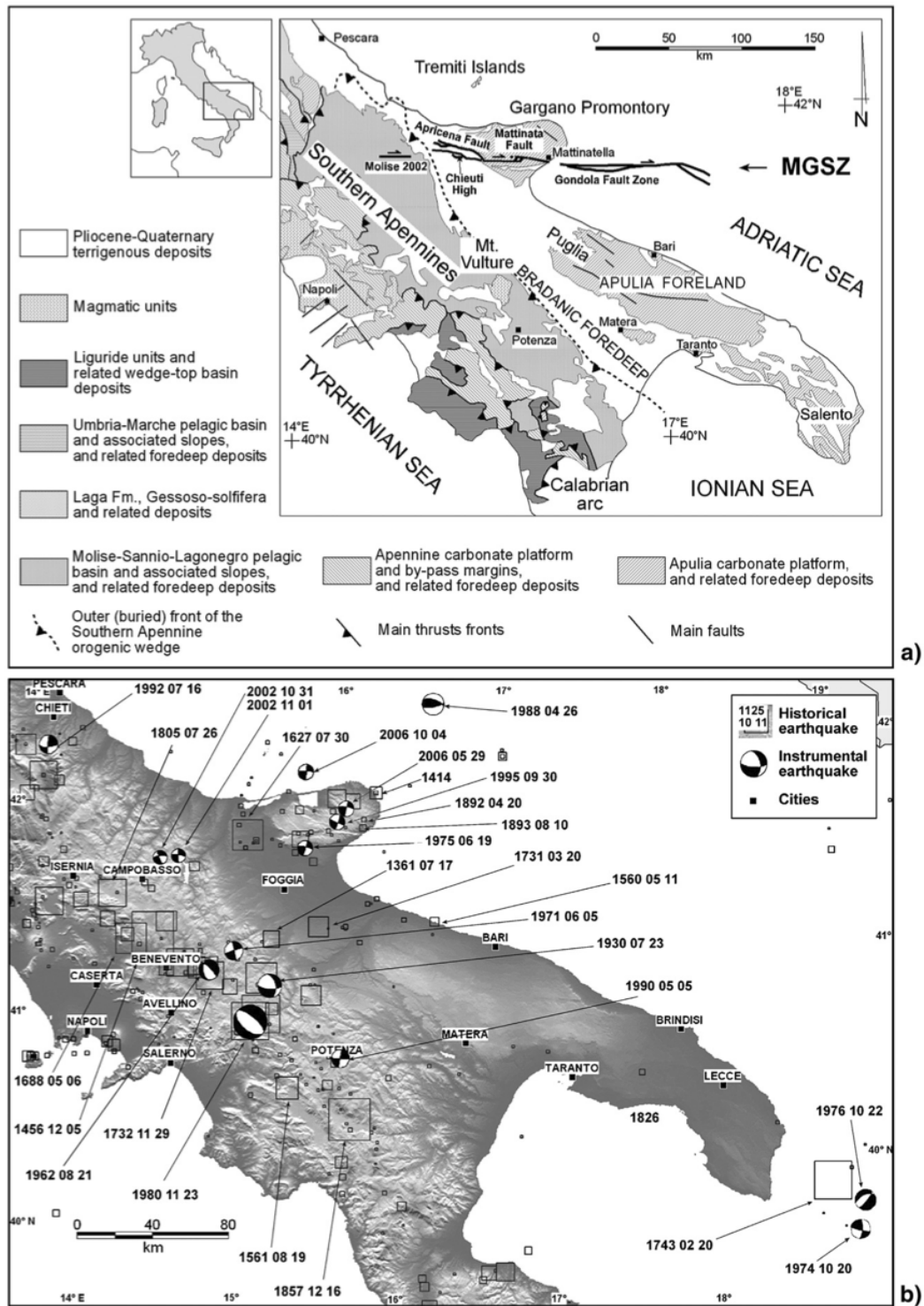
Figure 4.1: *From Ridente et al. (2008): a) Geological sketch map of Southern Italy (Calabrian arc excluded), showing the MattinataGondola Shear Zone (MGSZ). b) Historical and instrumental earthquakes of the Central and Southern Apennines (M>4.0; Gruppo di lavoro CPTI, 2004; Vannucci & Gasperini, 2004). The size of the square symbols is proportional to an equivalent magnitude derived from intensity data.*

m a.s.l., with respect to the maximum elevations of 200-300 m in the adjoining areas; the inland and offshore seismicity (Console *et al.*, 1993; Milano *et al.*, 2005); the presence of gravimetric and magnetic positive anomalies (Finetti *et al.*, 1987); a heat flow higher (60 mW/m^2) than the southern Apulian region (40 mW/m^2) (Mongelli & Ricchetti, 1970) and a crustal thickness smaller (25 km) than the average thickness estimated for the Apulian region (35-40 km) (Suhadolc *et al.*, 1990; Favali *et al.*, 1993).

Moreover the Gargano is signed by the presence of a widespread and complicated fault systems (Brankman & Aydin, 2004) mainly NW-SE, E-W trending, where the more visible morphological feature is the Mattinata fault system (see Fig.4.1a) that is ∼50 km long, E-Wtrending, cutting across the southern part of the promontory. This fault has received much attention by researchers, who, however, have so far provided contradictory interpretations on its kinematics and tectonic history. In summary, the Mattinata fault has been interpreted as reverse (Bertotti *et al.*, 1999), right-lateral (Piccardi, 2005), left-lateral (Salvini *et al.*, 1999; Brankman & Aydin, 2004; Billi *et al.*, 2007), right-to-left lateral inverted (De Alteriis, 1995), or left-to-right lateral inverted (Tondi *et al.*, 2005). The multi-kinematics assigned to this fault system is due to its riactivations in different tectonic regimes. Nevertheless, most investigators agree on a present-day right-lateral main component of motion, as confirmed also by the focal mechanisms (Vannucci & Gasperini, 2004; Del Gaudio *et al.*, 2007). Moreover geologic (Piccardi, 1998) and structural (Tondi *et al.*, 2005) analysis performed for the Mattinata fault supported the right-lateral motion of the fault, evaluating long-term slip rates within the interval 0.7-1 mm/yr. Furthermore on the basis of analog modeling, Di Bucci *et al.* (2006) reproduces the most recent phase of the Mattinata fault activity with a slip-rate of 1.3 mm/yr.

Indeed the Gargano promontory is charcterized by a diffuse instrumental seismicity and several historical strong seismic events (CPTI, Rovida *et al.*, 2011). Focal mechanisms (Vannucci & Gasperini, 2004; Pondrelli *et al.*, 2006; Del Gaudio *et al.*, 2007) show slip movements of faults mainly with right-lateral, tranpressional and compressional kinematics. However the seismicity in the region is of limited use in defining the trend of tectonic structures, since the recorded events does not concentrate around some particular fault (Del Gaudio *et al.*, 2007). In particular Milano *et al.* (2005) showed that the Gargano seismicity is generated by E-W, right-lateral strike-slip faults belonging to the Mattinata-Gondola fault-system, and by NW-SE, normal to left-lateral second-order faults slipping in response to dominantly NW-SE shortening. Moreover observations from the main historical earthquakes (e.g., San Severo 1627, and M. Sant'Angelo 1893, see Fig.4.1b) also suffer of large uncertainties (Del Gaudio *et al.*, 2007). For instance, the Mattinata fault has been invoked to account for the 1627 San Severo event (macroseismic magnitude of 6.7 assigned by Rovida *et al.* (CPTI, 2011)), together with the other principal historical earthquakes in the region (Valensise *et al.*, 2004). However, the location of the fault responsible for the 1627 San Severo earthquake is highly debated, and the WNW-ESE Apricena fault (see Fig.4.1a) has been recently considered the most likely candidate on the basis of a detailed subsurface study (Patacca & Scandone, 2004).

However the indetermination of seismic potential of these fault systems on the Gargano promontory can be addressed using geodetic measurements to detect any active tectonic

deformation due to specific fault structures.

4.3   GPS and InSAR data

The geodetic data that we used to study the kinematics in the Gargano promontory consist on an accurate selection of available measurements obtained with the GPS and DInSAR techniques (Chap.2) in order to perform a very specific study focused on this region. Figure 4.2 shows the InSAR data in East-West direction overlapped with GPS velocities that, thanks to the presence of survey-mode stations (blu arrows), give a fairly coverage of the target area, even if in the southern part there's still a poor presence of GPS sites. We choose to consider the East-West InSAR velocity field since the block modeling approach works only with horizontal data (see section 1.4.2). As already introduced in section 2.4,
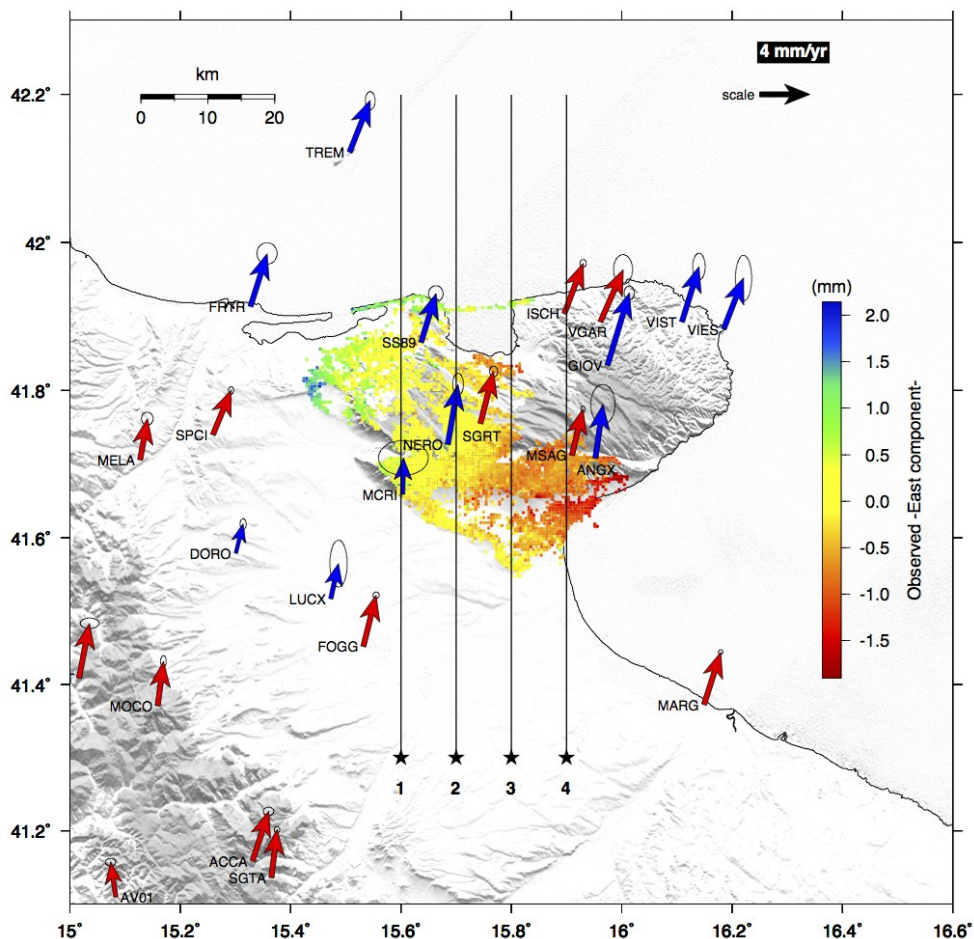

Figure 4.2: *GPS velocities w.r.t. Eurasia fixed frame and InSAR data in E-W direction referred to a local pixel close to the SGRT site; red arrows correspond to continuous GPS sites and blu ones correspond to survey-mode stations.*

the joint use of both kind of measurements needs to have measurements anchored to the same refence frame. In fact the InSAR velocities available for the Gargano promontory (see section 2.3.4) are provided in reference to a local pixel of the dataset, whereas GPS data are referred to an Eurasia well-defined reference frame (see section 2.2.2). In fact, it can be seen in Figure 4.3 from the profiles along the lines indicated in Figure 4.2, the E-W components of GPS and InSAR velocities show a mismatch that does not consists in a constant shift for all the points. This means that this gap cannot be corrected with a constant offset concerning with the different refence frame, but we should consider also a spatial variation of this mismatch, likely due to some non-corrected errors during the InSAR processing (section 2.3.4, Eq. 2.1).

4.3.1   Ramp estimation

As explained in section 2.4, a method widely used (e.g. Bürgmann *et al.*, 2000; Johanson *et al.*, 2006; Ryder *et al.*, 2007) to solve for this problem consists in estimating a planar ramp, represented by three parameters related linearly to the data (see Eq.2.1). To estimate these three unknowns and afterwards remove the ramp signal from InSAR data we need at least three GPS stations for which the Eq.2.1 should be valid, that is GPS sites lying within the InSAR frame. Looking at Figure 4.2, there are several GPS points falling in the area covered by InSAR velocities, but we cannot consider all of them, because some of them have big uncertainties (ANGX, MCRI). Moreover we decide to use the maximum number of GPS sites in order to avoid to loose information. Thus having four GPS stations (MSAG, NERO, SGRT, SS89) suitable for this purpose, the most appropriate method to estimate the ramp parameters is a Linear Least Square (LLS) inversion. for the Eq.2.1. However the most problematic issue of this approach concerns with the definition of the right velocity value for InSAR data to be compared with the E-W component of GPS velocities. In fact if we consider simply the velocity value corresponding to the closest pixel to the GPS sites, it may be troublesome if outliers are selected. Moreover we do not have any idea of which neighborhood of GPS points may be better to use,in order to have a right estimation of the ramp parameters.

That being so, we have decided to consider, for different distance radius, R, from GPS sites, the mean and the median values of velocities of pixels falling in the neighborhood. The considered interval of R spans from 0.5 km to 5 km with steps of 0.1 km. For each step we have performed the LLS inversion and we have evaluated the goodness of the corresponding solution estimating the RMS between GPS velocities and InSAR representative values corrected by the resulting ramp slope. The pattern of the RMS with the change in the radius is shown on Figure 4.4 and blu and green points correspond to solutions with mean and median InSAR velocity values, respectively. Their pattern are pretty similar but as the radius grows the approach with the median estimate gives relatively lower RMS. If we consider the RMS estimates (Figure 4.4), we can see that these values are already low (order of 0.1 mm/yr) for small radius, but if we observe instead the cross section profiles for the resultant E-W InSAR velocities shown by Figure 4.5, we may suppose that for small radius the ramp correction is not appropriate. In fact
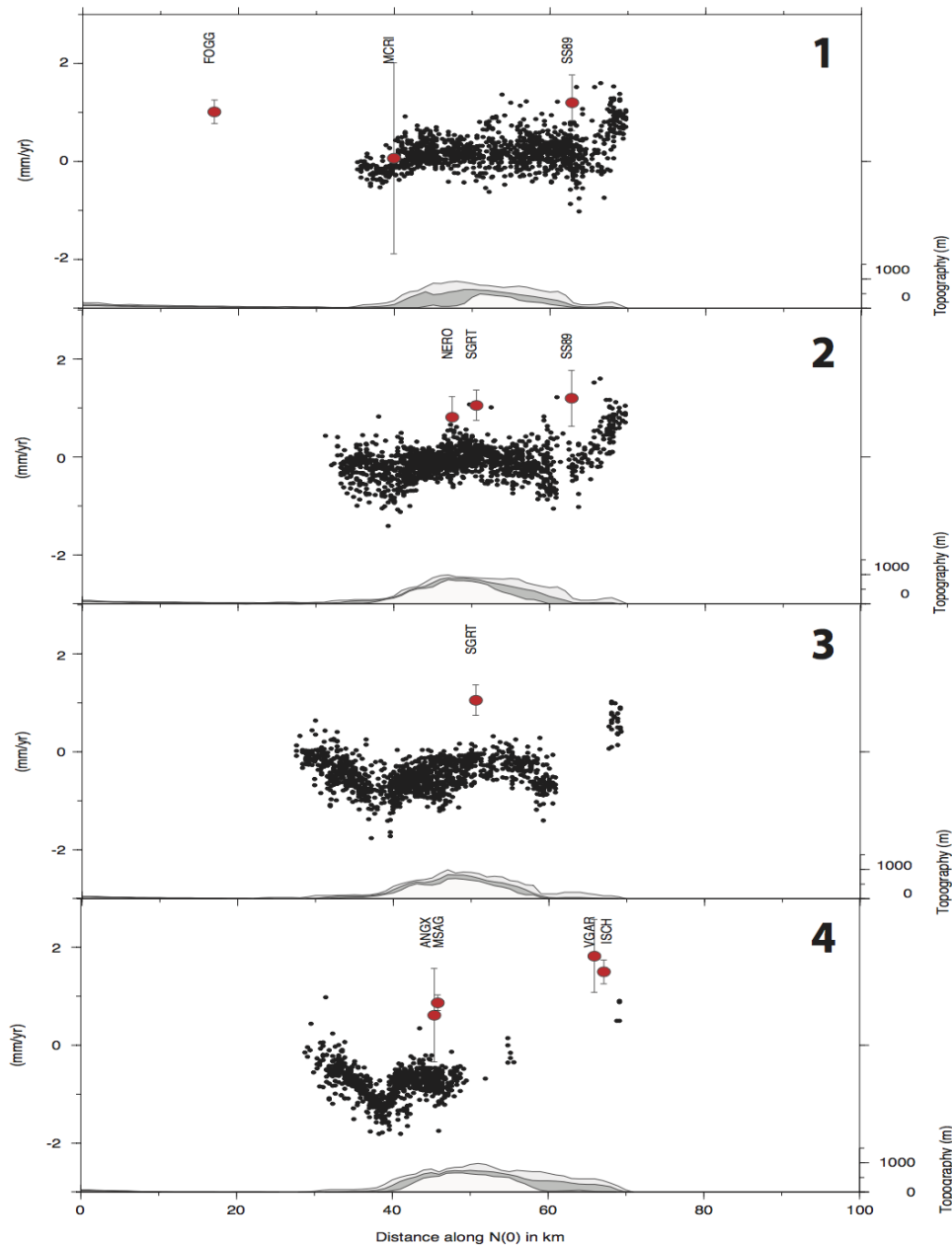
Figure 4.3: *East component of GPS (red dots) and InSAR data (black dots) along the profile lines shown in Fig.4.2, that have origin in correspondence of the stars and considering a swath profile of 6 km wide; below each one are reported the minimum, the mean and the maximum values of the elevation topography.*

in these cases the corrected E-W InSAR velocity field shows a steep gradient along the N-S direction, that should be unreasonable for the geodetic observed deformation rates (section 4.4).
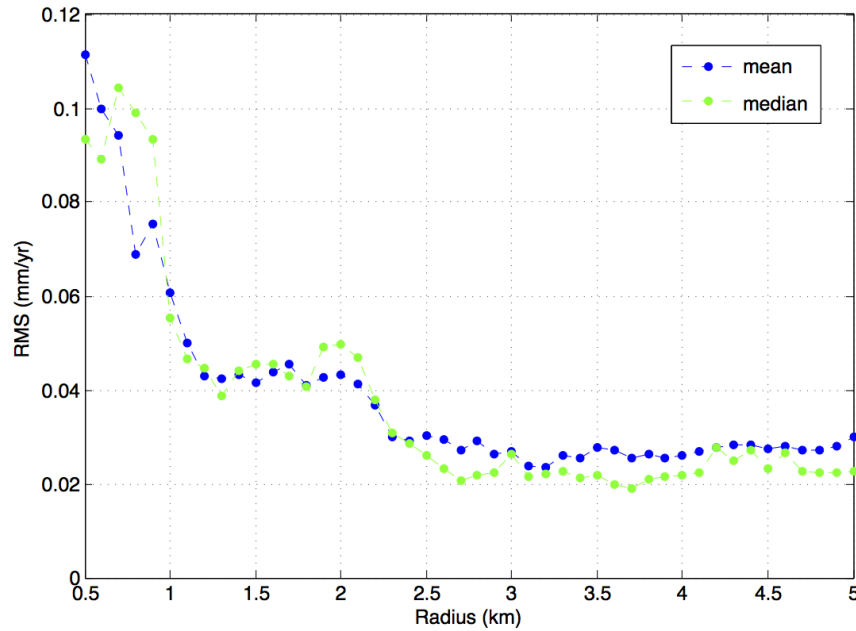
Figure 4.4: *Plot of RMS with the change in the radius; blu and green points correspond to solutions with mean and median InSAR velocity values, respectively*

Therefore we have chosen the solution with the absolute minimum value of RMS given by the median estimation of InSAR representative velocity for a radius of 3.7 km (see Figure 4.4). The corresponding ramp signal and corrected InSAR velocities on East direction are shown in Figure 4.6. The final ramp signal has a principal inclination on NE-SW direction, but the distribution of the four GPS sites is almost aligned along the perpendicular one. This particular configuration may have influenced the unfitting of the ramp correction estimated with small radius, whereas bigger dimensions of neighborhoods may have helped to have a more acceptable solution, where enough pixels aligned along the direction of ramp inclination are taken into account.

Thanks to this approach we have been able to recover the horizontal motion in the East-West direction from InSAR measurements, attached to the same refence frame of the GPS velocity field. The final InSAR velocity map (Figure 4.6B) shows, along the N-S direction, a variation of almost 1 mm/yr as the longest wavelength and a steep gradient in the northern part of 1-2 mm/yr more in few km (see the third profile in Figure 4.5). The reliability of these two signals is confirmed by the well distribution along the N-S direction of GPS sites used for the ramp estimate. The nature of these signals will be the matter of discussion in the following section, in order to understand which origin they may have.
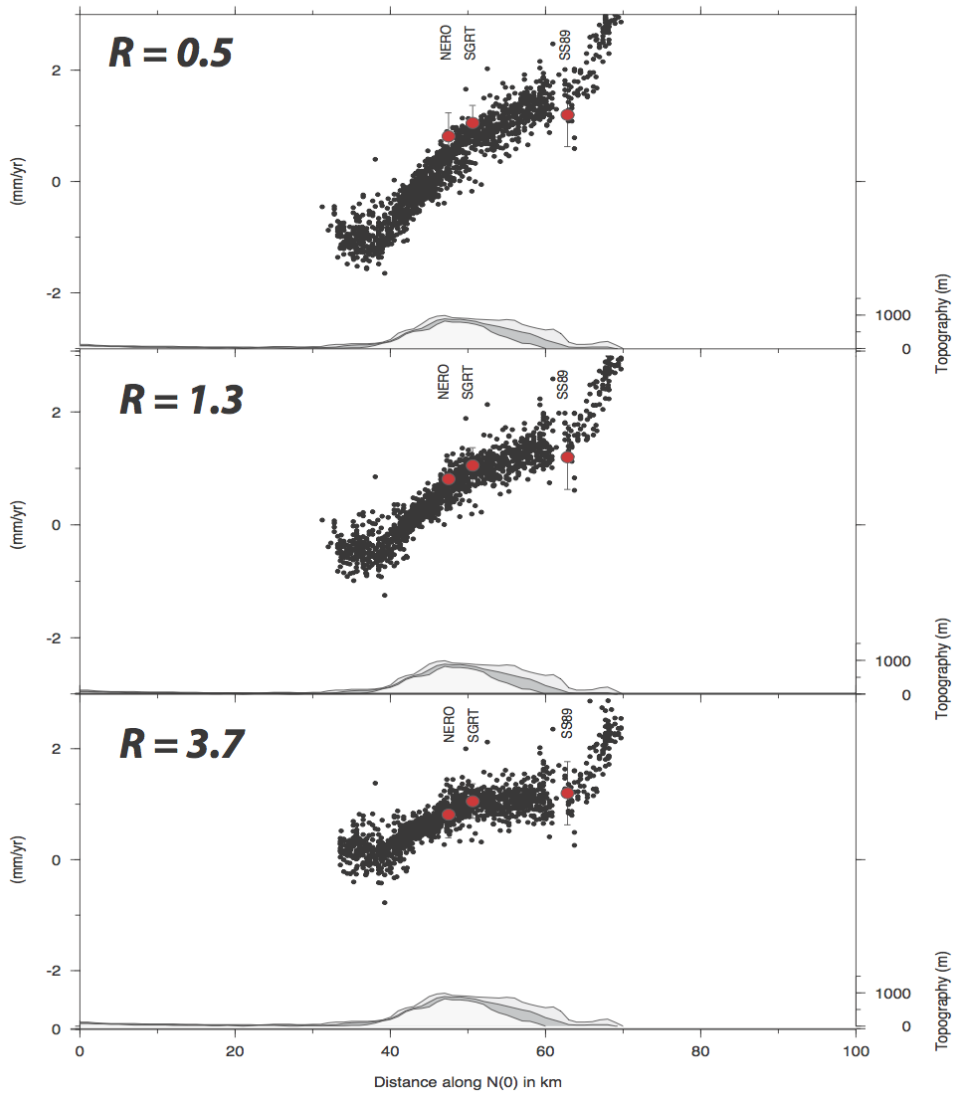
Figure 4.5: *Same kind of profiles as in Figure 4.3 along only line 2 (Figure 4.2) for the InSAR velocities corrected of a ramp signal obtained with different radius (0.5 km, 1.3 km, 3.7 km).*

4.4   Dislocation modeling

The Dislocation modeling is the easiest representation used to reproduce the interseismic deformation observed in proximity of a fault system. As explained in section 1.3, the relative motion of two regions may be assumed as a long buried fault below the seismogenic locked fault (Figure 1.1a). Our purpose is estimate from the data the position, top-depth and slip-rate of the buried fault.

Since this kind of approach assumes surface deformation due to an effect of the elastic contribution only due to the locked fault, it is important to select accurately GPS stations
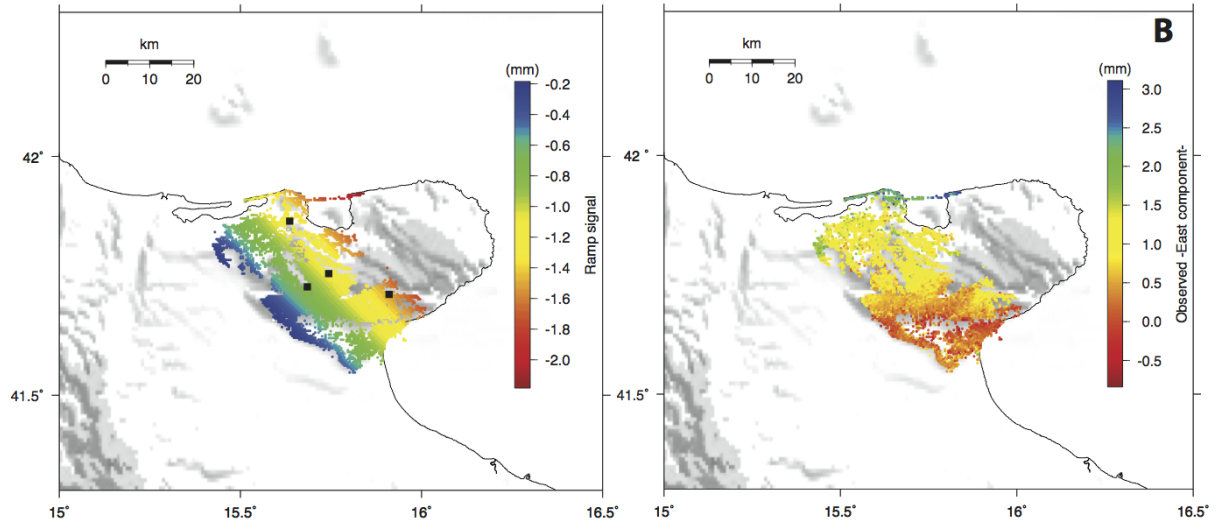
Figure 4.6: *Panel A: Ramp signal removed by original InSAR velocities on East-West direction, black squares indicate position of four GPS stations used; Panel B: InSAR velocities on East-West direction corrected of the linear ramp.*

close to the hypothetical fault position. Moreover their measurments should concern just the elastic signal. In this context we have selected a short list of GPS stations (18 sites) all around the InSAR frame and we have referred velocities of both datasets to a CGPS station far enough from the Gargano promontory and at the same time not close to any other elastic deformation source. As reference station we have choosen the AMUR site (E16.6, N40.9) located in the stable Apulian platform: GPS and InSAR velocities referred to are shown on Figure 4.7. The velocity field highlights a velocity variation for the East-West component of the order of 1 mm/yr that is shown by both datasets.

To model these data we have used a code for the dislocation modeling (section 1.3.1) that perform a constrained non-linear inversion of geodetic data to solve for nine parameters describing the rectangular dislocation and the slip vector (i.e. strike, dip, latitude, longitude, length, width, top depth, strike-slip and dip-slip components). In this case some of these parameters can be fixed. We chose length and width with big values and a fault structure oriented in E-W direction. This may be supported by the fact that the dense InSAR dataset indicates a clear velocity variation along the N-S direction that looks like the typical pattern associated to strike-slip faults (section 1.3, Figure 1.2). This evidence allows also to consider the longitude value irrelevant for the position of fault (fixing this parameter) and in addition the dip-slip component may be neglected since most of the signal is in the East-West direction. In this confiiguration also the dip should not be influent, as already explained in section 1.3, thus we have constrained it to be almost vertical. Finally for the latitude and top-depth of fault we have used wide bounds (Lat: $41.60^o - 41.80^o$, Depth: 0-30 km).
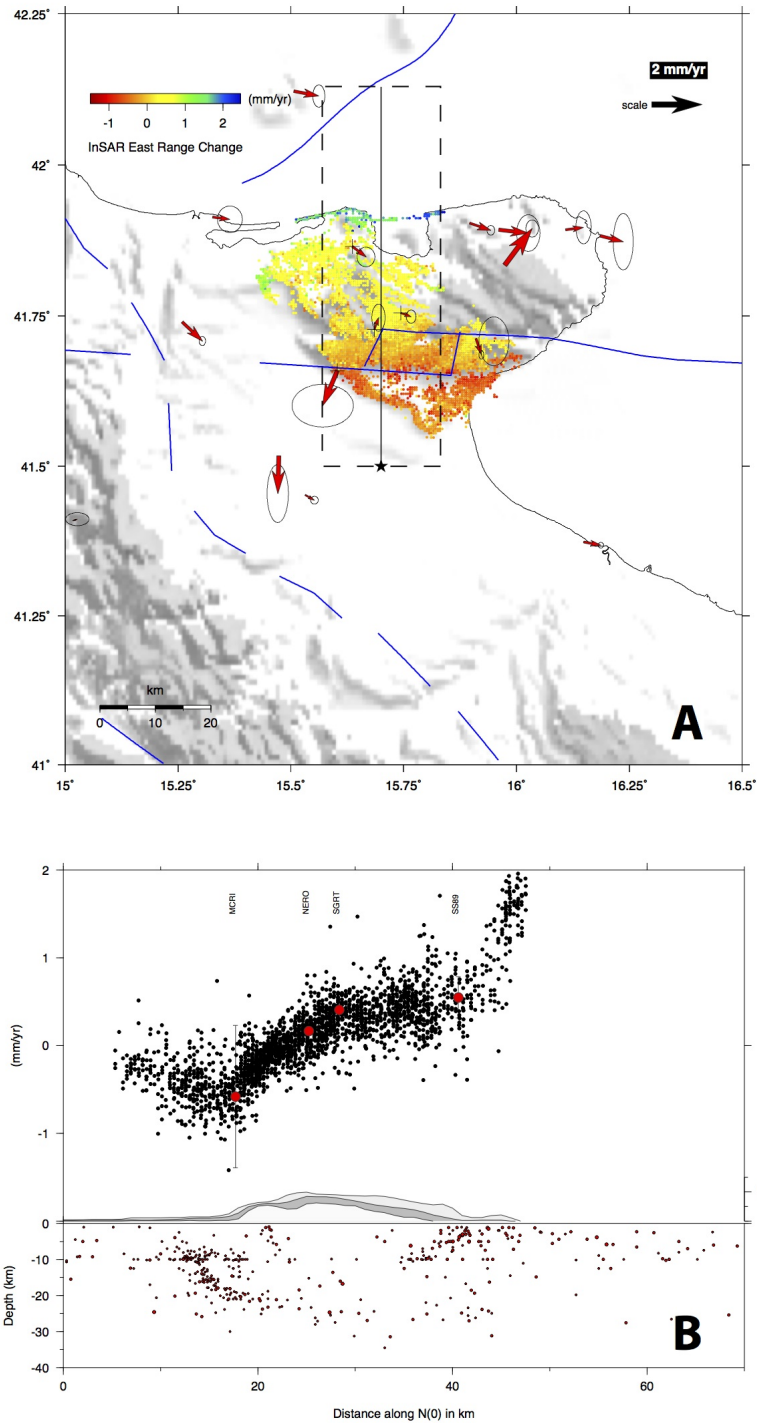
Figure 4.7: *Panel A: GPS and InSAR velocities referred to the AMUR site (E16.6, N40.9), blu lines represent principal fault systems; Panel B: S-N profile of the East component of both datasets within the swath indicated in the panel A, highlighting a long wavelength velocity gradient of the order of 1 mm/yr and a steep gradient of a further 1 mm/yr; below the elevation of topography and the instrumental seismicity of the last 10 years are shown.*

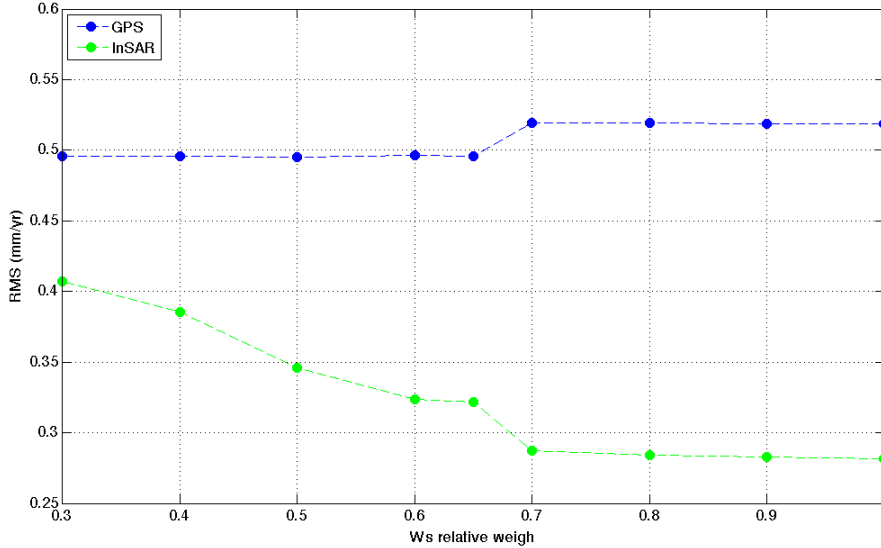We have performed different inversions with only GPS data, only InSAR data and

Figure 4.8: *Trade-off among the InSAR weighting factor Ws and RMS estimates for GPS and InSAR velocities.*

then both datasets jointly, to understand which contributions each dataset may provide. Thus inverting only GPS data with these fault bounds, we obtain a top-depth of ∼30km located at 41.73º of latitude and with very high right-lateral slip rate (∼3 mm/yr) that gives back the RMS = 0.5 mm/yr. This solution with high slip-rate estimate may be due to an inadequate distribution of GPS sites that is lacking mainly in the South. If we invert instead only InSAR data with these fault bounds, we obtain a solution that tries to mediate between the long wavelength signal and the steep velocity gradient in the northern part, failing to model both signals. Actually the second signal has velocity values higher that those observed in the farfield (the farther north station, TREM, has 1 mm/yr in the E-W component) and we suppose that it may be due to some external factors not taken into account during the processing phase. Then we have removed it from the InSAR data and performing an invertion with the same bounds, we obtain a final solution that fits well the long wavelegth signal (RMS = 0.28 mm/yr) with a shallow fault (∼4 km of locking depth) located in proximity of the Mattinata fault (Figure 4.9). The interesting result obtained with this inversion is that this best solution for InSAR data can provide also a good fitting for GPS data for which we have estimated the expected velocities (Figure 4.9A). Thus we have decided to no longer consider pixels interested by the northern signal within the InSAR dataset during all the following analysis.

Finally we perform the joint inversion, using the same bounds, of GPS and InSAR velocities, for which it is first necessary to optimally define the weighting factor Ws for
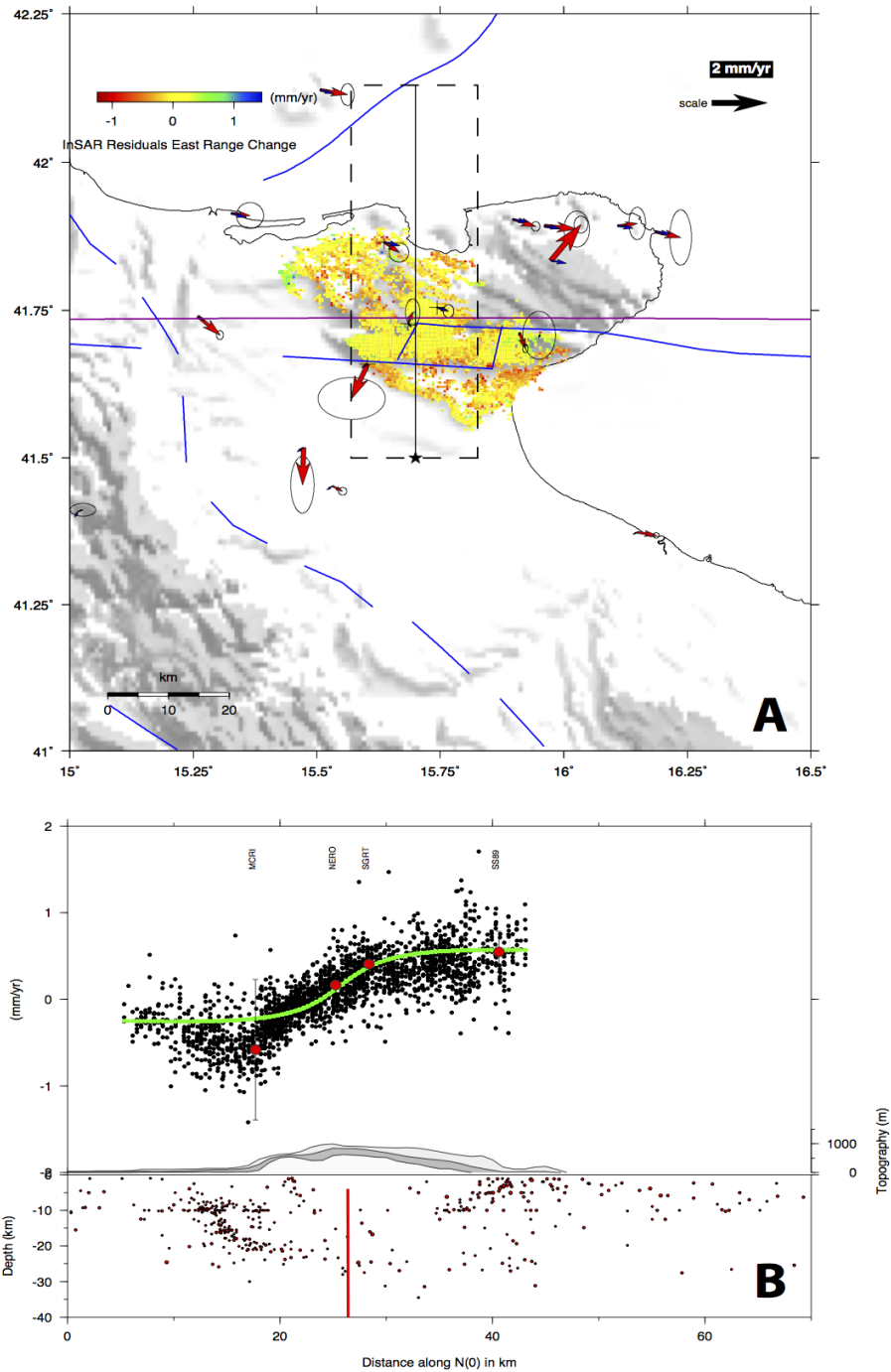
Figure 4.9: *Panel A: InSAR residual velocities due to the fault solution obtained with the inversion of only InSAR data and blu arrows indicate the expected velocities estimate, the violet line represents the fault trace projection at the surface; Panel B: same profile as in Figure 4.7B with modeled InSAR velocities (green line) and the fault extension along depth (red line).*
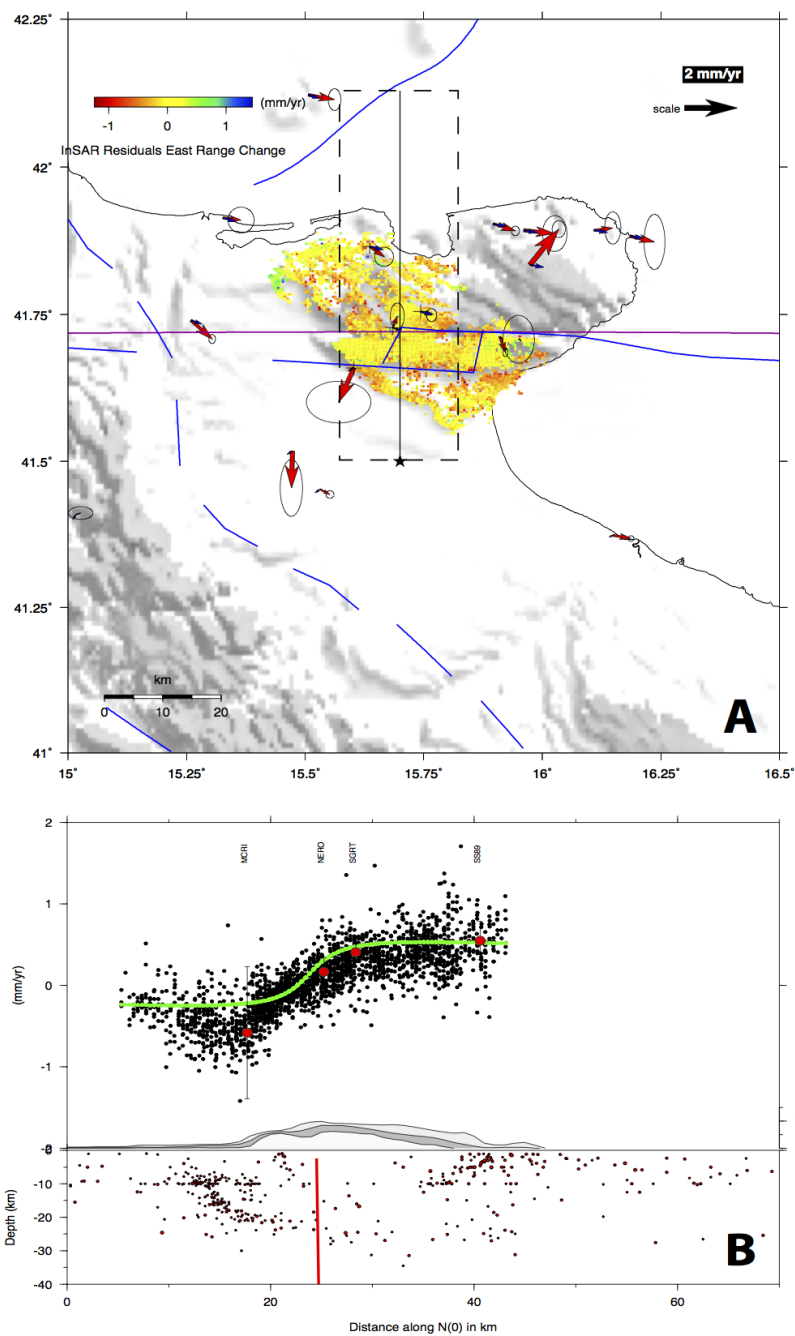
Figure 4.10: *Panel A: InSAR residual velocities due to the fault solution obtained with the joint inversion of GPS and InSAR data and blu arrows indicate the modeled GPS velocities, the violet line represents the fault trace projection at the surface; Panel B: same profile as in Figure 4.7B with modeled InSAR velocities (green line) and the fault extension along depth (red line).*

Figure 4.11: *Panel A: InSAR residual velocities corresponding to two fault fixed geometries for which have been estimated the strike-slip component by the joint inversion of data and blu arrows indicate the modeled GPS velocities, the violet lines represent the fault traces in the surface; Panel B: same profile as in Figure 4.7B with modeled InSAR velocities (green line) and the extension of faults along depth (red line).*

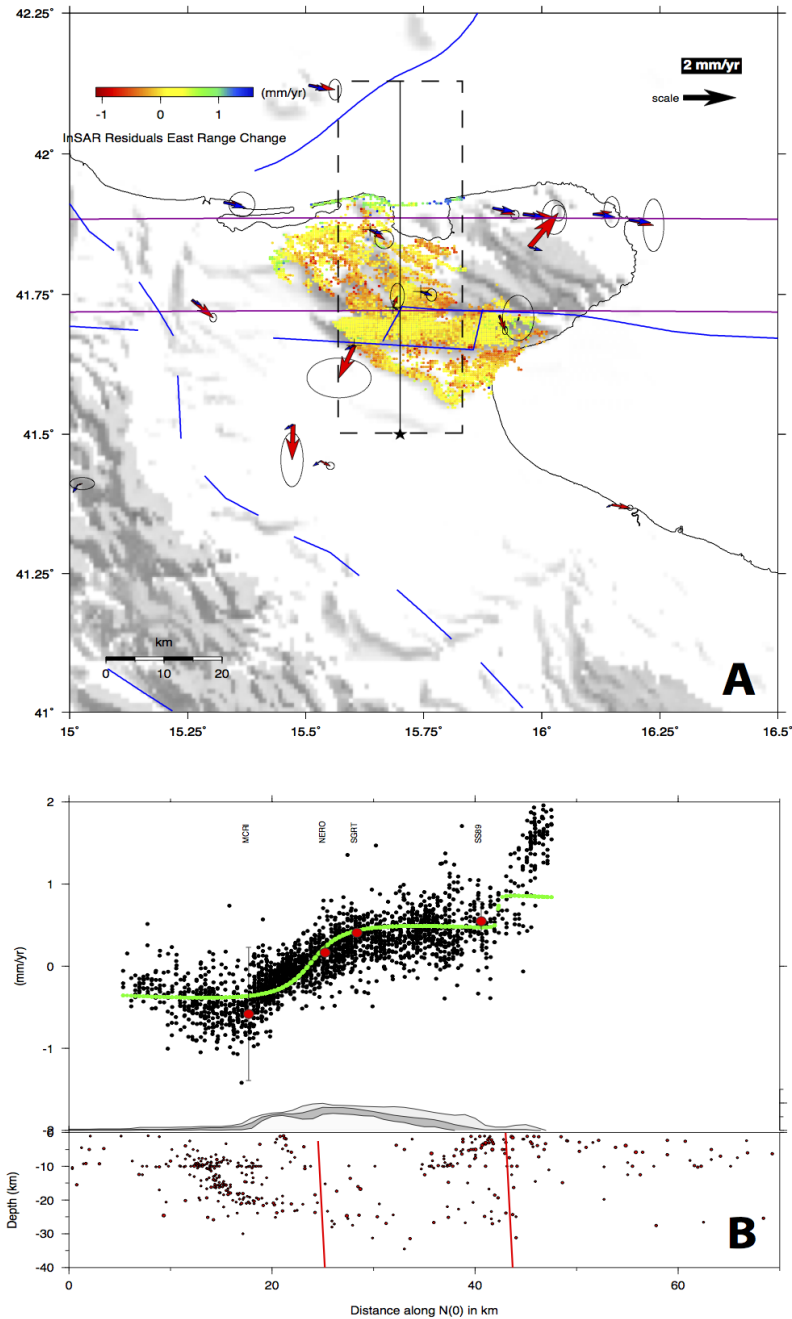the InSAR dataset (section 1.3.1). We have considered a Ws varing from 0.3 to 1 with step of 0.1 and for each one we have inverted data and estimated the residuals (RMS) for both datasets. Figure 4.8 show the RMS trends for GPS and InSAR data as Ws varies and we can see that the GPS RMS increases a little for Ws bigger than 0.7, whereas the InSAR RMS decreases slowly from small values of Ws up to 0.7, beyond which is stable around the same value. Since we have observed a strong instability of the GPS data to recover an appropriate solution and on the other hand a strong ability of InSAR data to detect a fault structure that also well reproduces GPS observations, we have decided to take in consideration high Ws values solutions to give more importance to InSAR data during the inversion. As shown in Figure 4.8, the solutions for Ws values greater than 0.7 provide the same InSAR residuals, obtaining in each case almost the same fault geometry. Thus we have choosen to take as best solution just the mean of the fault parameter values obtained in those cases (Ws $\geq$ 0.7) and it consists on Lat = 41.715^o, depth of 2.5 km and a right-lateral slip rate of 1 mm/yr. It is easy to observe in Figure 4.10 that, since the high values of Ws factor, this solution provide a fit similar to that obtained with the only InSAR inversion (Figure 4.9). However it is worth to note that the GPS data are never well modeled, having systematic residuals due to an underestimation of the east component in the north and of the north component for the few stations south of the fault. This second kind of residual may be due to the strictly strike-slip configuration that doesn't take into account for any N-S movement. However these GPS stations are few and scattered, and do not allow to constrain any fault system with slip along dip.

Moreover we have performed a further test to evaluate the non-tectonic nature of the northern steep velocity gradient removed from the InSAR frame. We have fixed two deep fault geometries, one in correspondence of the best solution just found and the second one in the north with a very shallow locking depth. We have inverted jointly the two datasets with Ws=0.8 just to get the strike-slip component for these two faults. Figure 4.11 shows the result of this inversion, that in particular produces a better fitting of the GPS data in the north, but on the other hand the steep velocity gradient is still largely underestimated. Therefore this result gives firstly the proof that the rapid variation of the E-W InSAR velocities in the north cannot be modeled by a second strike-slip fault structure consistent with the kinematic frame provided by GPS data. Thus we infer that this signal may have likely a non-tectonic origin. Moreover this test provides also an indication about the sistematic residuals observed in the north for GPS data, that can be modeled by the second fault. This result may be interpreted as an indication of a possible presence of a further active fault system, but it is too hard to account for it since the sea does not allow to have an appropriate data coverage. However this signal may be modeled also by a rotational velocity due to the relative motion of the two regions and this case will be presented in the next section.

4.5 Block modeling with GPS and InSAR data

To study the kinematics of the Gargano promontory with the block modeling approach, we have defined a very simple block-model in order to have less blocks as possible and to focus the attention on this specific plate boundary. Considering the seismo-tectonic context in which the promontory is inserted (section 4.2), the Gargano may be assumed as one of the possible plate boundaries between North-Adria and South-Adria (or Apulia) plates, which the relative motion generates a widespread deformation in the central Adriatic (D'Agostino *et al.*, 2008). We define the plate boundary following the Gargano-Dubrovnik line (Oldow *et al.*, 2002). The Apulia block is bordered to the west by the Tyrrhenian plate by means of a normal-fault system placed in the southern Appenines. The North-Adria (or just Adria) plate is well defined by geodetic measurements as an independent block (Calais *et al.*, 2002; Battaglia *et al.*, 2004; D'Agostino *et al.*, 2008; Devoti *et al.*, 2008). Since the used GPS velocity field is referred to the Eurasia fixed frame (section 2.2.2), we consider four main blocks: Eurasia (Eu), Adria (Ad), Apulia (Ap) and Tyrrhenian (Ty). The block geometry and the selected GPS velocity field are shown in Figure 4.13, where the locking depth of block boundaries is also indicated.

In particular we have selected 225 stations within these blocks, avoiding to consider sites close to the boundaries, except for the Gargano area and the southern Appennines. For the normal faults in the Southern Appennines we have used the fault parameters provided by the Italian fault catalog DISS (2010). Whereas for the Gargano promontory we have defined a long vertical fault located in the same position identified during the Dislocation Modeling analysis (section 4.4).

In this section we will use the block modeling approach to solve for the rotational rates and poles in a linear least squares sense (section 1.4.3), without estimating the intrablock strain tensor (section 1.4.2). We have used firstly only GPS data to detect the kinematic constraints that the GPS measurements provide in this kind of approach. Then we have considered the joint inversion with the InSAR velocities corrected of the planar ramp (section 4.3.1) in order to evaluate how the InSAR dataset may be integrated within the block modeling.

4.5.1 Block modeling inversion of GPS velocities

To define the optimal locking depth (LD) of the Gargano fault for the GPS velocities within our kinematic frame, we have performed several block modeling inversions with varing LD from 0 km to 40 km with step of 5 km and estimating for each one the residual GPS χ_r^2 (chi squared per degrees of freedom) and the mean absolute value of GPS residuals. The corresponding trend of GPS residuals is shown in Figure 4.12 where we observe a minimum for a locking depth of 15 km giving a $\chi_r^2 = 2.32$ and a mean residual of 0.515 mm/yr. This solution associates to the Gargano fault a right-lateral long-term slip rate of 1.1 ± 0.3 mm/yr, that is quite in agreement with values reported by other analysis (Piccardi, 1998; Tondi *et al.*, 2005; Di Bucci *et al.*, 2006) (section 4.2). The rotational poles of each block with respect to Eurasia fixed are reported in Table 4.1

and the angular velocities are positive for counterclockwise rotations. The Adria-Eurasia (Ad-Eu) pole we computed agrees with previous determinations in predicting most of the first-order seismotectonic features around the Adriatic microplate (Anderson & Jackson, 1987; Ward, 1994; Calais *et al.*, 2002; Battaglia *et al.*, 2004) and also with the following more accurate estimates performed with denser GPS velocity fields (Serpelloni *et al.*, 2005; D'Agostino *et al.*, 2008; Devoti *et al.*, 2008).

This kinematic frame will be taken into account as a reference result for the following joint inversions of GPS and InSAR datasets, to understand which contribution and information InSAR data may suggest in a kinematic approach.
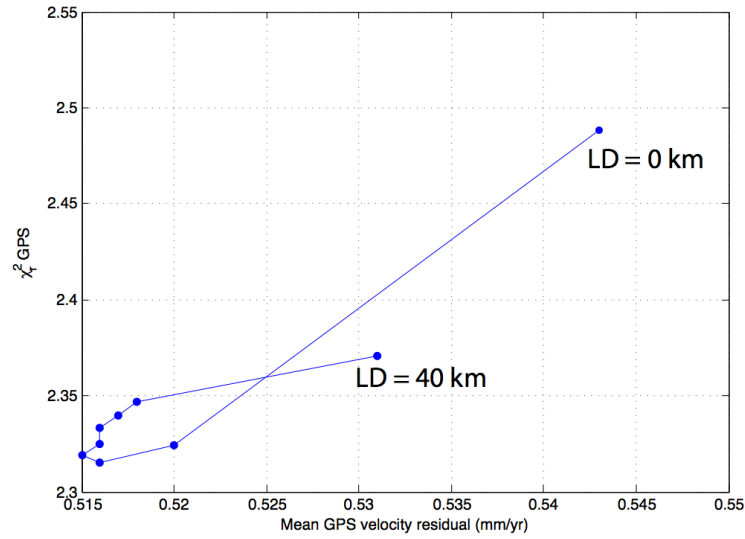

Figure 4.12: *Trade-off plot between the mean GPS velocity residuals and the corresponding* χ_r^2 *of block modeling inversions for only GPS data, with locking depth values of the Gargano segment from 0 km to 40 km by step of 5 km.*

Plate	Lon	Lat	σ_{Lon}	σ_{Lat}	Ω	σ_Ω
Ad-Eu	7.235	45.307	0.399	1.299	0.278	0.006
Ap-Eu	33.856	36.749	3.450	4.287	-0.162	0.012
Ap-Ad	17.804	42.904	1.087	1.826	-0.432	0.014
Ty-Eu	4.046	37.674	0.965	3.185	0.104	0.006

Table 4.1: *Plate angular velocities. Lon = Longitude (E); Lat = Latitude (N);* σ_{lon} *= 1σ uncertainty on Longitude estimate;* σ_{lat} *= 1σ uncertainty on Latitude estimate;* Ω *= rotation rate in deg/Myrs and positive for counterclockwise rotation;* σ_Ω *= 1σ uncertainty on rotation rate estimate*
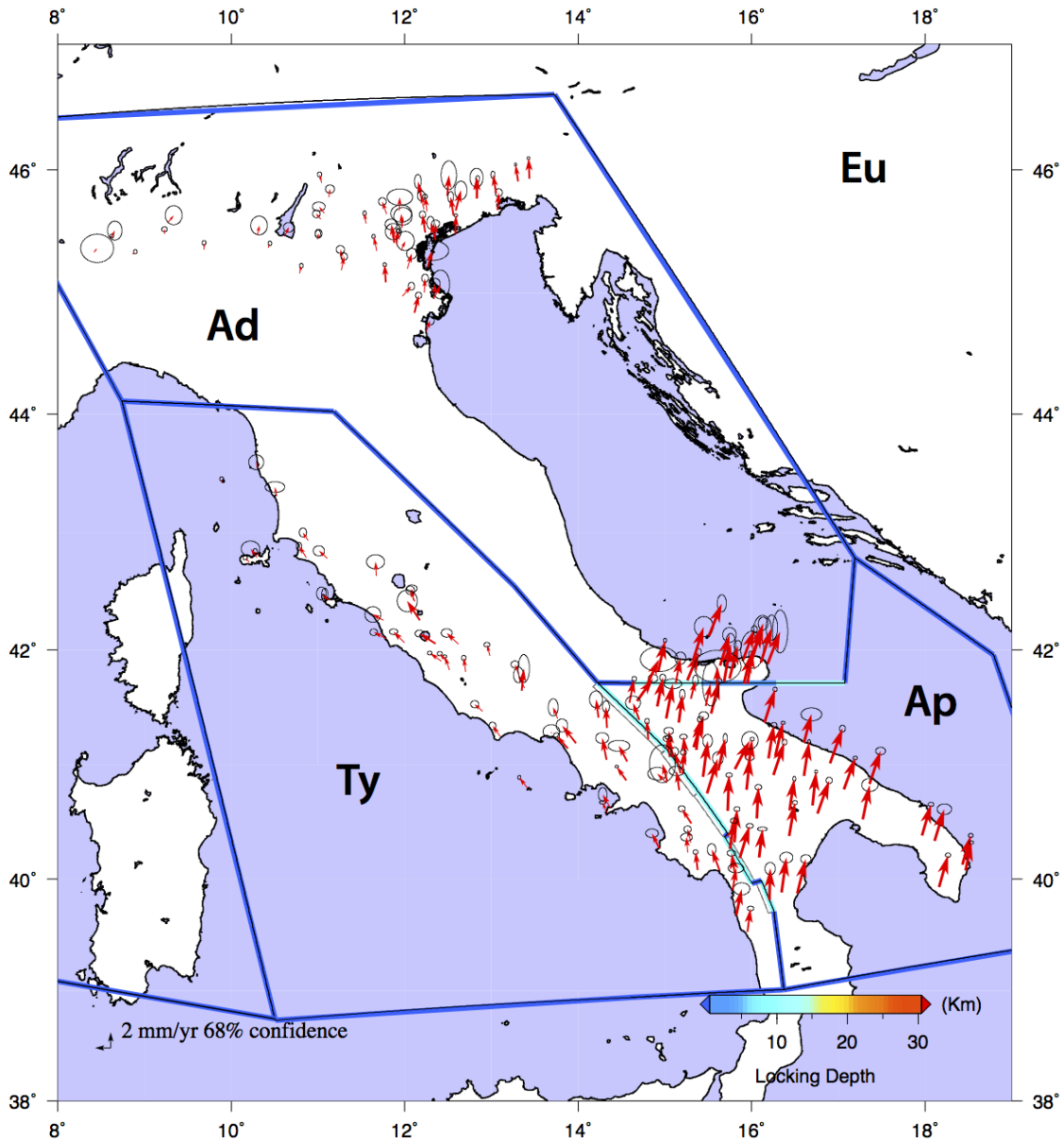
Figure 4.13: *Block definition and selected GPS velocities given wrt Eurasia fixed frame; the color of block boundaries indicates for each fault segment the corresponding locking depth of the block-model used for the joint inversion of GPS and InSAR data.*

4.5.2 Joint inversion of GPS and InSAR data

To invert jointly GPS and InSAR velocities with the defined block-model, we have decided to divide the Gargano fault in three segments, in order to set different locking depths depending on which kind of data may influence each segment. In fact knowing that InSAR data are well explained by a shallow locking depth (section 4.4), we should consider this

feature within our block-model definition, because otherwise it would be impossible to understand which contribution may be apported InSAR velocities within the BM approach. Thus we have setted for the central segment (i.e. Mattinata fault) the same locking depth obtained with the dislocation modeling approach and for the external ones the best value of locking depth found in the previous section (Figure4.13). Inverting with only GPS data this modified geometry, the plate rotational velocities slightly change, but they still remain within the previous uncertainties, giving just a little higher reduced chi squared ($\chi_r^2 = 2.34$).

The aim of this inversion is to evaluate how this kinematic configuration is consistent with the InSAR velocity field that has been attached to the same GPS reference frame. In fact the extremely localized presence of InSAR data may not contribute to the angular velocities estimation, that would need instead of a widespread signal. However the important contribution that this InSAR velocity field may provide strictly concerns with the nearfield deformation on the Mattinata fault.

Thus we have used our modified code of Meade & Loveless (2009) to invert jointly GPS and horizontal InSAR velocities (Appendix A) and solve for the rotational poles. For the previous considerations, we should use a low weighting factor (Ws) for the InSAR dataset (Appendix A), in order to reduce its numerical influence on the final solution. Initially we have choosen a very low Ws value (Ws = 0.05), to be sure that the solution has not been influenced by inSAR data. Nonetheless these settings has produced an unexpected result, for which the InSAR and GPS velocities are systematically overestimated (Figure 4.14). In order to provide an order of magnitude of this shift between observed and modeled velocities, we have computed the mean value of the InSAR velocity residuals (MIVR). Usually this value should be close to zero, instead in this case we obtain a MIVR of the order of -0.5 mm/yr. We suppose that this outcome has to be interpreted as a sign of a limit of our block-model settings. We are not able to well reproduce the nearfield velocities of Ad-Ap plate boundary with sub-millimeter precision, likely due to an insufficient GPS data coverage. Nevertheless, the resulting plate angular velocities are in agreement with other solutions presented by previous works (at least as the more constrained Adria plate is concerned). Some other fault system located in the north that are not considered within our block-model definition might reduce the MIVR estimate.

Thus we have performed a test adding one more block that bounds the Gargano promontory by means of a long E-W fault in the north close to the coast and we have inverted only GPS data using this new geometry. To consider acceptable the new geometry we firstly compute the F test (Stein & Gordon, 1984) to infer whether the fit to the data resulting from the block-model changing warrants that change.The F test assesses the change in the weighted misfit variance (χ^2) resulting from a change in the number of degrees of freedom between the two models. We obtain an F value of 11.18 (ending is positive for F values greater than 3.78) indicating that a further block may be taken into account to produce a better fit of the data. This highlights also that the deformation occurring in the Gargano area needs to be accommodated by more than only one fault system. However the long-term slip rates resulting from this last inversion are not in agreement with the expected kinematics for the region. In particular the added northern E-W segment turns
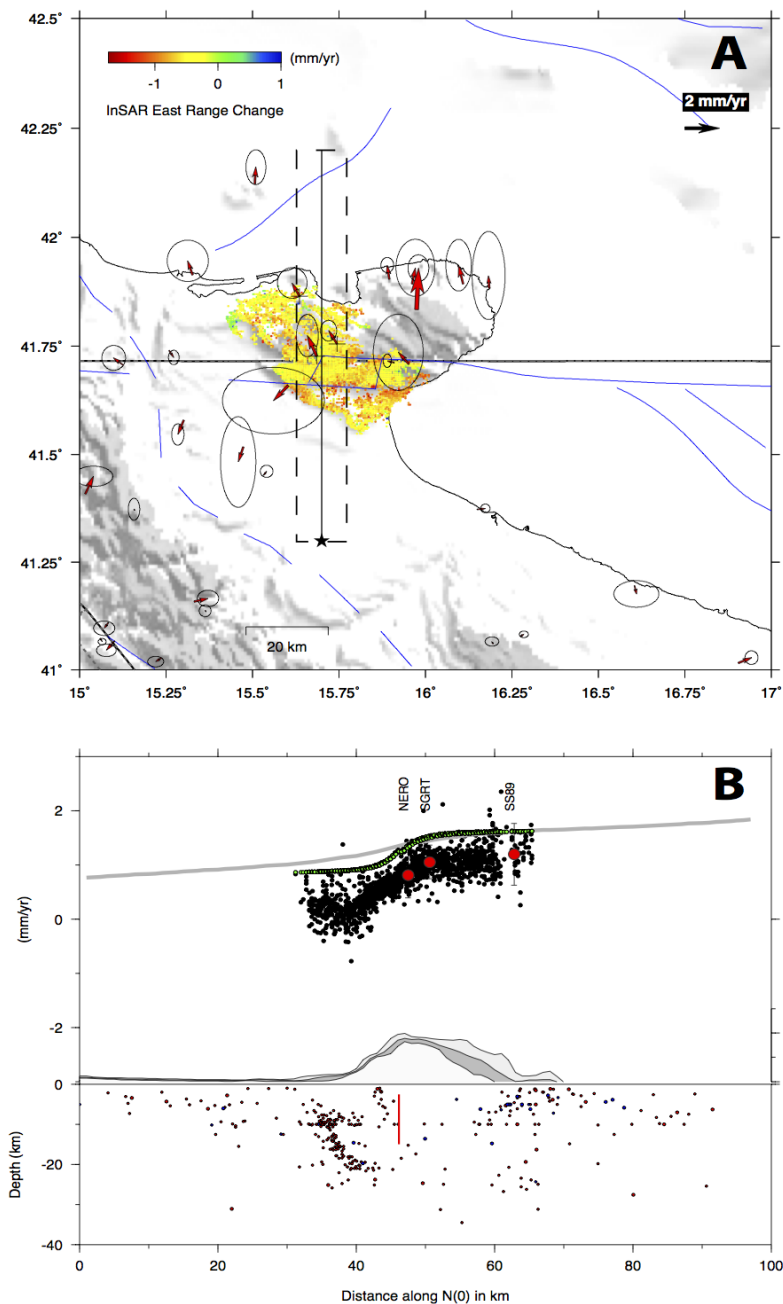
Figure 4.14: *Panel A: GPS and InSAR residual velocities obtained in the block-model joint inversion with a weighting factor Ws = 0.05; the black lines indicate the block boundaries positions and the error ellipses are at a 68% of confidence; Panel B: cross section along the swath profile in Panel A of observed, red and black dots, and modeled, gray line of interpolation and green dots, of the East component velocities for GPS and InSAR data, respectively; the red line indicates the block boundary extension along depth.*

Figure 4.15: *Same characteristics of Figure 4.14, but with results obtained with Ws = 0.4.*
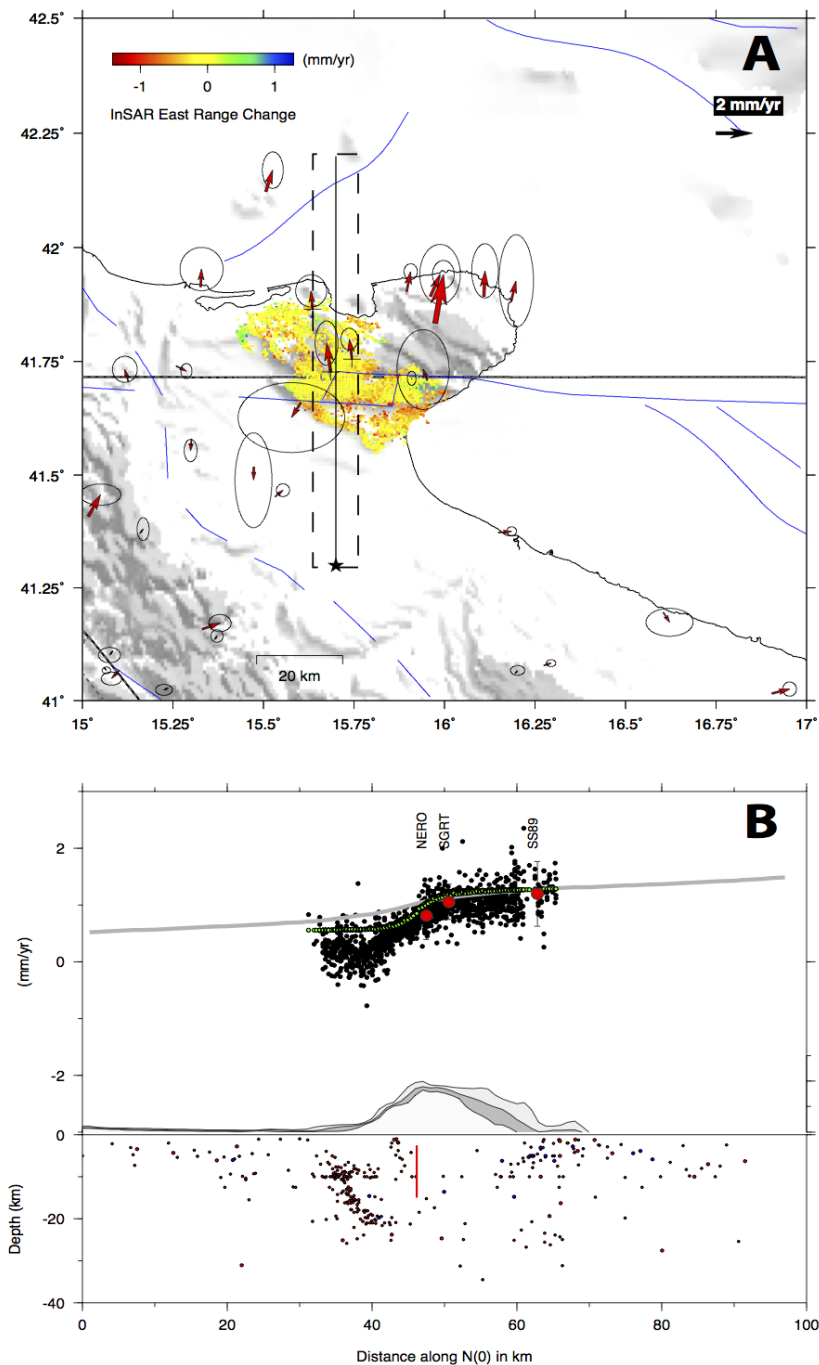
out to be characterised by a left-lateral movement, instead of right-lateral one as reported
by the principal seismological analysis performed for the northern sector of the Gargano
(Milano *et al.*, 2005; Del Gaudio *et al.*, 2007). This means that the rotational movement

of this further block is not well constrained by the available data, regardless of the F test
positive ending, and it may likely influence wrongly the modeled near-field velocities of
the Mattinata fault.

For the reasons just exposed, we choose to not consider any further added block in our
following modeling for the interseismic coupling degree estimates, counting on the near-
field velocity of InSAR data in order to estimate the coupling pattern. To achieve a fairly
fit of InSAR data reducing the constant mismatch, we have considered higher Ws values
to observe how much the MIVR is reduced. We have performed several joint inversions
as Ws changes from 0.05 to 1 with step of 0.05, and we have observed an acceptable
modeling of InSAR data with at least a MIVR = -0.2 mm/yr obtained with Ws = 0.4
(Figure 4.15) providing a GPS $\chi_r^2 = 2.65$.

In the next section we presented the block modeling inversions for the intersismic coupling
distribution using jointly GPS and InSAR data. For this purpose we shall evaluate an
appropriate Ws value to increase the MIVR estimates, but also to restain GPS residuals.

4.6   Interseismic coupling of Mattinata fault

We have tried to evaluate which information these data may provide about the interseis-
mic coupling degree for the Mattinata fault. We used the modified Block Modeling code
of Meade & Loveless (2009) to invert jointly GPS and horizontal InSAR velocities (Ap-
pendix A) to solve simultaneously for the rotational poles and the coupling distribution
ϕ (section 1.4.1). Using the same block-model geometry defined in previous sections, we
have subdivided the rectangular surface of the Mattinata fault in Triangular Dislocation
Elements (TDEs) using the free program *DistMesh* (Persson & Strang, 2004), in order
to allow the elastic contribution to vary along strike and dip. We have considered the
same segment dimension along strike and we have defined a plane width of 30km and the
element size of ∼3km. We have considered during our applications both inversion tech-
niques (section 1.4.3) consisting on the Linear Least Squares (LLS) solver and a Linear
Constrained Algorithm (LCA , Coleman & Verma, 2001), in order to evaluate limits and
strenghts of both approaches. We will firstly present the solution obtained with the LCA
method and then the other one from the LLS solver, comparing the results.

   Within the minimization problem providing the best solution, we should define the
optimal weighting factor Ws between two datasets. Since we have in this case an over-
determined problem (number of data greater than number of unknowns) in theory the
coupling regularization is not needed. However we have applied the same a slight regular-
ization for the slip distribution in the LCA method, showing that it is not influent during
the inversion. Instead in the LLS inversion we should estimate as well the smoothing fa-
tor β (section 1.4.2) that controls the back-slip regularization to limit the slip magnitude
(Loveless & Meade, 2010). We do not have applied any slip constraints for the TDEs to
force them to taper to zero at the fault edges.

Using the LCA method we are able to constraint the slip components of the back-slip dis-
tribution, setting as a lower limit value the long-term slip rate obtained for the Mattinata
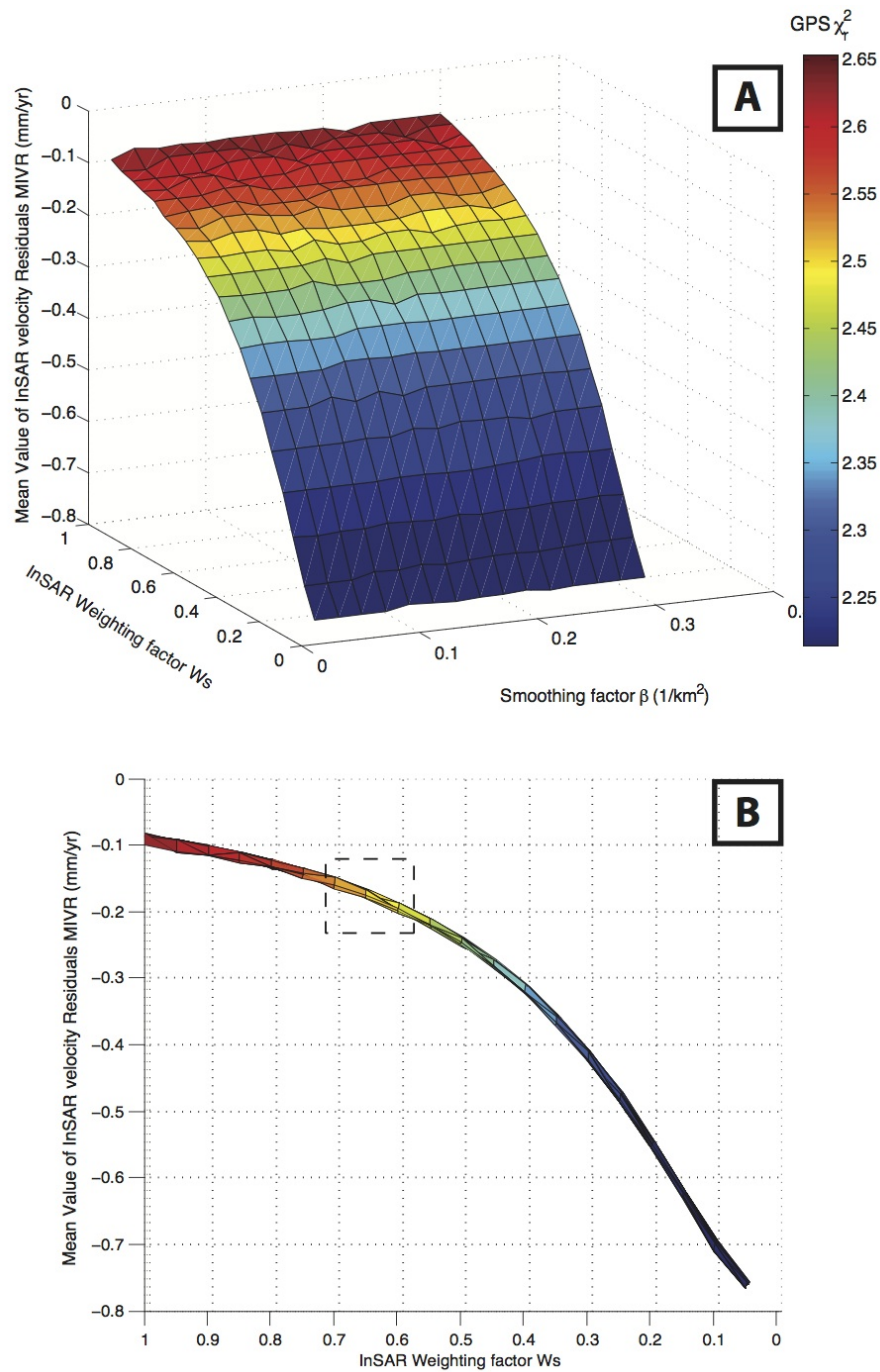
Figure 4.16: *Panel A: 3D trade-off between the GPS χ_r^2 and the MIVR for all values of Ws and β using the LCA approach; Panel B: lateral point of view of Panel A that exhibits the MIVR depending on Ws, dashed box indicates the solution corresponding to the chosen Ws value = 0.65; the color palette is the same of Panel A.*

fault segment during the block modeling GPS inversion (i.e. 1.1 mm/yr right-lateral, section 4.5.1), and the maximum limit has been set to zero. Thus we have performed systematic inversions as Ws changes from 0.05 to 1 with step of 0.05, and for each Ws value we have considered varing β quantities from 0.02 km^{-2} to 0.3 km^{-2} by step of 0.02 km^{-2}. In Figure 4.16A we show the GPS (χ_r^2) and InSAR (MIVR) residuals obtained for the Ws and β values considered and we can see clearly that both kind of misfits are influenced only by the Ws factor values, whereas the β factor does not affect to the final residuals. Thus we have decide to use $\beta = 0.1 km^{-2}$, to have a slightly regularized coupling solution. To evaluate instead the optimal weighting factor Ws value we consider the MIVR estimates for each Ws step (Figure 4.16B). Since in the last section we have identified a minimum value of MIVR ($MIVR_m$=-0.2 mm/yr) that allows to have well-reproduced InSAR data, we should choose the Ws value for which the MIVR is greater than $MIVR_m$. Thus looking to the Figure 4.16B, we observe that the factor Ws should be greater that 0.6 to get MIVR values higher than $MIVR_m$. We choose Ws = 0.65, in order to have a slighly reduced MIVR (- 0.18 mm/yr), and at the same time relatively low GPS residuals ($\chi_r^2 = 2.52$). The corresponding coupling degree distribution is shown in Figure 4.18 and it presents two main asperities, one long, shallow (3-5 km of thickness) and just below the area interested by the InSAR frame, and the second one deeper, bigger and extended from 20 to 30 km of depth. The related GPS and InSAR residuals are shown in Figure 4.17A, whereas the N-S cross section of model fitting for InSAR data is presented in Figure 4.17B.

We have verified the reliability of this solution by mean several checkerboard tests considering the Ws and β values just used, and we will present our results in the next subsection.

Now we present instead the coupling distribution solution obtained with the LLS solver and we have perform several inversions to assess a suitable choise for Ws and β. The latter parameter in this approach has the role of giving more importance to the regularization in order to limit the back-slip magnitude that may be overestimated (section 1.4.3). Thus we have executed systematic inversions as Ws changes from 0.05 to 1 with step of 0.05, and for each Ws value we have considered varying β from 10 km^{-2} to 200 km^{-2} by step of 10 km^{-2}. In Figure 4.19A we show the GPS (χ_r^2) and InSAR (MIVR) residuals obtained for the Ws and β values considered and we can observe that the latter parameter may influence the solution suggesting small β quantities for whatever Ws value (with reference of GPS residuals). Moreover looking at the Figure 4.19B that shows the trend of the MIVR as Ws changes, we can identify some likely solutions for Ws among [0.3,0.4] (dashed box), respecting the constraint of the minimum value of MIVR and for which GPS residuals may be still limited. However to choose the more suitable smoothing factor value we have to consider the strike-slip component of the back-slip distribution, which has to be comparable to the long-term relative plate motion (Loveless & Meade, 2010). Figure 4.20 shows the maximum (Panel A) and the minimum (Panel B) value of the strike-slip component of the back-slip distributions as β varies. In this case the expected values should be zero and -1 mm/yr, as maximum and minimum constraints, respectively. However Figure 4.20 shows that the minimum is achieved with initial β values, but the
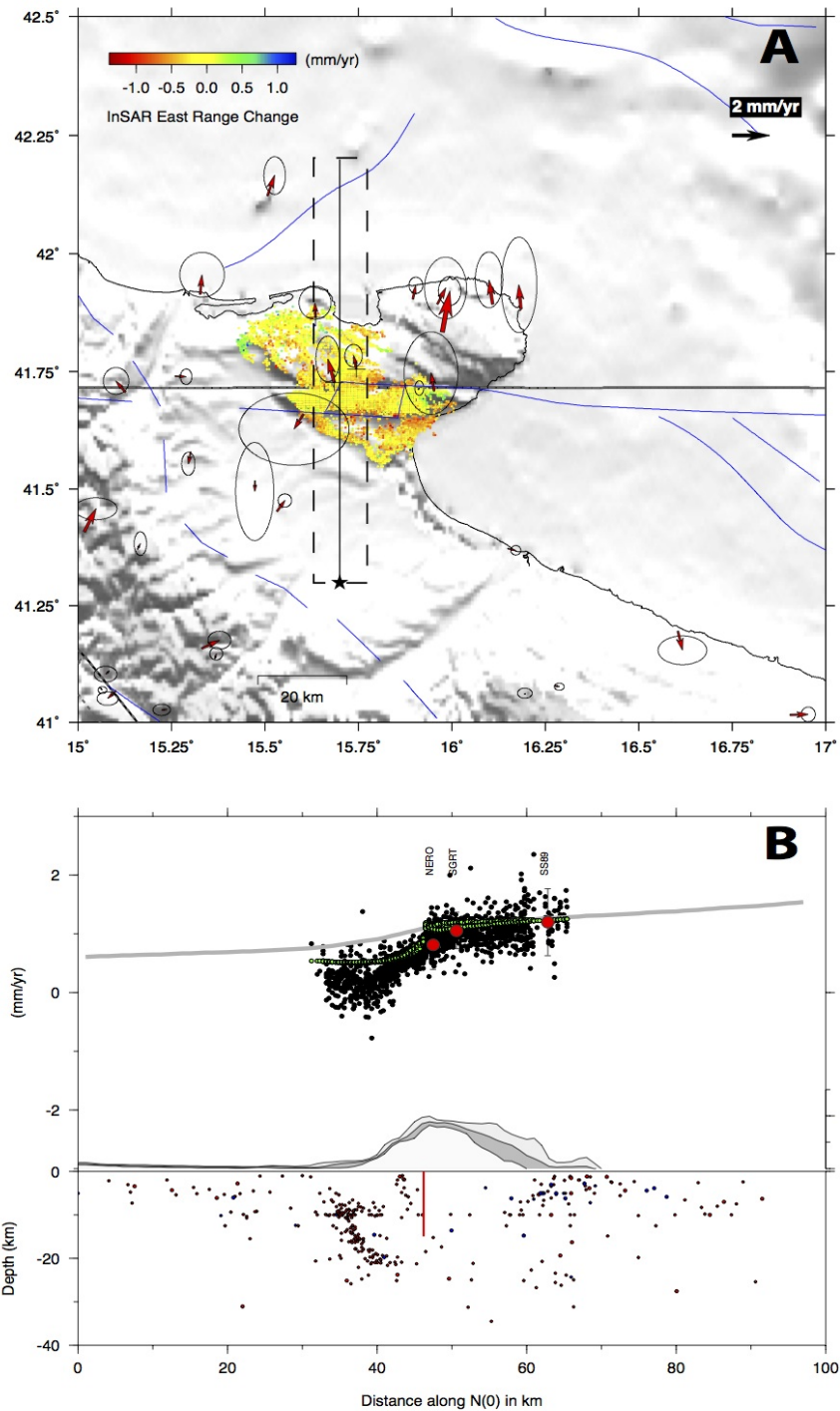
Figure 4.17: *Same characteristics of Figure 4.14, but results obtained with the LCA method for the coupling distribution estimate with Ws = 0.65 and $\beta = 0.1\ km^{-2}$.*
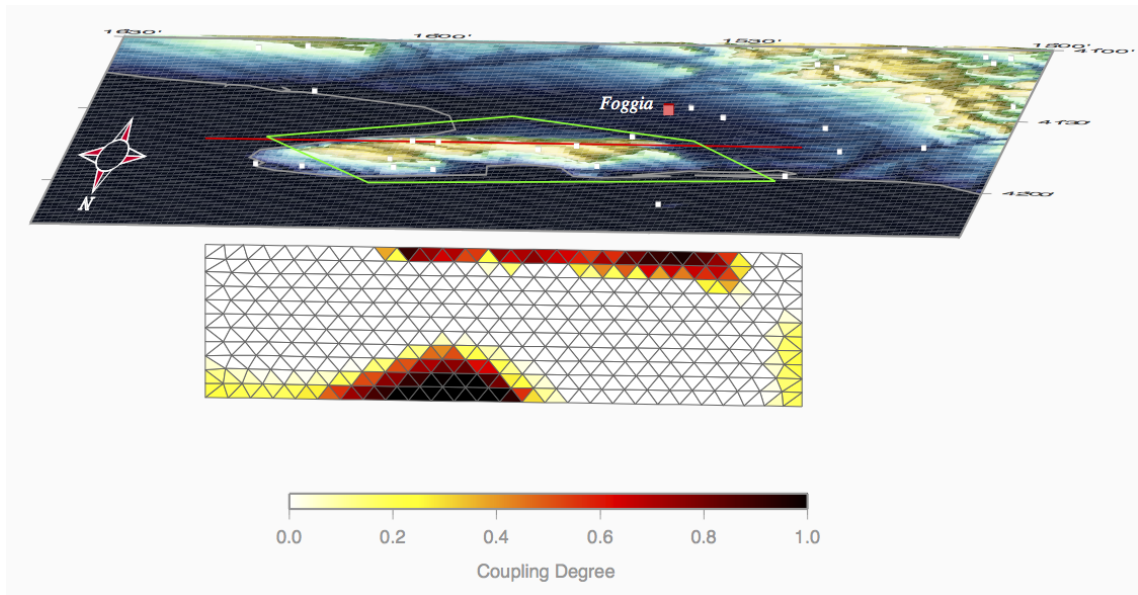
Figure 4.18: *Imaging with a 3D view of the interseismic coupling distribution obtained with the LCA method setting Ws = 0.65 and β = 0.1 km^{-2}; the green polygon indicates the InSAR frame position in map and the red line is the fault trace at the surface; the look angle of fault is N−5° and the wind rose specifies the map orientation.*

maximum is rather far to reach that limit. We suppose that this particular result may be due to the limit of our block-model definition to well reproduce the nearfield velocities of Ad-Ap plate boundary (section 4.5.2). That being so, we decided to choose β and Ws values for which we obtain a consistent minimum of strike-slip component, but not too high corresponding maximum one, and at the same time tring to get GPS and InSAR residuals as small as possible. For these reasons we have defined as optimal solution that one corresponding to Ws = 0.35 and β = 50 km^{-2}, providing a GPS χ_r^2 = 2.48 and a MIVR = -0.18 mm/yr. The related GPS and InSAR residuals are shown in Figure 4.21A, whereas the N-S cross section of model fitting for InSAR data is presented in Figure 4.21B. The corresponding coupling degree distribution is shown in Figure 4.22 and it is characterized by just one principal asperity, long and shallow similar to the solution found with the LCA method, but much more smoothed. We have to point out that the color palette of this figure is saturated at boundaries [0,1], but having positive strike-slip components the coupling ϕ ranges also in negative values (Eq. 1.5), that are integrated in the white areas.

Thus the coupling degree distributions found with the two distinct methods are not too much different the one from the other and moreover their corresponding residuals for GPS and InSAR velocities are very similar. The ability of the LCA method to constrain the slip magnitude is still the principal benefit of this approach, but however we cannot define if any of the two solutions might be the best one.
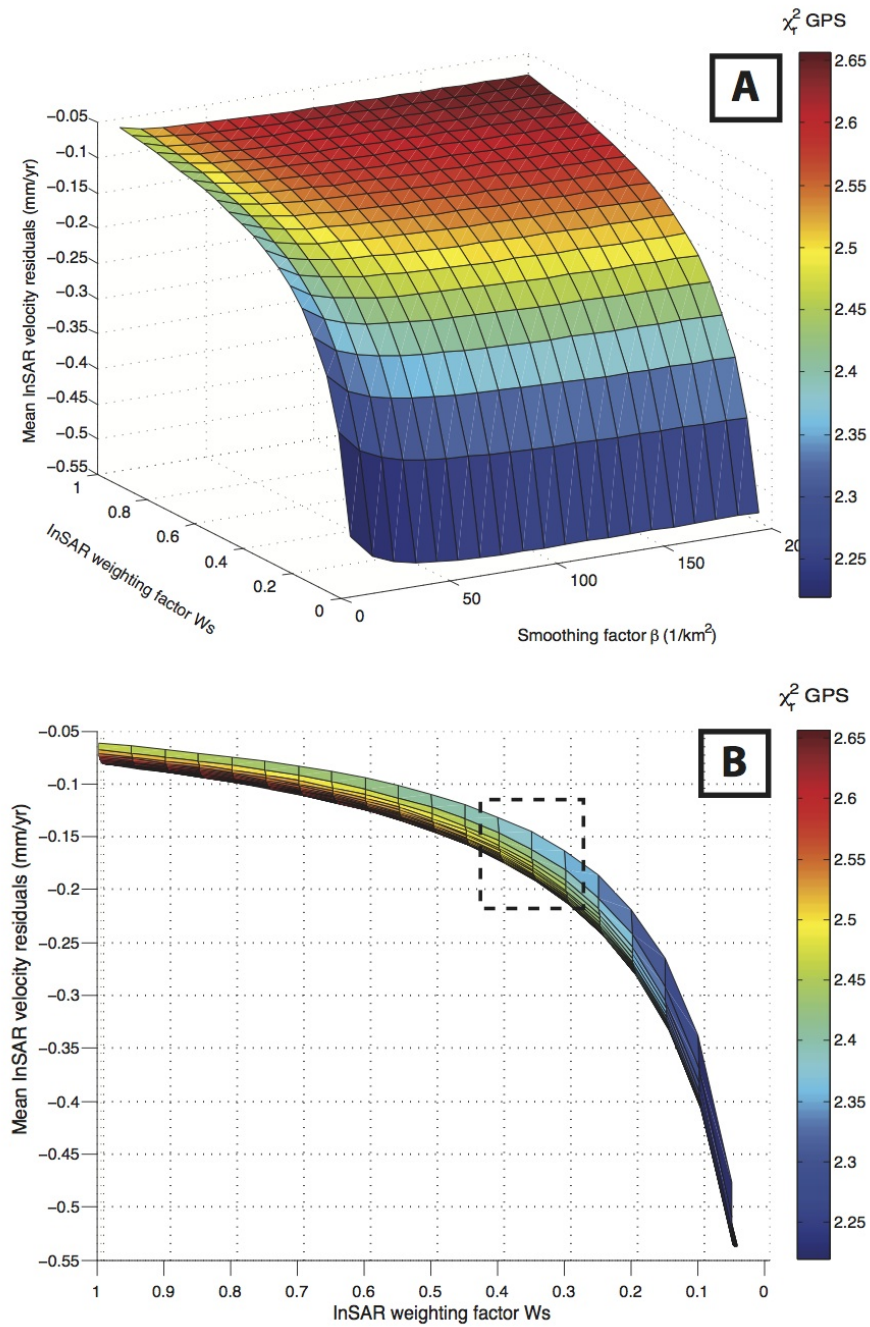
Figure 4.19: *Panel A: 3D trade-off between the GPS χ_r^2 and the MIVR for all values of Ws and β using the LLS approach; Panel B: lateral point of view of Panel A that exhibits the MIVR depending on Ws. The dashed box indicates the Ws values for which we want to examine the corresponding solutions to choose the final β value.*
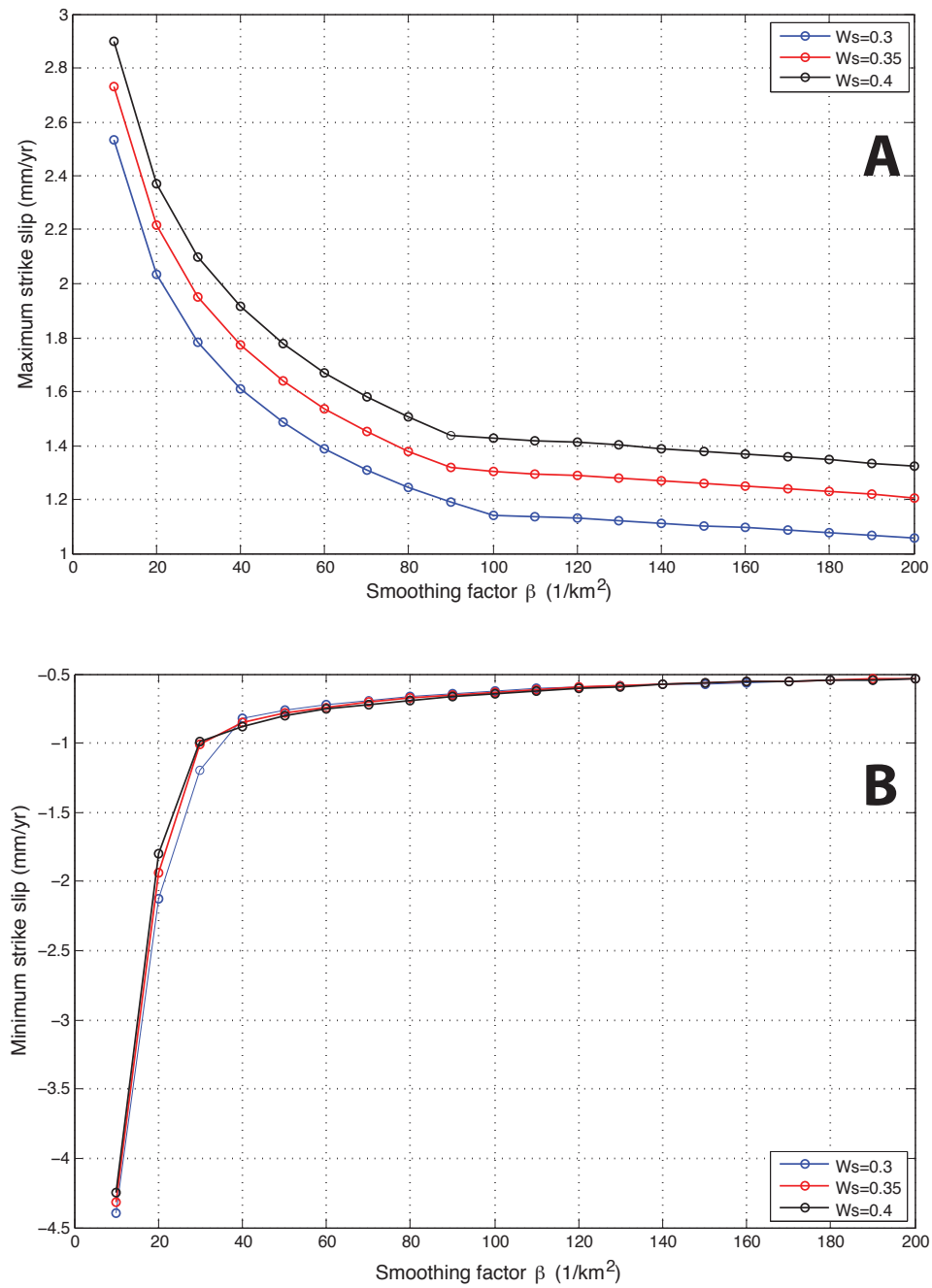
Figure 4.20: *Maximum (Panel A) and minimum (Panel B) values of the strike-slip component for the back-slip distribution as β changes, evaluated for the Ws factor = [0.3, 0.35, 0.4].*

Figure 4.21: *Same characteristics of Figure 4.14, but results obtained with the LLS method for the coupling distribution estimate with Ws = 0.35 and $\beta = 50\ km^{-2}$.*

Figure 4.22: *Imaging with a 3D view of the interseismic coupling distribution obtained with the LLS method setting Ws = 0.35 and $\beta = 50\ km^{-2}$; same map characteristics as in Fig. 4.18.*

4.6.1 Model resolution
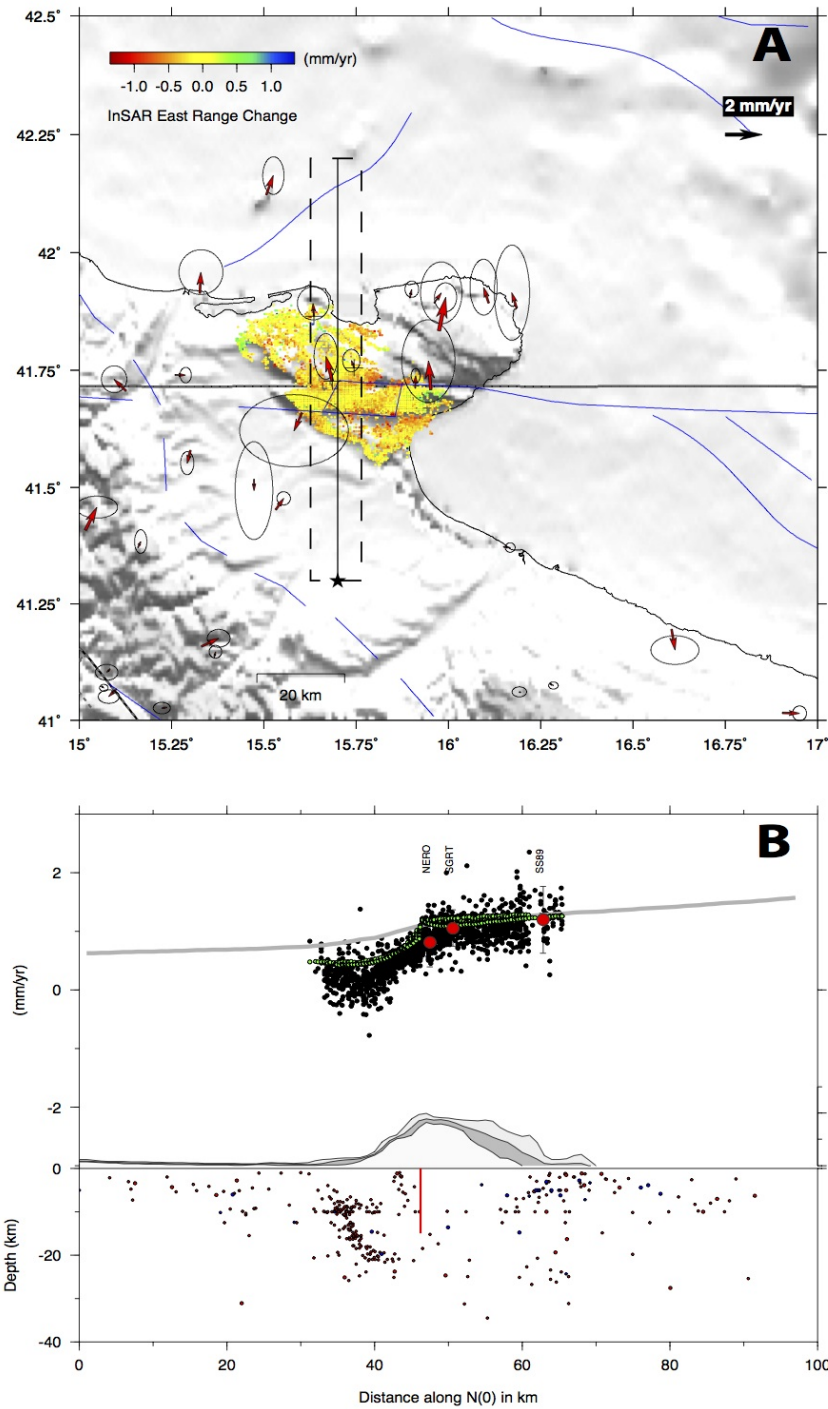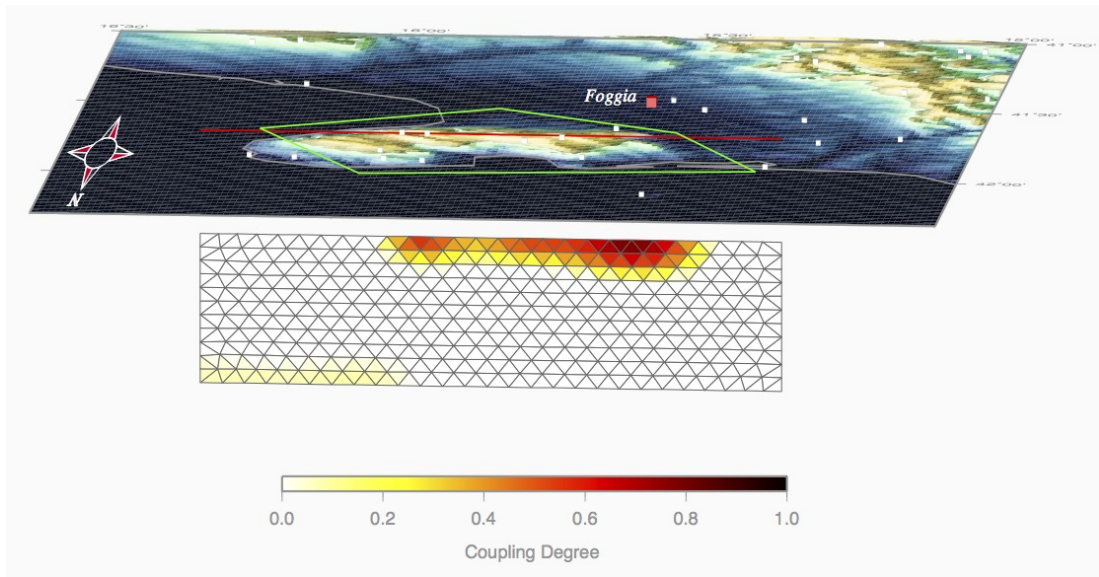
We have performed a last analysis to assess the reilability of used approaches and the ability of the available data to recover the coupling distribution in the fault plane with the chosen parameters. It consists on several checkerboard tests with different coupling pattern with 1mm/yr of right-lateral slip-rate, used to created synthetic GPS and InSAR velocity fields. Thus we have executed for each case an inversion of those synthetic data with both approaches, setting the same parameters defined in the previous sections. The original checkerboard patterns used and the recovered coupling of each test are shown in Appendix C.

We have defined a resolution criteria determining the resoved patches as a function of the magnitude of recovered slip. Following the method exposed by Métois *et al.* (2012), if the synthetic patch coupling is one, we consider resolved patches those ones where the recovered slip differs less than 30% from the initial value. Instead for synthetic patches with no coupling, we consider resolved those elements having less than 30% from the slip coupling value, as effect of the smoothing action. For twelve totaling test, we have then computed for each TDE the percentage of resolved times, and its worth to note that the most reliable areas should be characterized by at least a percentage of 60-70% ("percentage of resolution"). In fact looking at the recovered coupling patterns reported in Appendix C, we can see that the recovered slip distributions concern mainly the shallow part of the fault plane, without any recovered coupling pattern below of 15km of depth. However, using the criterium described above, we obtain a medium resolution of the order of 50% for the deeper portions of the fault, where the constant uncoupling allows to recover the original uncoupled portions. Thus we have decided to consider as resolved patches those

ones with higher resolution percentages.

Figure 4.23 shows our two final solutions of coupling distribution, with the countour lines of resolution corresponding to 60% and 80% and also the instrumental seismicity recorded at ± 2km of distrance from the fault plane. The figure highlights a very shallow resolution ($\sim$7km) for both inversion methods concerning patches located just below the area interested by InSAR points. We suppose that the small area recovered in depth may be an artifact due to the same coupling degree present in the synthetic patterns, and thus we do not consider it. The results just achieved for the coupling distribution estimates and about their reliability by means of checkerboard test allow us to affirm that the InSAR horizontal velocity we have considered may indicate probably a shallow interseismic coupling distribution for the Mattinata fault, characterized mainly by a low coupling degree for most of the fault surface.

4.7   Discussions

The interseismic coupling distributions for the Mattinata fault obtained with this analysis are the result of several assumptions that we had appointed step by step, and that may have generated anyhow some limits to this work. They concern mainly the reliability of the datasets used and the disputability of the applied kinematic approaches that model the data by means of simple approximations. However it is worth to say that a thorough kinematic study like this one for the Gargano promontory has never been performed before now.

In previous sections, we have noted that the sparse distribution of GPS sites has influenced not only the inaccurate modeling of the nearfield velocity in the Gargano promontory by the BM approach, but also the planar ramp estimation for the InSAR data. In fact the latter has been estimated using the maximum number as possible of GPS sites, that however, owning to their location, have provided just a limited information for the determination of the slope inclination (section 4.3.1). A denser distribution of GPS data might indicate a slightly different ramp, but it would allow to verify the reliability of the whole corrected InSAR dataset.

Moreover we have demonstrated, by means of the dislocation approach, (section 4.4) the inability of avalable GPS data to provide some indications about fault parameters for active fault system present in the region. Instead considering a wider GPS velocity field and a self-consistent kinematic approach, as the BM does, we have observed that the relative motion between Adria and Apulia plates could be accommodated by at least two fault systems, but the inadequate GPS coverage in the area does not allow us to perform a kinematically consistent study considering both (section 4.5.2). Certainly it is hard to solve for this problem, mainly because it is not possible to have a signal sampling in the surrounding area interested by the sea. However having some more data in some border regions, such as the apulian foredeep, could improve the present study with providing more kinematic constraints south of the Mattinata fault.

The InSAR velocities might provide some additional tectonic information. In fact, thanks
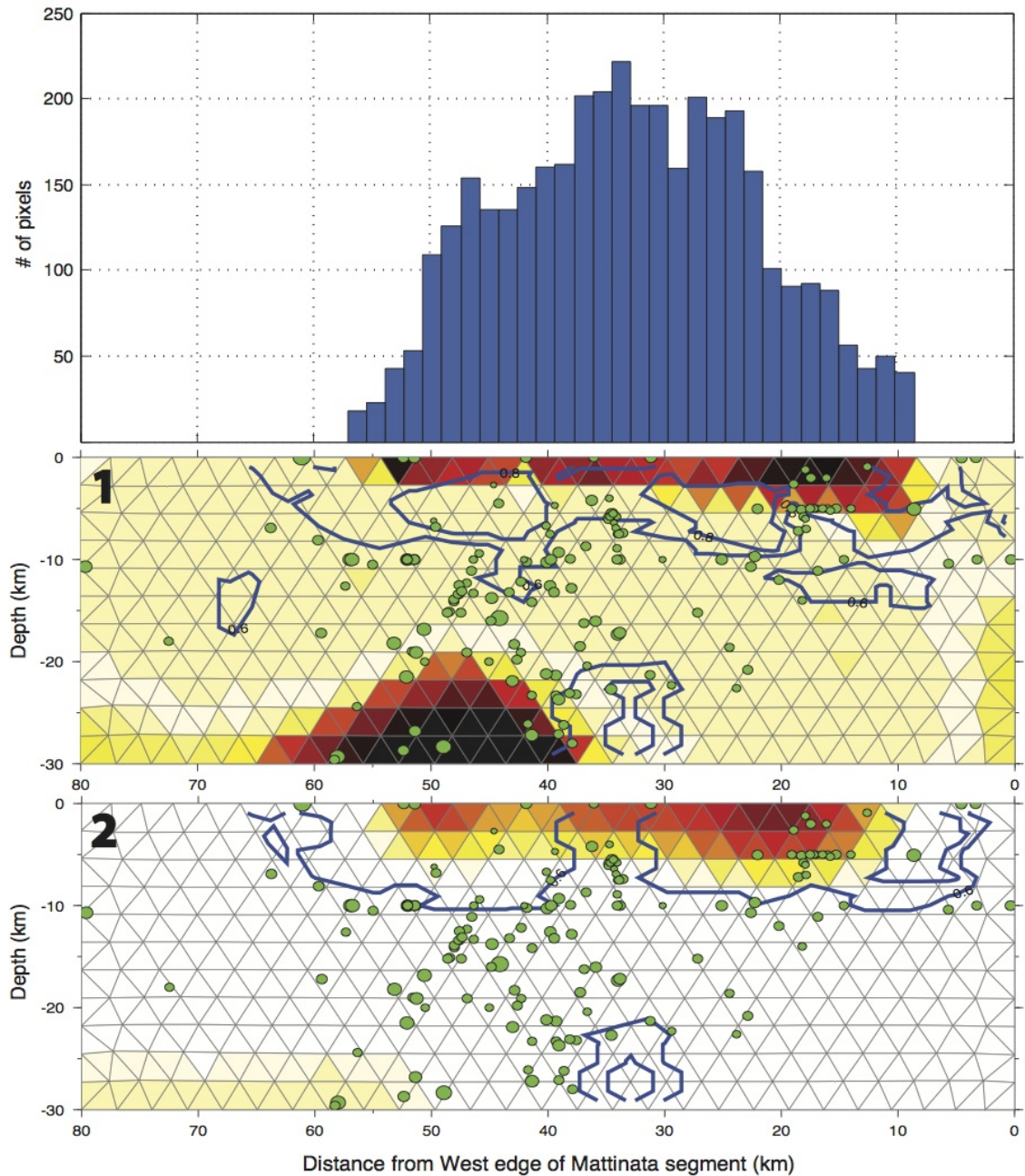
Figure 4.23: *Interseismic coupling distributions obtained with the LCA method (1) and the LLS solver (2). The instrumental seismicity (green dots) recorded at ± 2km of distrance from the plane, and the resolution contours for 60% and 80% (blu lines) are also shown. The upper panel is an histogram showing density of InSAR data points along the fault trace.*

to the pixel density and coherence of the available InSAR datasets in ascending and

descending tracks (section 2.4), Pezzo *et al.* (2014) have been able to combine them to extract the corresponding horizontal motion. During this combination they have assumed that the horizontal gradient measured should concern only the E-W direction, because of the very small inclination of satellite look-angle along the N-S line-of-sight. This assumption might be considered correct because InSAR data are referred to a local pixel and the horizontal velocities should be associated to a relative motion due to some tectonic origin. In particular for this region the N-S gradient of E-W deformation across the promontory was already detected by GPS data (Battaglia *et al.*, 2004) and this provides a further justification for the choice made. As proven by seismological (Milano *et al.*, 2005; Del Gaudio *et al.*, 2007) and geological (Piccardi, 1998; Tondi *et al.*, 2005) data, the Gargano promontory is interested by a compressional regime along the NW-SE direction (and thus extensional along the NE-SW one), that gives rise to the right-lateral shear along the E-W preferred direction, but also to extensional and compressive seismic events occurring on NE-SW and NW-SE oriented faults, respectively (Milano *et al.*, 2005; Pondrelli *et al.*, 2006; Del Gaudio *et al.*, 2007). This particular framework should produce in addition not only a variation for the E-W velocity components, but also variations for the N-S ones, that are however undetected owing to the sparse GPS network. Considering the residuals obtained for the InSAR velocities with the dislocation and the BM approaches (Figures 4.10, 4.21, 4.17) we observe a constant misfit mainly south of the fault, that is not consistent with a classical velocity gradient produced by a right-lateral strike slilp fault (Segall, 2010). To explain this misfit we have considered two principal causes:

1. an hidden gradient of the North velocity components due to some active dipping faults; however this possibility may be valid only if the North velocity gradient is of the order of 2 mm/yr, since the sensibility of the satellite along the North is less than a quarter of that one along the East direction. Nevertheless this hypothesis cannot be verified because of the completely lack of any GPS measurements in this specific area.

2. an asymmetric interseismic deformation around strike-slip faults has been documented for the major vertical fault-systems, that has been attributed to an elasticity contrast across the fault, due to the juxtaposition of different materials (Lisowski *et al.*, 1991; Le Pichon *et al.*, 2005; Jolivet *et al.*, 2008), or to the substrate viscosity contrasts (Malservisi *et al.*, 2001; Lundgren *et al.*, 2009; Vaghri & Hearn, 2012). Thus, our modeling approaches, assuming an elastic isotropic and homogeneus medium, may be too simple to model that signal.

However the first-order modeling of the horizontal InSAR velocities using both kinematic approaches is acceptable, also for the low residuals found. Moreover the contribution of InSAR velocities within kinematic studies may be very important, mainly for a tectonic framework such as this one for which few a-priori information are available. Firstly during the dislocation modeling InSAR data have shown their great ability to detect the fault position accommodating the velocity gradient and indicating the Mattinata fault as a principal structure. This result has provided a fondamental constraint further

applied in the BM analysis that depends strictly on the definition of the fault position. This starting-point in the BM inversions has allowed us to detect a mismatch between the observed velocity gradient by geodetic data and the modeled relative velocity corresponding to differential rotation of Adria and Apulia blocks. Since we have obtained rotational poles quite in agreement with those proposed in other works, we infer that within this plate boundary more than one fault system accommodating the relative motion should be present. In fact the great quantity of recorded seismicity offshore north of the Gargano might suggest a likely candidate, that we have tried to verify with a BM test, without obtaining any result.

The second important result achieved using InSAR data consists of the detection of the interseismic coupling degree for the Mattinata fault, testing our two different inversion methods for the BM approach. The accordant outcome from both methods consists mainly in a shallow pattern of coupling degree just below the InSAR data frame and with a low coupling degree for most of the fault surface. We have verified the resolution ability of our datasets for the coupling pattern by means of several checkerboard tests, for which we can consider as resolved just the first 5-7 km of depth below the InSAR frame. In fact from the performed resolution tests we have observed that the shallow aperities are recovered better along strike than along depth and moreover locked asperities at depth have never been recovered. This is clearly due to the inability of geodetic data to recover slip patterns in depth, perhaps because of the small InSAR frame that may be too small to be influenced by deep asperities. However the shallow resolution obtained for the coupling distribution allows us to affirm that the horizontal InSAR data may be explained by a shallow coupling pattern, but using these datasets we are not absolutely able to verify any presence of deep asperities.

Conclusions

In this thesis we have applied kinematic models using geodetic data to evaluate how the interseismic deformation is occurring in two Italian regions: the Alto Tiberina Fault (ATF) in the Umbria-Marche Apennines, and the Mattinata Fault in the Gargano promontory. We have used GPS velocities obtained from several operating networks in the Euro-Mediterranean regions. We have considered also horizontal InSAR velocities in East-West direction from ERS and ENVISAT satellites provided by Pezzo *et al.* (2014) concerning the Gargano promontory. These two target areas belong to different tectonic framework: in the first case we have a purely extensional deformation rate of almost 3 mm/yr along NE-SW direction and in the second one a right-lateral E-W shear zone of 1 mm/yr of deformation rate along the N-S direction. The aim of this thesis concerns the application of kinematic approaches, i.e. Block Modeling (BM) and Dislocation Modeling (DM), using joinlty (if possible) GPS and InSAR datasets, in order to assess how the interseismic deformation is accommodated in each specific region. In particular our analysis has concerned the estimation of kinematically consistent long-term slip rates and moreover the detection of the interseismic coupling distribution for the considered faults.

In particular for the ATF fault, thanks to the lately improvement of the local GPS network, we have demonstrated that the extensional rate measured by GPS velocities should be accommodated by at least two fault-systems, that are in this case the east-dipping low-angle normal-faults (LANFs), which the ATF belongs to, and the high-angle west-dipping normal-faults, in which the Gubbio fault (GuF) is part of it. This result highlights the active tectonic role of the ATF within an extensional context, where LANFs may be considered by the "Andersonian" theory as averse to faulting. However the recent activity of ATF has been suggested by several geological and seismological studies (e.g. Collettini, 2002; Chiaraluce *et al.*, 2007; Mirabella *et al.*, 2011) inferring at least a partial detachment of the fault. Thus we have used the BM approach also to evaluate the coupling degree distribution for the ATF considered fistly a planar surface meshed with triangular patches. Using this first approximation for the ATF surface we have demonstrated that the observed velocity filed is better explained by a varied coupling distribution. Then considering a more complicated surface, using the recent 3D reconstruction of the ATF provided by Mirabella *et al.* (2011), we observe instead that, with same GPS residuals, the coupling distribution slightly changes. In particular we obtain creeping behavior for few patches characterized by higher inclination. Thus, thanks to the availability of geometric features for the ATF, we have been able to observe a more realistic coupling distribution, that would not have been possible using a simple planar fault. Moreover this particular

coupling distribution shows a good correlation with the relocated microseismicity (Chiaraluce *et al.*, 2007) that is usually attributed to aseismic creeping behavior (Rubin *et al.*, 1999; Vergne *et al.*, 2001). Finally, performing a resolution analysis by menas of several checkerboard tests, we found that our coupling distribution is well resolved mostly for portions located below the GPS sites, giving reliability to a portion of the shallower asperity and to some creeping areas in depth.

As regards instead the Gargano promontory, our analysis has highlighted the important contribution that InSAR velocities may apport to understand the occurring deformation across a specific fault. The Gargano is inserted in a complicated seismo-tectonic framework generated by the relative movement of Adria and Apulia plates (Doglioni *et al.*, 1994). The deformation occurring in this region is widespread in the central Adriatic, observing numerous active fault systems (Brankman & Aydin, 2004; Ridente & Trincardi, 2006) and a diffuse seismicity onshore and offshore the promontory (Console *et al.*, 1993; Pondrelli *et al.*, 2006; Del Gaudio *et al.*, 2007). In this case we do not have any well-defined fault boundary between the two plates, and we have tried to evaluate which deformation is occurring in the Gargano promontory, modeling the measured velocities by the two available geodetic techniques. To have comparable GPS and InSAR velocities, we have anchored the latter to the same well-defined terrestrial reference frame of the GPS velocity field, estimating a planar signal (as known as "ramp"), that allows also to correct InSAR data of some orbital effects not completely removed during the processing phase. The InSAR velocity field corrected of the ramp shows a coherent velocity variation of the East-West component along the North-South direction. Thus we have performed a DM approach using jointly GPS and InSAR data, to evaluate which fault system may better reproduce the observed velocities. We have found that the most contribution to recover the optimal fault parameters has been provided by InSAR data, mostly because of the sparsity of GPS stations in the considered region. The indicated fault by InSAR measurements by the DM analysis corresponds exactly to the Mattinata fault, with a shallow locking depth. This result has been subsequentely used within the BM approach for the block geometry definition, in order to insert the corrected InSAR velocities within a wider kinematic frame. Using the BM approach, we have found that GPS and InSAR velocities close to the Mattinata fault are over-estimated by a simple block-model in which an E-W fault system passing through the Mattinata fault is assumed to be the only plate boundary between Adria and Apulia. This outcome may be interpreted as a proof of the widespread deformation accommodated in the central Adriatic, that we cannot take into account within the BM approach, because of the inadequate GPS coverage in the area. However, we have estimated as well the intersiemic coupling distribution for the Mattinata fault giving more importance to InSAR data with respect to GPS ones, in order to detect as better as possible the coupling pattern. The final solution shows a very shallow coupling distribution, that is resolved by the available data after a resolution analysis performed with several checkerboard tests.

The achievements of this thesis do not concern only the geophysical results obtained in each specific study, but they regard also the used methods that have allowed to perform the analysis. In particular we have modified the used BM modeling code in order to con-

straint the back-slip distribution to be consistent with the kinematics of the region (that is not considered in the original code). In each study we have estimated the coupling distribution using both methods, and the second method has provided better (for the ATF) or comparable (for the Mattinata fault) solutions in both cases.

Moreover the joint use of GPS and InSAR data is a strong approach to study in detail the deformation occurring across fault systems. In particular for the Mattinata fault, we have been able to define a possible plate boundary between Adria and Apulia plates only thanks to the InSAR velocities. The dense and well-distributed measurements provided by the InSAR technique are an important tool to observe tectonic deformation at short wavelength that instead GPS data could never provide.

In light of this consideration, we suppose that a possible future developement to better understand the occurring deformation across the Umbria-Marche Apennines may consist with a possible integration of InSAR velocity datasets within our BM analysis. Moreover it may be appropriate to compare also the coupling distribution estimates for the ATF and the Mattinata fault, with further information of different nature (e.g. rheological, seismological), in order to validate the final solutions found.

Appendix A

Detailed parametric representation of the BM approach

Generalization of the BM approach for GPS data

The final generalization of the forward problem considering all the constrains is given by:

$$
\begin{bmatrix}
\mathbf{V_I} \\
\mathbf{s_{obs}} \\
0 \\
0
\end{bmatrix}
=
\begin{bmatrix}
\mathbf{P_V G_B} - \mathbf{G_0 P_F P_V G_{B\Delta V}} & -\mathbf{G_T} & \mathbf{G_{\dot{\epsilon}}} \\
\mathbf{P_{Fs} P_{Vs} G_{B\Delta Vs}} & 0 & 0 \\
0 & \mathbf{L_T} & 0 \\
0 & \mathbf{B_T} & 0
\end{bmatrix}
\begin{bmatrix}
\mathbf{\Omega} \\
\mathbf{t} \\
\dot{\epsilon}
\end{bmatrix}
\tag{A.1}
$$

where $\mathbf{s_{obs}}$ are the apriori long-term fault slip rates, $\mathbf{L_T}$ is the Laplacian operator that estimates the second derivative of the TDE slip distribution (Maerten *et al.*, 2005) to be minimized during the inversion ($\nabla^2 \mathbf{t} = \mathbf{0}$) and $\mathbf{B_T}$ is a sparse matrix that applies the up- and/or down-dip zero slip constraints to TDEs. For this generalized linear relationship (eq. A.1), the authors of the code (Meade & Loveless, 2009) propose as a linear solver for the unknown parameters the weighted least-squares estimator (LLS):

$$
\begin{bmatrix}
\mathbf{\Omega_{est}} \\
\mathbf{t_{est}} \\
\dot{\epsilon}_{est}
\end{bmatrix}
= (\mathbf{G_G^T W G_G})^{-1} \mathbf{G_G^T W}
\begin{bmatrix}
\mathbf{V_I} \\
\mathbf{s_{obs}} \\
0 \\
0
\end{bmatrix}
\tag{A.2}
$$

where $\mathbf{G_G}$ is the generalized Jacobian (eq. A.1) that relates the observed velocity and bounds to the unknown parameters, and $\mathbf{W}$ is the data and boundary condition weighting matrix given by:

$$
\mathbf{W} =
\begin{bmatrix}
\mathbf{C_v}^{-1} & 0 & 0 & 0 \\
0 & \beta_1 \mathbf{C_s}^{-1} & 0 & 0 \\
0 & 0 & \beta_2 \mathbf{I} & 0 \\
0 & 0 & 0 & \beta_3 \mathbf{C_t}^{-1}
\end{bmatrix}
\tag{A.3}
$$

where $\mathbf{C_v}$ is the data covariance matrix, $\mathbf{C_s}$ is the a priori uniform slip rate covariance matrix, $\mathbf{I}$ is the identity matrix, $\mathbf{C_t}$ is the TDE boundary condition covariance matrix, and

β_i are the relative weights of the applied constraints. The a priori slip rates are weighted by β_1, the strength of the smoothing constraint on the TDE-slip distribution is given by β_2 (*smoothing factor*), and the weights of the a priori slip rates on TDEs are given by β_3.

Generalization of the BM approach considering jointly GPS and InSAR data

We have modified the original BM code of Meade & Loveless (2009), in order to invert also for InSAR velocities within the BM approach. Thus we have modified the generalized previous equations, with the aim to consider also InSAR velocities in the linear relationship (Eq. 1.12) between unknown parameters and observed velocities. Thus the Eq. A.1 of the generalized linear relationship become:

$$
\begin{bmatrix} \mathbf{V_I^G} \\ \mathbf{V_I^S} \\ \mathbf{s_{obs}} \\ 0 \\ 0 \end{bmatrix} = \begin{bmatrix} \mathbf{P_V G_B^G} - \mathbf{G_0^G P_F P_V G_{B\Delta V}^G} & -\mathbf{G_T^G} & \mathbf{G_{\dot{\epsilon}}^G} \\ \mathbf{P_V G_B^S} - \mathbf{G_0^S P_F P_V G_{B\Delta V}^S} & -\mathbf{G_T^S} & \mathbf{G_{\dot{\epsilon}}^S} \\ \mathbf{P_{Fs} P_{Vs} G_{B\Delta Vs}} & 0 & 0 \\ 0 & \mathbf{L_T} & 0 \\ 0 & \mathbf{B_T} & 0 \end{bmatrix} \begin{bmatrix} \boldsymbol{\Omega} \\ \mathbf{t} \\ \dot{\epsilon} \end{bmatrix} \tag{A.4}
$$

where the apices **G** and **S** indicate data and modeling matrices referred to GPS and InSAR velocities respectively. For the new generalized forward relation the linear solver of the weighted linear least-squares solution of Eq.A.2 is still valid. In this case we should consider as generalized Jacobian $\mathbf{G_G}$ the general matrix of the Eq. A.4 and the weighting matrix $\mathbf{W}$ become instead:

$$
\mathbf{W} = \begin{bmatrix} \mathbf{C_g}^{-1} & 0 & 0 & 0 & 0 \\ 0 & W_s \mathbf{C_s}^{-1} & 0 & 0 & 0 \\ 0 & 0 & \beta_1 \mathbf{C_s}^{-1} & 0 & 0 \\ 0 & 0 & 0 & \beta_2 \mathbf{I} & 0 \\ 0 & 0 & 0 & 0 & \beta_3 \mathbf{C_t}^{-1} \end{bmatrix} \tag{A.5}
$$

where $\mathbf{C_{g,s}}$ are the covariance matrices for GPS and InSAR data respectively and W_s is the InSAR weighting factor and it may vary from 0 to 1, and it is used to modulate the relative importance between GPS and InSAR data to the unknown parameter estimates. As reported by the Eq. A.5, W_s works down-weighting the InSAR covariance matrix, in order to reduce the InSAR data numerical influence on the final solution. The method used to choose the most appropriate W_s factor has been defined case by case.

Appendix B

ATF Checkerboard Tests

For each checkerboard coupling pattern we have inverted the corresponding synthetic velocity field using different smoothing factor β varied within the interval [0.01-0.3] km^{-2} with step of 0.01 km^{-2}. For each inversion we evaluate the GPS χ^2 of residual velocities and the precentage of resolved patches with respect to the original coupling pattern. The method used to define a resolved patch consists of a criteria determining the resoved patches as a function of the magnitude of recovered slip. Following the method exposed by Métois *et al.* (2012), if the synthetic patch coupling is one, we consider resolved patches those ones where the recovered slip differs less than 30% from the initial value. Instead for synthetic patches with no coupling, we consider as resolved those elements having less than 30% from the slip coupling value, as limit for the smoothing action.

Then, for each synthetic pattern, we have evaluated a trade-off curve (Figures B.1, B.2) for the GPS χ^2 as β changes, and we have chosen the optimal recovered solutions minimizing the χ^2. However to define a clear minimum for the χ^2 in each case, we have created two criteria based on the particular trade-off curve. In fact we have observed two principal patterns for the trade-off curves:

1. if χ^2 estimates for first β values are low, then χ^2 gets higher as β rises;

2. if χ^2 estimates for first β values are high, then χ^2 gets lower as β rises.

This particular behavior may be due to the various dimensions of original coupling patterns, that GPS data may recover by means of different contributions provided by the regularization. In particular the first group do not need a significant regularization contribution, and checkerboard patterns with small patches belong to this group (Figure B.1). Thus in this case we have chosen as optimal solution that one corresponding to the last absolute minimum for the χ^2 before a stable rising as β grows, and this criteria allows the recovered coupling distribution to be fairly regolarized. Instead to the second group belong all the other coupling patterns (Figures B.1, B.2), that have mostly bigger asperities, and for this reason they need a substantial regularization contribution to recover all the coupling features. Therefore in this case we consider as the optimal solution that one corresponding to the first absolute minimum for the χ^2, in which the regularization

has provided enough low residuals and at the same time a good percentage of resolved patches. The specific β values chosen for each synthetic case are shown in Figures B.1-B.2 indicated by red bars. Figures B.1-B.2 show also a further curve (green one) for each case overlapped to the χ^2 curves, indicating the trend of resolved patches percentage for each inversion, and we can observe that the chosen criteria allows to well recover most of coupling synthetic patterns.

The original and recovered coupling distributions for each synthetic pattern are shown below in Figure (to insert)
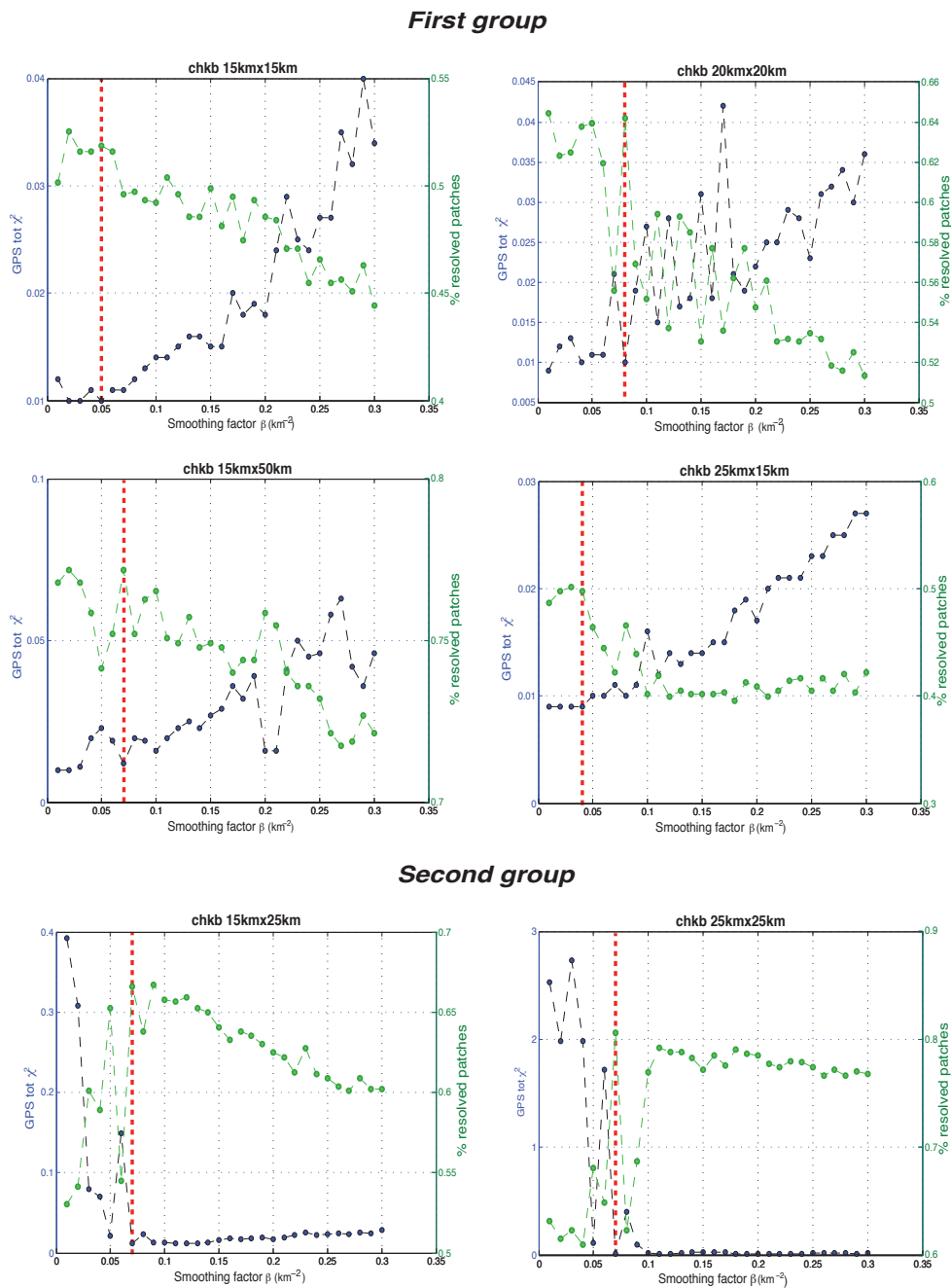
First group

Second group

Figure B.1: *Trade-off curves indicating the pattern of the GPS χ^2 (blu one) as β varies and corresponding percentage resolution (green one); red lines indicate the optimal β value chosen for each checkerboard test, following the criteria defined in Appendix B. The classification of the checkerboard tests in two groups is shown.*
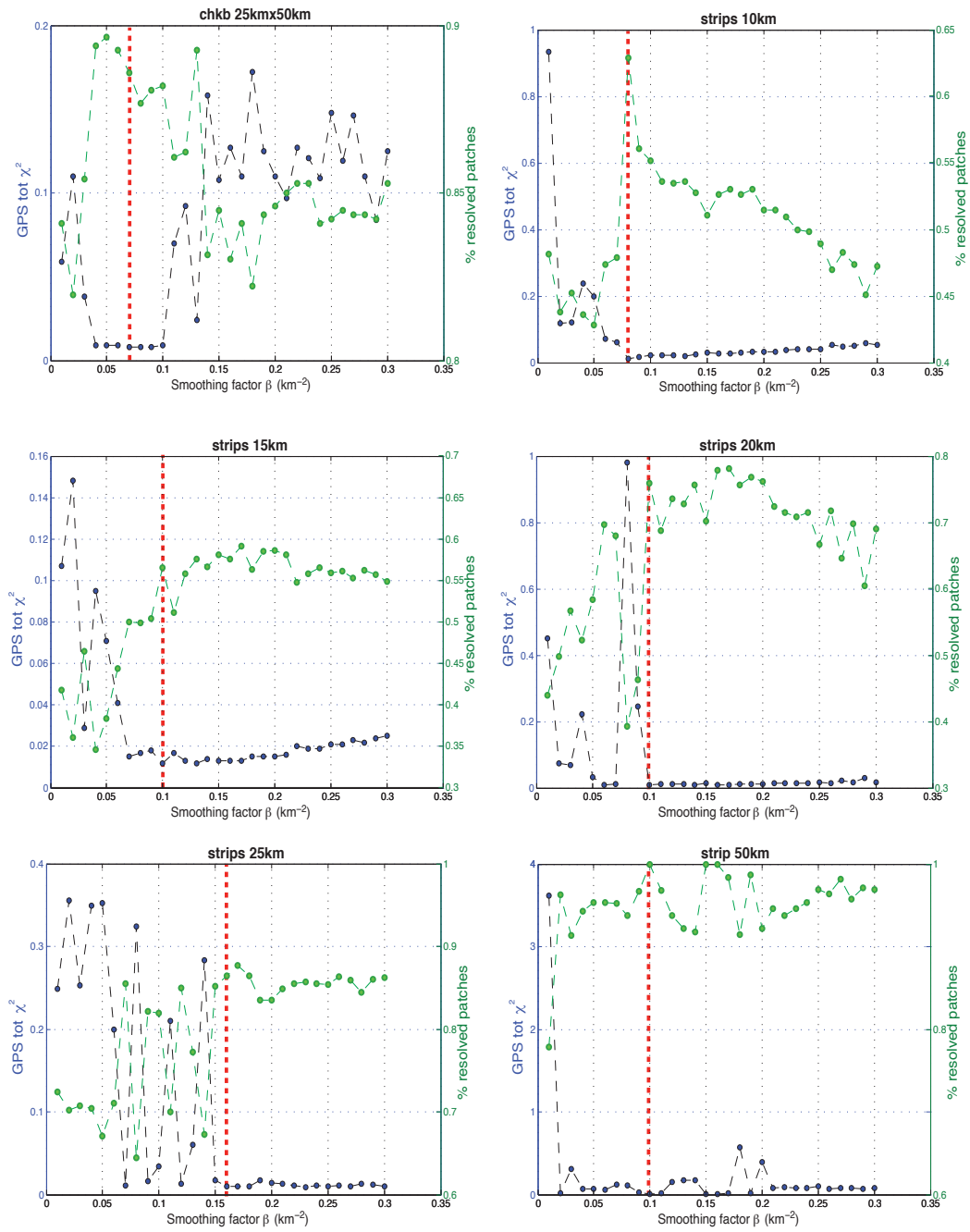
Second group

Figure B.2: *Same considerations as in Figure B.1.*
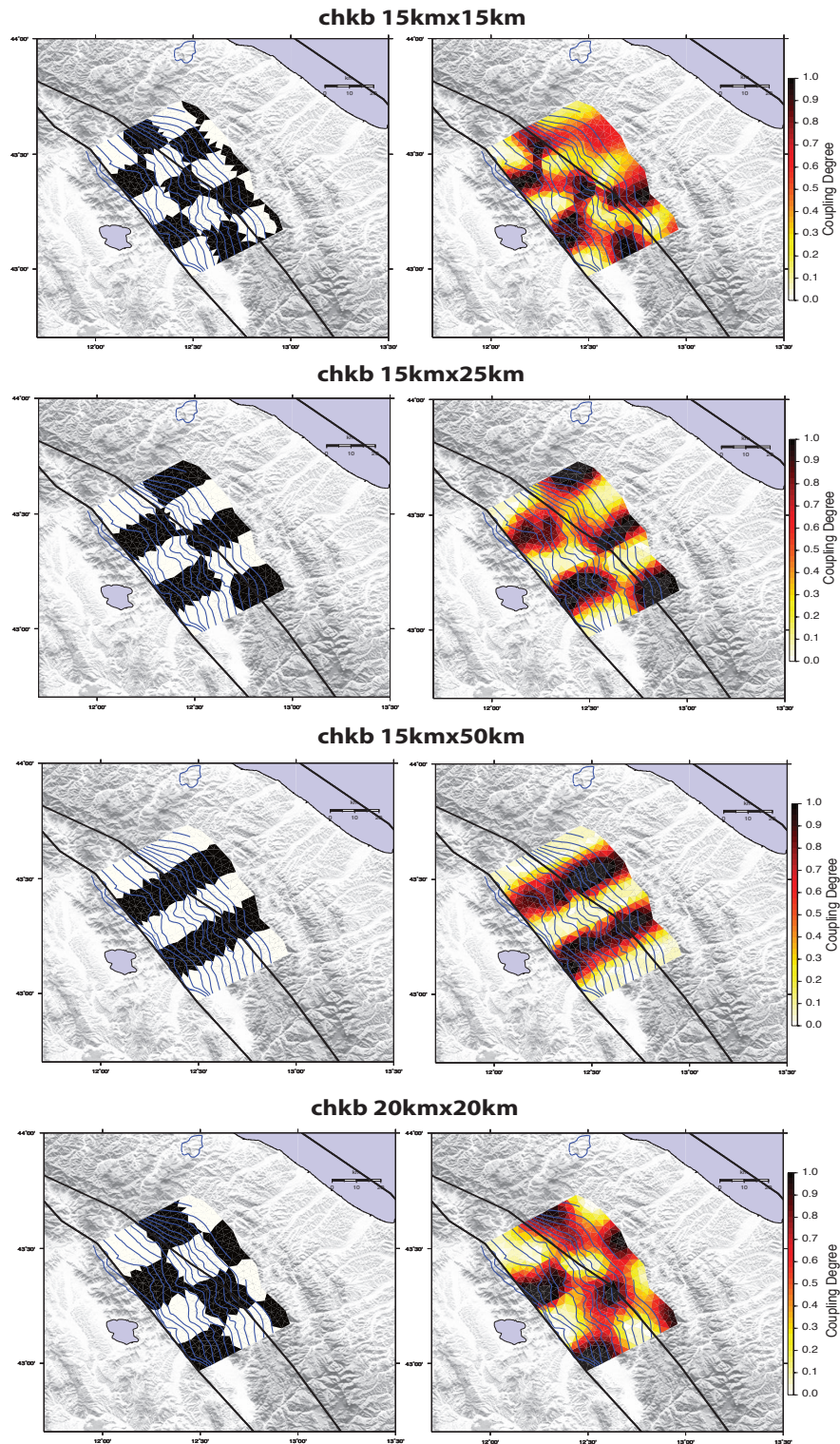
Figure B.3: *Checkerboard resolution tests performed with the LCA method for the ATF 3D surface using the β values shown in Figures* **??***.*

.

Figure B.4: *Same considerations as in Figure B.3.*
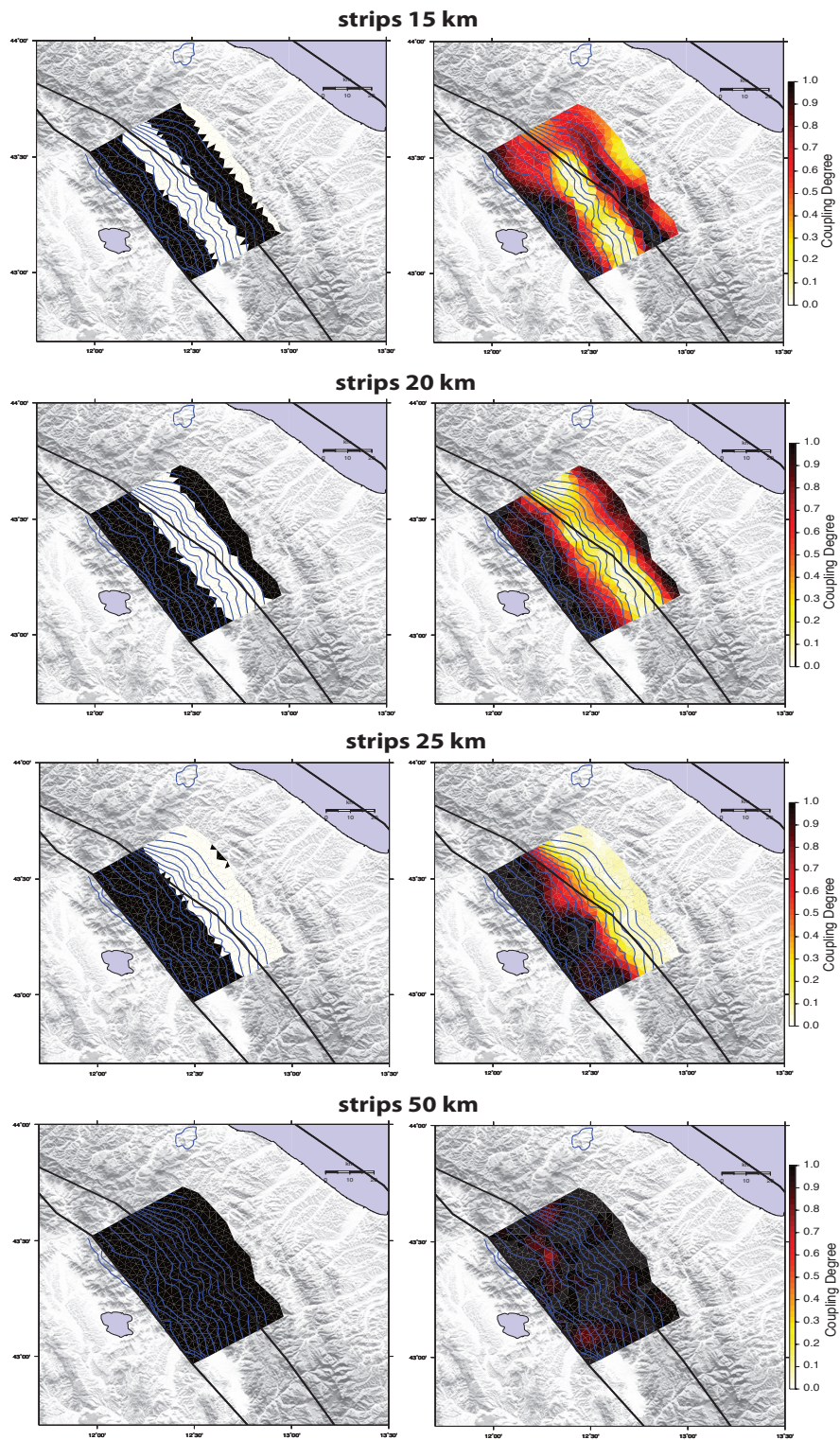
Figure B.5: *Same considerations as in Figure B.3.*

Appendix C

Checkerboard Resolution

LCA method
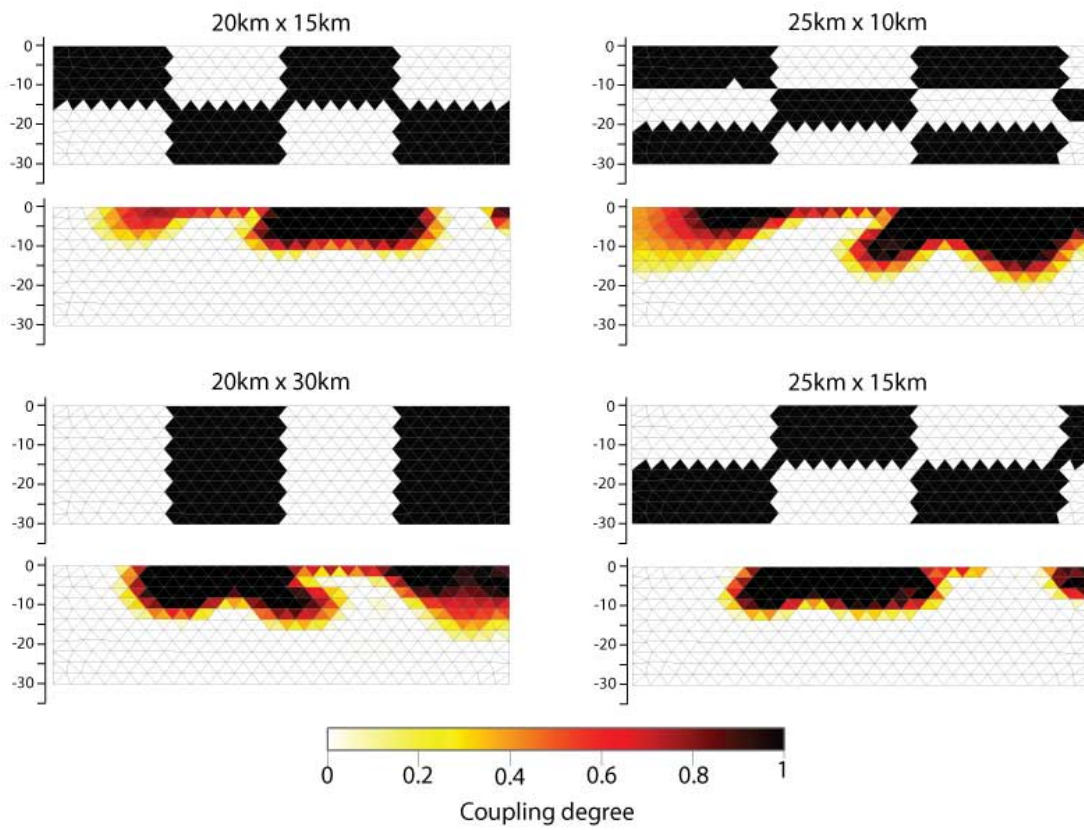
Figure C.1: *Checkerboard resolution tests performed with the LCA method using $\beta=0.1km^{-2}$ and Ws=0.65 and bounding the coupling degree to be within the interval [0,1].*
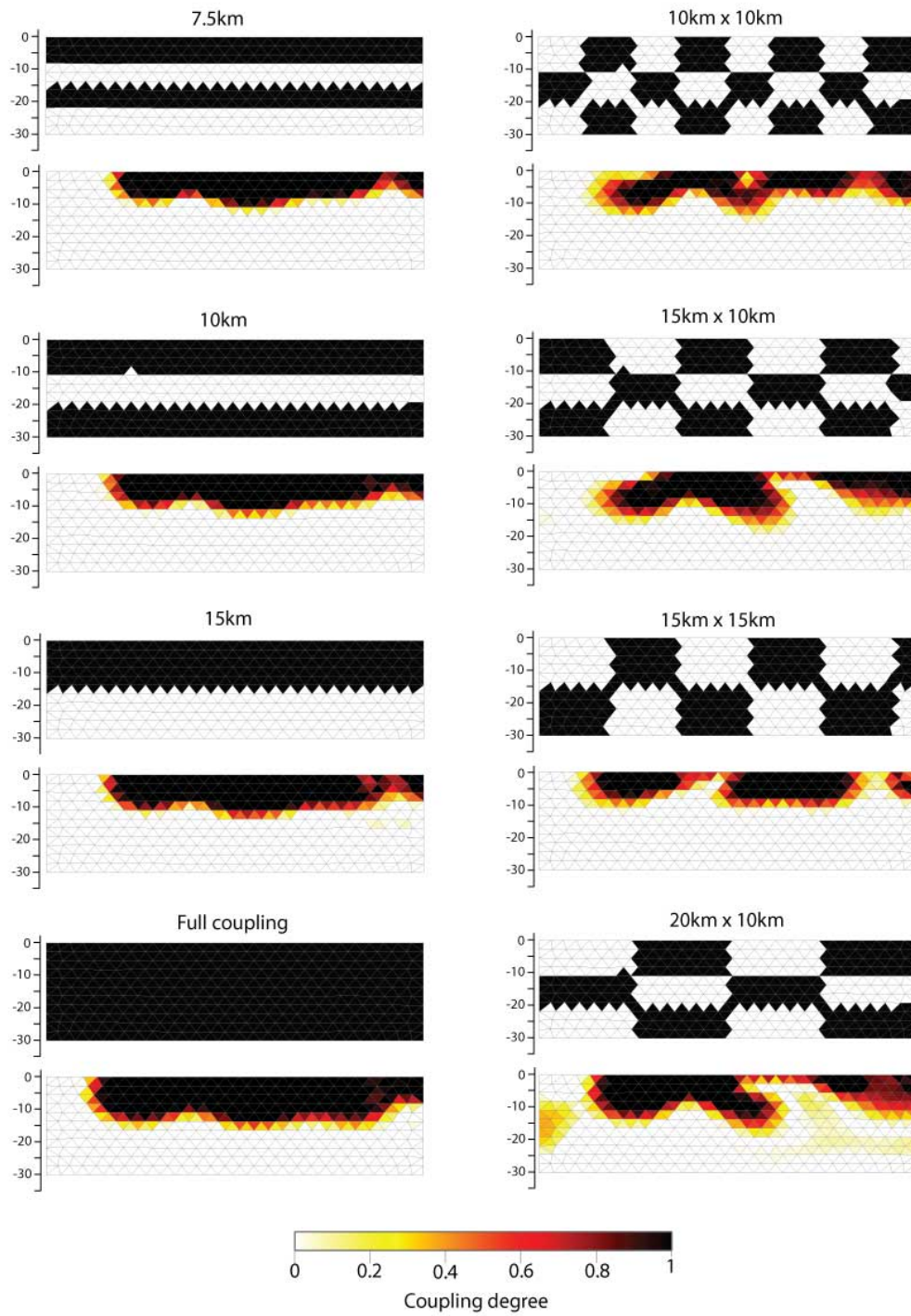
Figure C.2: *Same considerations as in Figure C.1.*

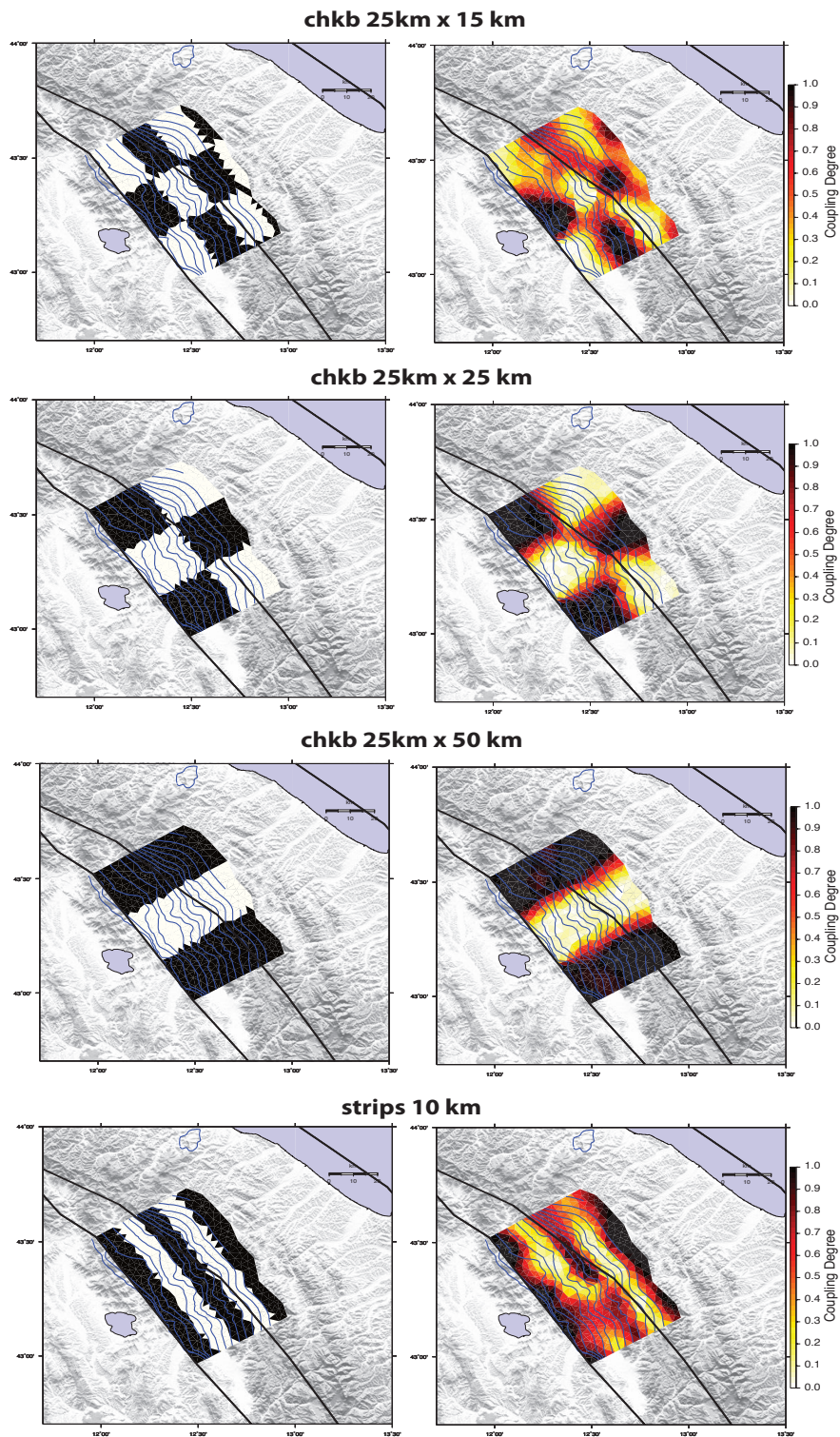# LLS method

Figure C.3: *Checkerboard resolution tests performed with the LLS method using β=50km^{-2} and Ws=0.35. The recovered coupling distributions span from negative values to quantities higher than 1 (i.e. back-slip greater than 1 mm/yr), which are indicated in the coupling patterns by dark red patches.*

Figure C.4: *Same considerations as in Figure C.3.*

References

Altamimi, Z, Collilieux, X, & Métivier, L. 2011. ITRF2008: An improved solution of the International Terrestrial Reference Frame. *Journal of Geodesy*, **85**(8), 457–473.
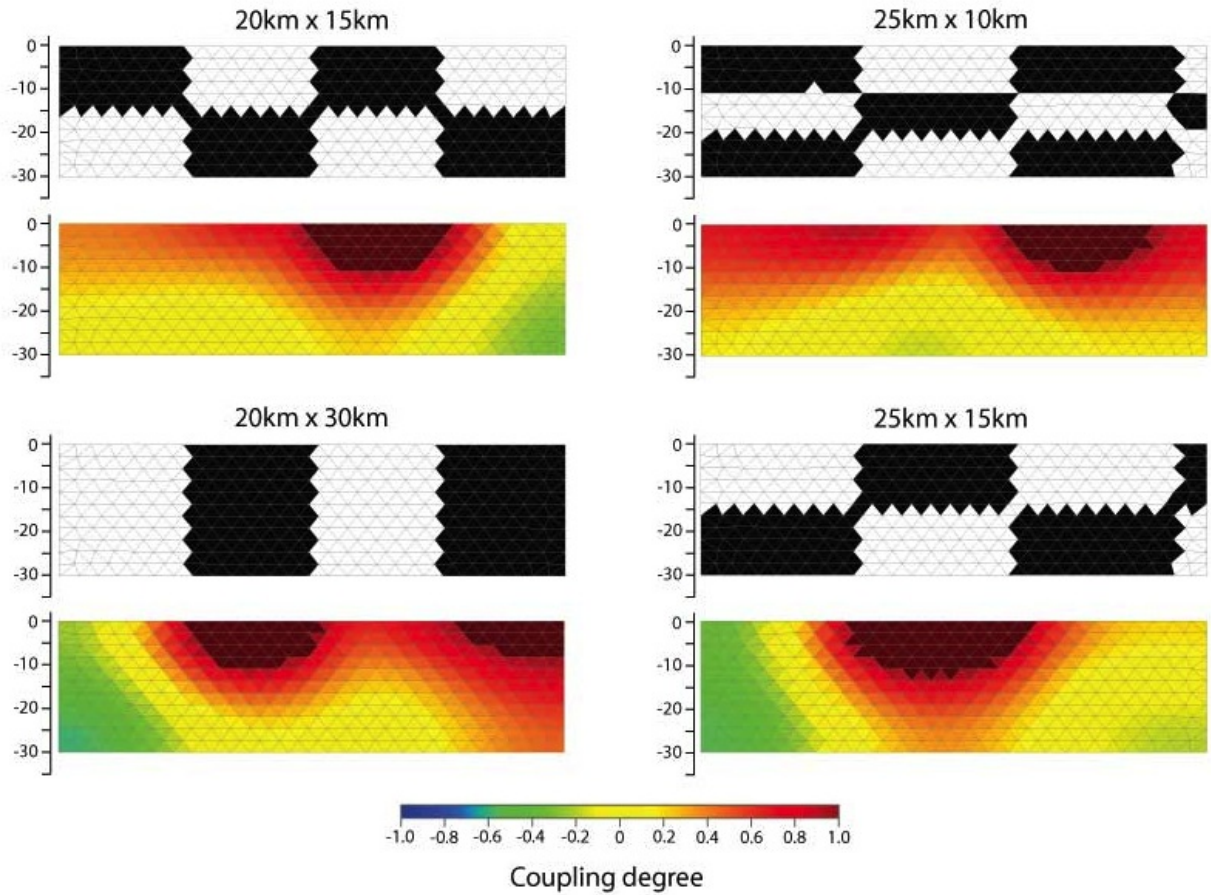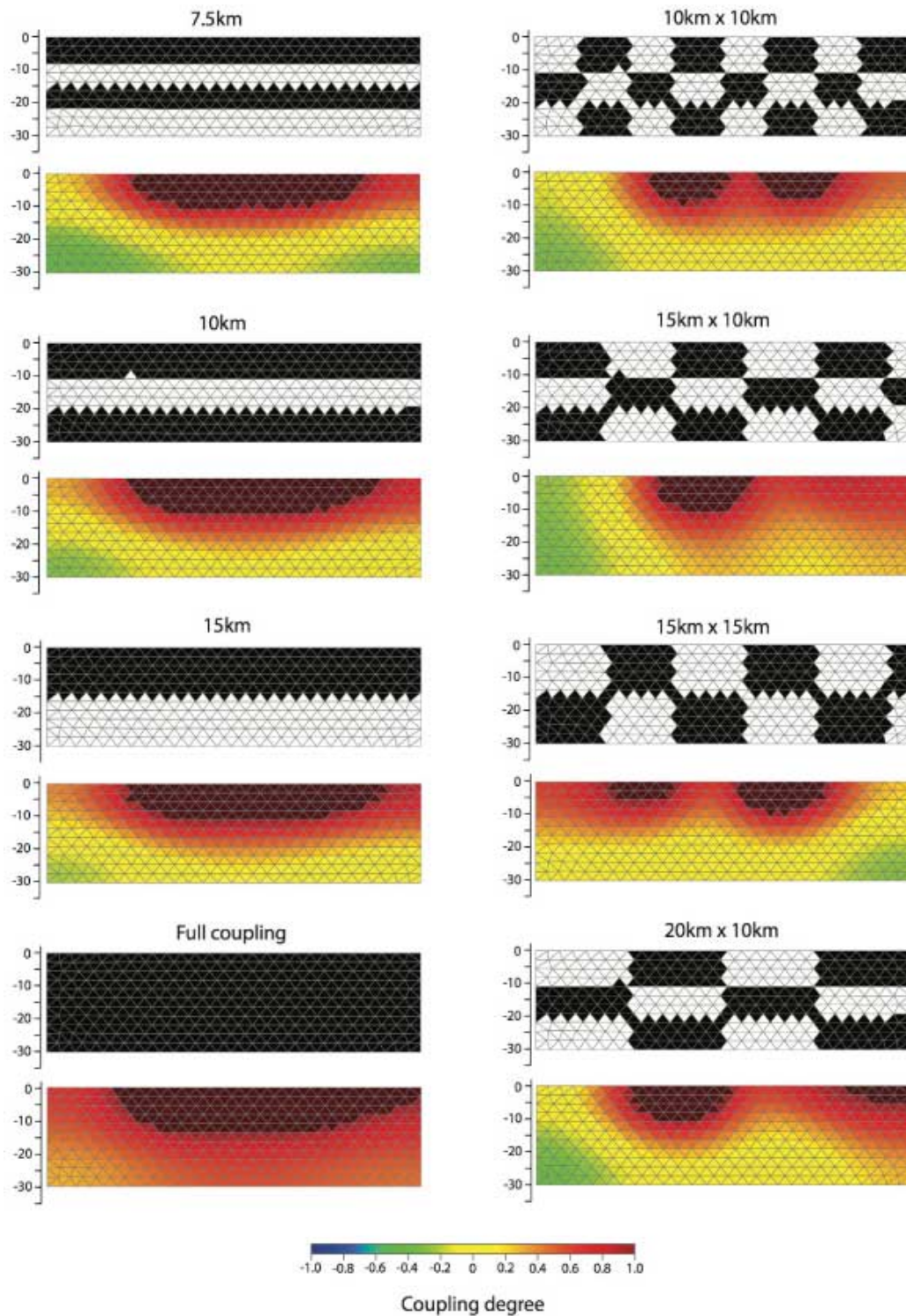
Alvarez, W. 1972. Rotation of the Corsica-Sardinia microplate. *Nature*, **248**, 309–314.

Amato, A., Azzara, R., Chiarabba, C., Cimini, G. B., Cocco, M., Di Bona, M., Margheriti, L., Mazza, S., Mele, F., Selvaggi, G., Basili, A., Boschi, E., Courboulex, F., Deschamps, A., Gaffet, S., Bittarelli, G., Chiaraluce, L., Piccinini, D., & Ripepe, M. 1998. The 1997 Umbria-Marche, Italy, Earthquake Sequence: A first look at the main shocks and aftershocks. *Geophysical Research Letters*, **25**(15), 2861–2864.

Anderson, Helen, & Jackson, James. 1987. Active tectonics of the Adriatic Region. *Geophysical Journal Research astr. Society*, **91**, 937–983.

Antonioli, Andrea, Piccinini, Davide, Chiaraluce, Lauro, & Cocco, Massimo. 2005. Fluid flow and seismicity pattern: Evidence from the 1997 Umbria-Marche (central Italy) seismic sequence. *Geophysical Research Letters*, **32**(10).

Árnadóttir, Thóra, & Segall, Paul. 1994. The 1989 Loma Prieta earthquake imaged from inversion of geodetic data. *Journal of geophysical research*, **99**(B11), 21835–21855.

Barchi, M., Minelli, G., & Pialli, G. 1998. The CROP-03 profile. A synthesis of results on deep structures of the northern Apennines. *Mem. Soc. Geol. It*, **52**, 383–400.

Battaglia, Maurizio, Murray, Mark H, Serpelloni, Enrico, & Burgmann, Roland. 2004. The Adriatic region : An independent microplate within the Africa- Eurasia collision zone. *Geophysical Research Letters*, **31**, 10–13.

Bennett, R A, Serpelloni, E, Hreinsdóttir, S, Brandon, M T, Buble, G, Basic, T, Casale, G, Cavaliere, A, Anzidei, M, Marjonovic, M, Minelli, G, Molli, G, & Montanari, A. 2012. Syn-convergent extension observed using the RETREAT GPS network, northern Apennines, Italy. *Journal of geophysical research*, **117**.

Berardino, P, Fornaro, G, Lanari, R, & Sansosti, E. 2002. A new algorithm for surface deformation monitoring based on small baseline differential interferograms. *IEEE Transactions on Geoscience and Remote Sensing*, **40**, 2375–2383.

Bertotti, G., Casolari, E., , & Picotti, V. 1999. The Gargano Promontory: A Neogene contractional belt within the Adriatic plate. *Terra Nova*, **11**, 168–173.

Billi, Andrea, Gambini, Roberto, Nicolai, Carlo, & Storti, Fabrizio. 2007. Neogene-Quaternary intraforeland transpression along a Mesozoic platform-basin margin: The Gargano fault system, Adria, Italy. *Geosphere*, **3**(1), 1–15.

Blewitt, G., & Lavallée, D. 2002. Effect of annual signals on geodetic velocity. *Journal of Geophysical Research*, **107**(B7), 2145.

Boehm, J., Niell, A., Tregoning, P., & Schuh, H. 2006. Global Mapping Function (GMF): A new empirical mapping function based on numerical weather model data. *Geophysical Research Letters*, **33**, L07304.

Boncio, Paolo, & Lavecchia, Giusy. 2000a. A geological model for the Colfiorito earthquakes (September-October 1997, central Italy). *Journal of Seismology*, **4**(October 1997), 345–356.

Boncio, Paolo, & Lavecchia, Giusy. 2000b. A structural model for active extension in Central Italy. *Journal of Geodynamics*, **29**, 233–244.

Boncio, Paolo, Lavecchia, Giuseppina, Milana, Giuliano, & Rozzi, Barbara. 2004. Seismogenesis in Central Apennines, Italy: an integrated analysis of minor earthquake sequences and structural data in the Amatrice-Campotosto area. *Annals of Geophysics*, **47**(6), 1723–1742.

Boschi, E., Guidoboni, E., Ferrari, G., Valensise, G., & Gasperini, P. 1999. Catalogue of strong Italian earthquakes from 461 bc to 1990. *Annali di Geofisica*, **42**.

Brankman, Charles M, & Aydin, Atilla. 2004. Uplift and contractional deformation along a segmented strike-slip fault system: the Gargano Promontory, southern Italy. *Journal of Structural Geology*, **26**(5), 807–824.

Brozzetti, Francesco. 1995. Stile deformativo della tettonica distensiva nell'Umbria Occidentale: l'esempio dei Massicci Massicci Mesozoici Perugini. *Studi Geologici Camerti*, **1**, 105–119.

Brozzetti, Francesco, Boncio, Paolo, Lavecchia, Giusy, & Pace, Bruno. 2009. Present activity and seismogenic potential of a low-angle normal fault system (Città di Castello, Italy): Constraints from surface geology, seismic reflection data and seismicity. *Tectonophysics*, **463**(1-4), 31–46.

Bürgmann, R., Schmidt, D, Nadeau, R M, D'Alessio, M, Fielding, E, Manaker, D, McEvilly, T V, & Murray, M H. 2000. Earthquake Potential Along the Northern Hayward Fault, California. *Science*, **289**(5482), 1178–1182.

Bürgmann, Roland, & Dresen, Georg. 2008. Rheology of the Lower Crust and Upper Mantle: Evidence from Rock Mechanics, Geodesy, and Field Observations. *Annual Review of Earth and Planetary Sciences*, **36**, 531–567.

Bürgmann, Roland, & Thatcher, Wayne. 2013. Space geodesy : A revolution in crustal deformation measurements of tectonic processes. *Geological Society of America*, **2500**(12), 1–34.

Bürgmann, Roland, Segall, Paul, Lisowski, Mike, & Svarc, Jerry. 1997. Postseismic strain following the 1989 Loma Prieta earthquake from GPS and leveling measurements. *Journal of geophysical research*, **102**(96), 4933–4955.

Calais, E., Nocquet, J. M., Jouanne, F., & Tardy, M. 2002. Current strain regime in the western Alps from continuous Global Positioning System measurements, 1996–2001. *Geology*, **7**, 651–654.

Casu, F, Manzo, M, & Lanari, R. 2006. A quantitative assessment of the SBAS algorithm performance for surface deformation retrieval from DInSAR data. *Remote Sensing and Environment*, **102**(3/4), 195–210.

Cattuto, C., Cencetti, C., Fisauli, M., & Gregori, L. 1995. I bacini pleistocenici di Anghiari e Sansepolcro nell'alta valle del Tevere. *Quaternario*, **8**, 119–128.

Celis, M., Dennis, E. J., & Tapia, R. A. 1985. *A trust region strategy for nonlinear equality constrained optimization in Numerical Optimization 1994*. SIAM, Philadelphia, PA. Pages 71–82.

Chiaraluce, L., Chiarabba, C., Collettini, C., Piccinini, D., & Cocco, M. 2007. Architecture and mechanics of an active low-angle normal fault: Alto Tiberina Fault, northern Apennines, Italy. *Journal of Geophysical Research*, **112**(B10), 1–22.

Ching, Kuo En, Rau, Ruey Juin, Johnson, Kaj M, Lee, Jian Cheng, & Hu, Jyr Ching. 2011. Presentday kinematics of active mountain building in Taiwan from GPS observations during 1995–2005. *Journal of geophysical research*, **116**(September), 1–22.

Chiodini, G., Cardellini, C., Amato, A., Boschi, E., Caliro, S., Frondini, F., & Ventura, G. 2004. Carbon dioxide Earth degassing and seismogenesis in central and southern Italy. *Geophysical Research Letters*, **31**(7), n/a–n/a.

Coleman, T. F., & Verma, A. 2001. A preconditioned conjugate gradient approach to linear equality constrained minimization. *Comput. Optim. Appl.*, **20**, 61–72.

Collettini, C., & Holdsworth, R.E. 2004. Fault zone weakening and character of slip along low-angle normal faults: insights from the Zuccale fault, Elba, Italy. *Journal of the Geological Society*, **161**(6), 1039–1051.

Collettini, C., Barchi, M.R., Chiaraluce, L., Mirabella, F., & Pucci, S. 2003. The Gubbio fault: can different methods give pictures of the same object? *Journal of Geodynamics*, **36**(1-2), 51–66.

Collettini, Cristiano. 2002. Hypothesis for the mechanics and seismic behaviour of low-angle normal faults : the example of the Altotiberina fault Northern Apennines. *Annals of Geophysics*, **45**(5), 683–698.

Collettini, Cristiano, Barchi, Massimiliano, Pauselli, Cristina, Federico, Costanzo, & Pialli, Giampaolo. 2000. Seismic expression of active extensional faults in northern Umbria (Central Italy). *Journal of Geodynamics*, **29**, 309 – 321.

Comninou, Maria, & Dundurs, J. 1975. The angular dislocation in a half space. *Journal of elasticity*, **5**(November), 203–216.

Console, R., Di Giovambattista, R., Favali, P., Presgrave, B. W., & Smiriglio, G. 1993. Seismicity of the Adriatic microplate. *Tectonophysics*, **218**, 343–354.

D'Agostino, N, Avallone, A, Cheloni, D, D'Anastasio, E, Mantenuto, S, & Selvaggi, G. 2008. Active tectonics of the Adriatic region from GPS and earthquake slip vectors. *Journal of geophysical research*, **113**, 1–19.

D'Agostino, N, Mantenuto, S, Anastasio, E D, Avallone, A, Barchi, M, Collettini, C, Radicioni, F, Stoppini, A, & Fastellini, G. 2009. Tectonophysics Contemporary crustal extension in the Umbria–Marche Apennines from regional CGPS networks and comparison between geodetic and seismic deformation. *Tectonophysics*, **476**(1-2), 3–12.

D'Alessio, M A, Johanson, I A, Burgmann, R, Schmidt, D A, & Murray, M H. 2005. Slicing up the San Francisco Bay Area : Block kinematics and fault slip rates from GPS-derived surface velocities. *Journal of geophysical research*, **110**, 1–19.

De Alteriis, G. 1995. Different foreland basins in Italy: Examples from the central and southern Adriatic Sea. *Tectonophysics*, **252**, 349–373.

Del Gaudio, V., Pierri, P., Frepoli, A., Calcagnile, G., Venisti, N., & Cimini, G.B. 2007. A critical revision of the seismicity of Northern Apulia (Adriatic microplate — Southern Italy) and implicationsfor the identification of seismogenic structures. *Tectonophysics*, **436**(1-4), 9–35.

Delle Donne, D., Piccardi, L., Odum, J., Stephenson, W., & Williams, R. 2007. High-resolution shallow reflection seismic image and surface evidence of the upper Tiber basin active faults (Northern Apennines, Italy). *Bollettino Società Geologica Italiana*, **126**, 323–331.

Deschamps, A., Scarpa, R., & Selvaggi, G. 1989. Analisi sismologica del settore settentrionale dell'Appennino umbro-marchigiano. *Proceedings VIII Nat. Congr. G.N.G.T.S., Rome*, **1**, 9–15.

Devoti, Roberto, Riguzzi, Federica, Cuffaro, Marco, & Doglioni, Carlo. 2008. New GPS constraints on the kinematics of the Apennines subduction. *Earth and Planetary Science Letters*, **273**(1-2), 163–174.

Di Bucci, Daniela, Ravaglia, Antonio, Seno, Silvio, Toscani, Giovanni, Fracassi, Umberto, & Valensise, Gianluca. 2006. Seismotectonics of the southern Apennines and Adriatic foreland: Insights on active regional E-W shear zones from analogue modeling. *Tectonics*, **25**(4), 1–21.

DISS, Working Group. 2010. *Database of Individual Seismogenic Sources (DISS), Version 3.1.1: A compilation of potential sources for earthquakes larger than M 5.5 in Italy and surrounding areas.* http://diss.rm.ingv.it/diss/, Istituto Nazionale di Geofisica e Vulcanologia.

Doglioni, Carlo, Mongelli, Francesco, & Pieri, Piero. 1994. The Puglia uplift (SE Italy): An anomaly in the foreland of the Apenninic subduction due to buckling of a thick continental lithosphere. *Tectonics*, **13**(5), 1309–1321.

Dong, D., Fang, P., Bock, Y., Webb, F., Prawirodirdjo, L., Kedar, S., & Jamason, P. 2006. Spatiotemporal filtering using principal component analysis and Karhunen-Loeve expansion approaches for regional GPS network analysis. *Journal of Geophysical Research*, **111**, B03405.

Dong, Danan, Herring, T, & King, Robert W. 1998. Estimating regional deformation from a combination of space and terrestrial geodetic data. *Journal of Geodesy*, **72**(4), 200–214.

Dong, Danan, Fang, P., Bock, Yehuda, Cheng, M., & Miyazaki, Shin'ichi. 2002. Anatomy of apparent seasonal variations from GPS-derived site position time series. *Journal of Geophysical Research*, **107**(B4), 2075.

Du, By Yijun, Aydin, Atilla, & Segall, Paul. 1992. Comparison of various inversion techniques as applied to the determination of a geophysical deformation model for the 1983 Borah Peak earthquake. *Bullettin of Seismological Society of America*, **82**(4), 1840–1866.

Elter, P., Giglia, G., Tongiorgi, M., & Trevisan, L. 1975. Tensional and compressional areas in the recent (Tortonian to present) evolution of north Apennines,. *Boll. Geofis. Teor. Appl*, **17**, 3–18.

Farr, T.G., Rosen, P.A., Caro, E., Crippen, R., Duren, R., Hensley, S., Kobrick, M., Paller, M., Rodriguez, E., Roth, L., Seal, D., Shaffer, S., Shimada, J., Umland, J., Werner, M., Oskin, M., Burbank, D., & Alsdorf, D. 2007. The Shuttle Radar Topography Mission. *Reviews of Geophysics*, **45**(RG2004).

Favali, P., Funiciello, R., & Pieri, P. 1993. An active margine across the Adriatic Sea (central Mediterranean Sea). *Tectonophysics*, **219**, 109–117.

Ferretti, Alessandro, Prati, Claudio, & Rocca, Fabio. 2001. Permanent scatterers in SAR interferometry. *IEEE Transactions on Geoscience and Remote Sensing*, **39**(1), 8–20.

Finetti, I., Bricchi, G., Del Ben, A., Pipan, M., & Xuan, Z. 1987. Geophysical study of the Adria Plate. *Mem. Soc. Geol. It*, **40**, 335–344.

Franco, A, Lasserre, C, Lyon-Caen, H, Kostoglodov, V, Molina, E, Guzman-Speziale, M, Monterosso, D, Robles, V, Figueroa, C, Amaya, W, Barrier, E, Chiquin, L, Moran, S, Flores, O, Romero, J, Santiago, J A, Manea, M, & Manea, V C. 2012. Fault kinematics in northern Central America and coupling along the subduction interface of the Cocos Plate, from GPS data in Chiapas (Mexico), Guatemala and El Salvador. *Geophysical Journal International*, 1–14.

Geuzaine, C., & Remacle, J.-F. 2009. Gmsh: a three-dimensional finite element mesh generator with built-in pre- and post-processing facilities. *International Journal for Numerical Methods in Engineering*, **79**(11), 1309–1331.

Goldstein, Richard M. 1995. Atmospheric Limitations to repeat-track radar interferometry. *Geophysical Research Letters*, **22**(18), 2517–2520.

Goldstein, Richard M, & Zebker, Howard A. 1987. Interferometric radar measurement of ocean surface currents. *Nature*, **328**, 707 – 709.

Harris, Ruth A, & Segall, Paul. 1987. Detection of a Locked Zone at Depth on the Parkfield , California, Segment of the San Andreas Fault. *Journal of geophysical research*, **92**, 7945–7962.

Herring, T, King, Robert W, & McClusky, Simon. 2010. *GAMIT Reference Manual, Release 10.4*. Massachussetts Institute of Technology, Cambridge, MA.

Hreinsdóttir, Sigrún, & Bennett, Richard A. 2010. Active aseismic creep on the Alto Tiberina low-angle normal fault, Italy. *Geology*.

Hunstad, I., Selvaggi, G., D'Agostino, N., England, P., Clarke, P., & Pierozzi, M. 2003. Geodetic strain in peninsular Italy between 1875 and 2001. *Geophysical Research Letters*, **30**(4), 1–4.

Hunstad, I., Pepe, a., Atzori, S., Tolomei, C., Salvi, S., & Lanari, R. 2009. Surface deformation in the Abruzzi region, Central Italy, from multitemporal DInSAR analysis. *Geophysical Journal International*, **178**(3), 1193–1197.

Ito, Takeo, Yoshioka, Shoichi, & Miyazaki, Shin'ichi. 1999. Interplate coupling in southwest Japan deduced from inversion analysis of GPS data. *Physics of the Earth and Planetary Interiors*, **115**(1), 17–34.

Jeyakumaran, M., Rudnicki, J. W., & Keer, L. M. 1992. MODELING SLIP ZONES WITH TRIANGULAR DISLOCATION ELEMENTS. *Bullettin of Seismological Society of America*, **82**(5), 2153–2169.

Johanson, Ingrid A, Fielding, Eric J, Rolandone, Frederique, & Bu, Roland. 2006. Coseismic and Postseismic Slip of the 2004 Parkfield Earthquake from Space-Geodetic Data. *Bullettin of Seismological Society of America*, **96**(4), 269–282.

Johnson, K M, & Segall, P. 2004. Viscoelastic earthquake cycle models with deep stress-driven creep along the San Andreas fault system. *Journal of geophysical research*, **109**, 1–19.

Johnson, Kaj M, & Fukuda, Jun. 2010. New methods for estimating the spatial distribution of locked asperities and stress driven interseismic creep on faults with application to the San Francisco Bay Area , California. *Journal of geophysical research*, **115**, 1–28.

Johnson, Kaj M, Hilley, George, & Burgmann, Roland. 2007. Influence of lithosphere viscosity structure on estimates of fault slip rate in the Mojave region of the San Andreas fault system. *Journal of Geophysical Research*, **112**(B07408).

Jolivet, Laurent, Faccenna, Claudio, Goffé, Bruno, Mattei, Massimo, Rossetti, Federico, Brunet, Christophe, Storti, Fabrizio, Funiciello, Renato, Cadet, Jean Paul, D'Agostino, Nicola, & Parra, Teddy. 1998. Midcrustal shear zones in postorogenic extension: Example from the northern Tyrrhenian Sea. *Journal of Geophysical Research: Solid Earth*, **103**(B6), 12123–12160.

Jolivet, R., Cattin, R., Chamot-Rooke, N., Lasserre, C., & Peltzer, G. 2008. Thin-plate modeling of interseismic deformation and asymmetry across the Altyn Tagh fault zone. *Geophysical Research Letters*, **35**(2), 1–5.

Kanda, Ravi V S, & Simons, Mark. 2010. An elastic plate model for interseismic deformation in subduction zones. *Journal of geophysical research*, **115**, 1–19.

Kaneko, Yoshihiro, Avouac, Jean-philippe, & Lapusta, Nadia. 2010. Towards inferring earthquake patterns from geodetic observations of interseismic coupling. *Nature Geoscience*, **3**(5), 363–369.

Lavecchia, Giusy, Boncio, Paolo, Brozzetti, Francesco, Stucchi, Massimiliano, & Leschiutta, Ilaria. 2002. New criteria for seismotectonic zoning in Central Italy: insights from the Umbria-Marche Apennines. *Bollettino Società Geologica Italiana*, **1**, 881–890.

Le Pichon, Xavier, Kreemer, Corné, & Chamot-Rooke, Nicolas. 2005. Asymmetry in elastic properties and the evolution of large continental strike-slip faults. *Journal of Geophysical Research*, **110**(B3405), 1–11.

Li, V. C., & Rice, J. R. 1987. Crustal deformation in great California earthquake cycles. *Journal of Geophysical Research*, **92**, 11533–11551.

Lisowski, M, Savage, J. C., & Prescott, W.H. 1991. The Velocity Field Along the San Andreas Fault in Central and Southern California. *Journal of geophysical research*, **96**, 8369–8389.

Lopez-Quiroz, P., Doin, M.-P., Tupin, F., Briole, P., & Nicholas, J.-M. 2009. Time series analysis of Mexico City subsidence constrained by radar interferometry. *Journal of Applied Geophysics*, **69**, 1–15.

Loveless, J P, & Meade, B J. 2011. Partitioning of localized and diffuse deformation in the Tibetan Plateau from joint inversions of geologic and geodetic observations TS AT. *Earth and Planetary Science Letters*, **303**(1-2), 11–24.

Loveless, John P, & Meade, Brendan J. 2010. Geodetic imaging of plate motions, slip rates, and partitioning of deformation in Japan. *Journal of geophysical research*, **115**, 1–35.

Lundgren, Paul, Hetland, Eric A., Liu, Zhen, & Fielding, Eric J. 2009. Southern San Andreas-San Jacinto fault system slip rates estimated from earthquake cycle models constrained by GPS and interferometric synthetic aperture radar observations. *Journal of Geophysical Research: Solid Earth*, **114**(B2), n/a–n/a.

Lyard, F, Lefevre, F, Letellier, T, & Francis, O. 2006. Modelling the global ocean tides: Modern insights from FES2004. *Ocean Dynam.*, **56**, 394–415.

Maerten, Frantz, Resor, Phillip, Pollard, David, & Maerten, Laurent. 2005. Inverting for slip on three-dimensional fault surfaces using angular dislocations. *Bullettin of Seismological Society of America*, **95**(5), 1654–1665.

Malservisi, R., Furlong, K. P., & Dixon, T. H. 2001. Influence of the earthquake cycle and lithospheric rheology on the dynamics of the Eastern California Shear Zone. *Geophysical Research Letters*, **28**(14), 2731–2734.

Manaker, D M, Calais, E, Freed, A M, Ali, S T, Przybylski, P, Mattioli, G, Jansma, P, Prépetit, C, & Chabalier, J B De. 2008. Interseismic Plate coupling and strain partitioning in the Northeastern Caribbean. *Geophysical Journal International*, **174**, 889–903.

Massonnet, Didier, & Feigl, Kurt L. 1995. Discrimination of geophysical phenomena in satellite radar interferograms. *Geophysical Research Letters*, **22**(12), 1537–1540.

McCaffrey, Robert. 2002. Crustal Block Rotations and Plate Coupling. *AGU Monograph*, 1–40.

McCaffrey, Robert. 2005. Block kinematics of the Pacific–North America plate boundary in the southwestern United States from inversion of GPS, seismological, and geologic data. *Journal of geophysical research*, **110**, 1–27.

McKenzie, Dan, & Jackson, James. 1983. The relationship between strain rates, crustal thickening, palaeomagnetism, finite strain and fault movements within a deforming zone. *Earth and Planetary Science Letters*, **65**(1), 182–202.

Meade, Brendan J. 2007a. Algorithms for the calculation of exact displacements, strains, and stresses for triangular dislocation elements in a uniform elastic half space. *Computers & Geosciences*, **33**, 1064–1075.

Meade, Brendan J. 2007b. Present-day kinematics at the India-Asia collision zone. *Geological Society of America*, **35**(1), 81–84.

Meade, Brendan J, & Hager, Bradford H. 2005. Block models of crustal motion in southern California constrained by GPS measurements. *Journal of geophysical research*, **110**, 1–19.

Meade, Brendan J, & Loveless, John P. 2009. Block Modeling with Connected Fault-Network Geometries and a Linear Elastic Coupling Estimator in Spherical Coordinates. *Bullettin of Seismological Society of America*, **99**(6), 3124–3139.

Menke, W. 1989. *Geophysical data analisis: discrete inverse theory.* Vol. 45. Academic Press, INC.

Métois, M, Socquet, A, & Vigny, C. 2012. Interseismic coupling, segmentation and mechanical behavior of the central Chile subduction zone. *Journal of geophysical research*, **117**, 1–16.

Milano, Girolamo, Di Giovambattista, Rita, & Ventura, Guido. 2005. Seismic constraints on the present-day kinematics of the Gargano foreland, Italy, at the transition zone between the southern and northern Apennine belts. *Geophysical Research Letters*, **32**(24), 1–4.

Miller, S. A., Collettini, C., Chiaraluce, L., Cocco, M., Barchi, M. R., & Kraus, J. B. 2004. Aftershocks driven by a high-pressure CO2 source at depth,. *Nature*, **427**, 724–727.

Mirabella, F., Brozzetti, F., Lupattelli, A., & Barchi, M. R. 2011. Tectonic evolution of a low-angle extensional fault system from restored cross-sections in the Northern Apennines (Italy). *Tectonics*, **30**(6), 1–23.

Mongelli, F., & Ricchetti, G. 1970. Heat flow along the Candelaro Fault - Gargano Headland (Italy). *Geothermics*, **2**(special issue), 450–458.

Morley, C.K. 1999. Marked along-strike variations in dip of normal faults-the Lokichar fault, N. Kenya rift: a possible cause for metamorphic core complexes. *Journal of Structural Geology*, **21**(5), 479 – 492.

Okada, Yoshimitsu. 1985. Surface deformation due to shear and tensile faults in a half-space. *Bullettin of Seismological Society of America*, **75**(4), 1135–1154.

Oldow, J.S., Ferranti, L., Lewis, D.S., Campbell, J.K., D'Argenio, B., Catalano, R., Pappone, G., Carmignani, L., Conti, P., & Aiken, C.L.V. 2002. Active fragmentation of Adria, the north African promontory, central Mediterranean orogen. *Geology*, **30**(9), 779–782.

Patacca, E., & Scandone, P. 2004. The 1627 Gargano earthquake (Southern Italy): Identification and characterization of the causative fault. *Journal of Seismology*, **8**, 259–273.

Pauselli, Cristina, Barchi, Massimiliano R., Federico, Costanzo, Magnani, M. Beatrice, & Minelli, Giorgio. 2006. The crustal structure of the northern apennines (Central Italy): An insight by the crop03 seismic line. *American Journal of Science*, **306**(6), 428–450.

Persson, Per-Olof, & Strang, Gilbert. 2004. A simple mesh generator in matlab. *SIAM Review*, **46**(2), 329–345.

Pezzo, Giuseppe, Tolomei, Cristiano, Atzori, Simone, Salvi, Stefano, & Serpelloni, Enrico. 2014. Present deformation of the Gargano promontory (Southern Italy) by multitemporal SAR interferometry analysis. *under revision.*

Pialli, G., Barchi, M., & Minelli, G. 1998. Results of the CROP03 Deep Seismic Reflection Profile. *Mem. Soc. Geol. It*, **52**, 657 pp.

Piccardi, L. 1998. Cinematica attuale, comportamento sismico, e sismologia storica della faglia attiva di Monte Sant'Angelo (Gargano, Italia): la possibile rottura superficiae del leggendario terremoto del 493 d.C. *Geogr. Fis. Din. Quant.*, **21**, 155–166.

Piccardi, L. 2005. Paleoseismic evidence of legendary earthquakes: The apparition of Archangel Michael at Monte Sant'Angelo (Italy). *Tectonophysics*, **408**, 113–128.

Piccinini, D., Cattaneo, M., Chiarabba, C., Chiaraluce, L., De Martin, M., Di Bona, M, Moretti, M., Selvaggi, G., Augliera, P., & Spallarossa, D. 2003. A microseismic study in a low seismicity area of Italy: the Città di Castello 2000-2001 experiment. *Annals of Geophysics*, **46**(6).

Pondrelli, S, Salimbeni, S, Ekstrom, G, Morelli, A, Gasperini, P, & Vannucci, G. 2006. The Italian CMT dataset from 1977 to the present. *Physics of the Earth and Planetary Interiors*, **159**, 286–303.

Reilinger, Robert, McClusky, Simon, Vernant, Philippe, Lawrence, Shawn, Ergintav, Semih, Cakmak, Rahsan, Ozener, Haluk, Kadirov, Fakhraddin, Guliev, Ibrahim, Stepanyan, Ruben, Nadariya, Merab, Hahubia, Galaktion, Mahmoud, Salah, Sakr, K., ArRajehi, Abdullah, Paradissis, Demitris, Al-Aydrus, A., Prilepin, Mikhail, Guseva, Tamara, Evren, Emre, Dmitrotsa, Andriy, Filikov, S. V., Gomez, Francisco, Al-Ghazzi, Riad, & Karam, Gebran. 2006. GPS constraints on continental deformation in the Africa-Arabia-Eurasia continental collision zone and implications for the dynamics of plate interactions. *Journal of Geophysical Research*, **111**(B5), 1–26.

Reutter, Klaus-J., Giese, Peter, & Closs, Hans. 1980. Lithospheric split in the descending plate: Observations from the Northern Apennines. *Tectonophysics*, **64**, T1 – T9.

Ridente, Domenico, & Trincardi, Fabio. 2006. Active foreland deformation evidenced by shallow folds and faults affecting late Quaternary shelf-slope deposits (Adriatic Sea, Italy). *Basin Res.*, **18**, 171–188.

Ridente, Domenico, Fracassi, Umberto, Di Bucci, Daniela, Trincardi, Fabio, & Valensise, Gianluca. 2008. Middle Pleistocene to Holocene activity of the Gondola Fault Zone (Southern Adriatic Foreland): Deformation of a regional shear zone and seismotectonic implications. *Tectonophysics*, **453**(1-4), 110–121.

Rigo, A., Lyon-Caen, H., Armijo, R., Deschamps, A., Hatzfeld, D., Makropoulos, K., Papadimitriou, P., & Kassaras, I. 1996. A microseismic study in the western part of the Gulf of Corinth (Greece): implications for large-scale normal faulting mechanisms. *Geophysical Journal International*, **126**(3), 663–688.

Rolandone, F, Burgmann, R, Agnew, D C, Johanson, I A, & Templeton, D C. 2008. Aseismic slip and fault-normal strain along the central creeping section of the San Andreas fault. *Geophysical Research Letters*, **35**, 1–5.

Rosen, Paul A, Hensley, Scott, Joughin, Ian R, Li, Fuk K, Madsen, Søren N, Rodríguez, Ernesto, & Goldstein, Richard M. 2000. Synthetic Aperture Radar Interferometry. *PROCEEDINGS OF THE IEEE*, **88**(3), 333–382.

Rovida, A., Camassi, R., Gasperini, P., & Stucchi, M. 2011. *CPTI 11, the 2011 Version of the Parametric Catalogue of Italian Earthquakes.* Available at http://emidius.mi.ingv.it/CPTI, INGV Milano, Bologna.

Rubin, Allan M, Gillard, Dominique, & Got, Jean-luc. 1999. Streaks of microearthquakes along creeping faults. *Nature*, **400**(AUGUST), 635–641.

Ryder, Isabelle, Parsons, Barry, Wright, Tim J., & Funning, Gareth J. 2007. Postseismic motion following the 1997 Manyi (Tibet) earthquake: InSAR observations and modelling. *Geophysical Journal International*, **169**(3), 1009–1027.

Salvini, Francesco, Billi, Andrea, & Wise, Donald U. 1999. Strike-slip fault-propagation cleavage in carbonate rocks: the Mattinata Fault Zone, Southern Apennines, Italy. *Journal of Structural Geology*, **21**(12), 1731–1749.

Sandwell, David T, & Price, Evelyn J. 1998. Phase gradient approach to stacking interferograms. *Journal of Geophysical Research: Solid Earth*, **103**(B12), 30183–30204.

Savage, J C. 1983. A Dislocation Model of Strain Accumulation and Release at a Subduction Zone. *Journal of geophysical research*, **88**(3), 4984–4996.

Savage, J. C. 1990. Equivalent strike-slip earthquake cycles in half-space and lithosphere-asthenosphere Earth models. *Journal of Geophysical Research*, **95**, 4873–4879.

Savage, J. C. 1995. Interseismic uplift at the Nankai subduction zone, southwest Japan. *Journal of Geophysical Research*, **100**, 6339–6350.

Savage, J. C. 1998. Displacement field for an edge dislocation in a layered half-space. *Journal of Geophysical Research*, **103**(B2), 2439–2446.

Savage, J C, & Burford, R O. 1970. Accumulation of tectonic strain in california. *Bullettin of Seismological Society of America*, **60**(6), 1877–1896.

Savage, J. C., & Burford, R O. 1973. Geodetic Determination of Relative Plate Motion in Central California. *Journal of geophysical research*, **78**(5), 832–845.

Savage, J C, & Prescott, W H. 1978. Asthenosphere Readjustment and the Earthquake Cycle. *Journal of Geophysical Research*, **83**(8), 3369–3376.

Scholz, Christopher H. 1998. Earthquakes and friction laws. *Nature*, **391**, 37–42.

Segall, Paul. 2010. *Earthquake and Volcano Deformation*. Princeton, New Jersey: Princeton University Press. Page 432pp.

Segall, Paul, & Davis, James L. 1997. Gps Applications for Geodynamics and Earthquake Studies. *Annual Review of Earth and Planetary Sciences*, **25**(1), 301–336.

Serpelloni, E, Anzidei, M, Baldi, P, Casula, G, & Galvani, A. 2005. Crustal velocity and strain-rate fields in Italy and surrounding regions: new results from the analysis of permanent and non-permanent GPS networks. *Geophysical Journal International*, **161**, 861–880.

Serpelloni, E, Bürgmann, R, Anzidei, M, Baldi, P, Ventura, B Mastrolembo, & Boschi, E. 2010. Strain accumulation across the Messina Straits and kinematics of Sicily and Calabria from GPS data and dislocation modeling. *Earth and Planetary Science Letters*, **298**(3-4), 347–360.

Serpelloni, Enrico, Faccenna, Claudio, Spada, Giorgio, Dong, Danan, & Williams, Simon D. P. 2013. Vertical GPS ground motion rates in the Euro-Mediterranean region: New evidence of velocity gradients at different spatial scales along the Nubia-Eurasia plate boundary. *Journal of Geophysical Research: Solid Earth*, **118**(11), 6003–6024.

Sibson, Richard H. 1985. A note on fault reactivation. *Journal of Structural Geology*, **7**(6), 751 – 754.

Smith, Bridget R, & Sandwell, David T. 2006. A model of the earthquake cycle along the San Andreas Fault System for the past 1000 years. *Journal of geophysical research*, **111**, 1–20.

Socquet, Anne, Simons, Wim, Vigny, Christophe, McCaffrey, Robert, Subarya, Cecep, Sarsito, Dina, Ambrosius, Boudewijn, & Spakman, Wim. 2006. Microblock rotations and fault coupling in SE Asia triple junction (Sulawesi, Indonesia) from GPS and earthquake slip vector data. *Journal of geophysical research*, **111**, 1–15.

Sorel, D. 2000. A Pleistocene and still-active detachment fault and the origin of the Corinth-Patras rift, Greece. *Geology*, **28**(1), 83–86.

Souter, B. J. 1998. *Comparisons of geologic models to GPS observations in southern California*. Ph.D. thesis, Massachusetts Institute of Technology.

Spalluto, M, & Pieri, P. 2008. Carta geologica delle unità carbonatiche mesozoiche e cenozoiche del Gargano sud-occidentale: nuovi vincoli stratigrafici per l'evoluzione tettonica dell'area. *Mem. Descr. Carta Geol. d'It.*, **LXXVII**, 147–176.

Stein, Seth, & Gordon, Richard G. 1984. Statistical tests of additional plate boundaries from plate motion inversions. *Earth and Planetary Science Letters*, **69**, 401–412.

Suhadolc, P., Panza, G. F., & Mueller, S. 1990. Physical properties of the lithosphere—asthenosphere system in Europe. *Tectonophysics*, **176**(1), 123–135.

Thatcher, Wayne. 2009. How the Continents Deform: The Evidence From Tectonic Geodesy. *Annual Review of Earth and Planetary Sciences*, **37**, 237–264.

Tondi, E., Piccardi, L., Cacon, S., Kontny, B., & Cello, G. 2005. Structural and time constraints for dextral shear along the seismogenic Mattinata Fault (Gargano, southern Italy). *Journal of Geodynamics*, **40**(2-3), 134–152.

Tondi, Emanuele. 2000. Geological analysis and seismic hazard in the Central Apennines (Italy). *Journal of Geodynamics*, **29**(3-5), 517–533.

Vaghri, Ali, & Hearn, Elizabeth. H. 2012. Can Lateral Viscosity Contrasts Explain Asymmetric Interseismic Deformation around Strike-Slip Faults? *Bulletin of the Seismological Society of America*, **102**(2), 490–503.

Valensise, G., Pantosti, D., & Basili, R. 2004. Seismology and tectonic setting of the 2002 Molise, Italy, earthquake. *Earthquake Spectra*, **20**, S23–S37.

Vannucci, G., & Gasperini, P. 2004. The new release of the database of Earthquake Mechanisms of the Mediterranean Area (EMMA version 2). *Annales Geophysicae*, **47**(1).

Vergne, J, Cattin, R, & Avouac, J P. 2001. On the use of dislocations to model interseismic strain and stress build-up at intracontinental thrust faults. *Geophysical Journal International*, **147**, 155–162.

Wallace, Laura M, Beavan, John, McCaffrey, Robert, & Darby, Desmond. 2004. Subduction zone coupling and tectonic block rotations in the North Island, New Zealand. *Journal of geophysical research*, **109**, 1–21.

Ward, Steven N. 1994. Constraints on the seismotectonics of the central Mediterranean from Very Long Baseline Interferometry. *Geophysical Journal International*, **117**, 441–452.

Wesson, Robert L. 1988. Dynamics of Fault Creep. *Journal of geophysical research*, **93**, 8929–8951.

Williams, Simon D. P., Bock, Yehuda, Fang, P., Jamason, P., Nikolaidis, R., Prawirodirdjo, Linette, Miller, M., & Johnson, D. 2004. Error analysis of continuous GPS position time series. *Journal of Geophysical Research*, **109**, B03412.

Zebker, H. A., & Villasenor, J. 1992. Decorrelation in interferometric radar echoes. *IEEE Transactions on Geoscience and Remote Sensing*, **30**(5), 950–959.